CARRASCO, MARIA C., MS. Protonation State of the Bridging Ligand in the Resting State of Cytochrome *c* Oxidase: Investigations of Synthetic Heme/Copper Models. (2021)
Directed by Dr. Shabnam Hematian. 114 pp.

Inspiration for our research stems from biological redox processes performed by metalloenzymes. Heme-containing enzymes are able to perform oxidation and reduction reactions, such as in cytochrome P450 and cytochrome c oxidase (CcO). The focus of the work presented in this thesis is on the resting state of the active site of CcO. The active site of CcO consists of an iron porphyrin (heme a3) and copper site (CuB) which perform the four electron, four proton reduction of dioxygen to generate two water molecules. The resting state at this active site contains a bridging oxygen-based ligand and is an intriguing example of a heme-containing oxygen-bridged assembly. We begin with a holistic review of the literature available on these complexes and provide a classification of all μ–(hydr)oxo heme complexes (Chapter I). The exact nature and protonation state of the oxygen-based bridging ligand of the resting state of CcO is not yet known and can have significant implications for its catalytic performance. Therefore, here, we utilize synthetic models to elucidate fundamental aspects of the acid-base chemistry, formation, correlation to structure, electronic-structure, and reactivity. For pK_a measurements of our heme/copper μ–hydroxo complexes, we first prepare a series of weak acids, in the form of protonated nitrogen bases (Chapter II), to then use in titration experiments with our heme/copper μ–oxo complexes (Chapter III).

Chapter I contains an overview of all published oxo- or hydroxo-bridged heme complexes. They are divided into three categories which are those with two identical metal sites and porphyrin ligands (homobinuclear homoleptic complexes), those with two identical metal centers and varying ligand environments (homobinuclear heteroleptic complexes) and those with two different metal centers and ligands (heterobinuclear heteroleptic complexes). A range of investigations have been performed on these (hydr)oxo-bridged heme constructs for the important roles that they play in many life processes or their different applications in catalysis and preparation of new functional materials. We

compiled structural features from crystal structures to gain a better understanding of how modifications in the metal site or ligand environment result in remarkable changes in the reactivity of synthetic μ–(hydr)oxo complexes. Their use in other applications such as materials science and environmental sciences are also discussed.

Chapter II describes the preparation and characterization of the protonated nitrogen bases, or weak acids, later used for titration experiments; these can be classified as alkyl ammoniums, pyridiniums, or anilinium. The anion used with the protonated nitrogen bases is the tetrakis(pentafluorophenyl)borate complex as it increases the solubility of complexes in non-aqueous solvents such as dichloromethane, tetrahydrofuran and toluene. Strikingly, the ^{1}H-NMR spectra of all of these weak acids highlight a distinguished triplet splitting pattern for the coupling of the acidic proton to the quadrupolar ^{14}N nuclei (I = 1). The results point to the relatively slow spin-lattice relaxation of the ^{14}N nucleus in these systems which permits the observation of spin-spin coupling between the ^{14}N and bound ^{1}H nuclei. The proton chemical shifts and ^{14}N-^{1}H coupling constants ($^{1}J_{NH}$) of the acidic protons also correlate well with the known pK_a values and hybridization of the nitrogen site in the respective protonated species.

Chapter III details the pK_a measurements for two heme/copper μ–hydroxo complexes as well as UV-vis and NMR studies of three heme/copper μ–hydroxo complexes. These were obtained through titration experiments with the protonated nitrogen bases described in Chapter II. While previous reports on the pK_a of heme/copper μ–hydroxo complexes provided a range of values for each complex, we are able to provide a pK_a value in a non-aqueous solvent for our heme/copper complexes that can be converted to an aqueous pK_a value. This will be useful for future comparisons of the structural features of the enzyme and synthetic complexes, and how those correlate to a change in basicity of the bridging oxo moiety.

PROTONATION STATE OF THE BRIDGING LIGAND IN THE RESTING STATE OF CYTOCHROME C OXIDASE: INVESTIGATIONS OF SYNTHETIC HEME/COPPER MODELS

by

Maria C. Carrasco

A THESIS

Submitted to
the Faculty of The Graduate School at
The University of North Carolina at Greensboro
in Partial Fulfillment
of the Requirements for the Degree
Master of Science

Greensboro

2021

Approved by

Dr. Shabnam Hematian
Committee Chair

DEDICATION

I dedicate this thesis to my mother, Maria Antonia Cera Ordoñez, my grandmother, Marcelina Ordoñez, my uncle, José Luis Cera, and Mary Elizabeth "Betsy" Huneycutt.

APPROVAL PAGE

This thesis written by Maria C. Carrasco has been approved by the following committee of the Faculty of The Graduate School at The University of North Carolina at Greensboro.

Committee Chair	Dr. Shabnam Hematian
Committee Members	Dr. Mitchell Croatt
	Dr. Jerry Walsh

4/29/2021
Date of Acceptance by Committee

4/7/2021
Date of Final Oral Examination

ACKNOWLEDGEMENTS

The journey to the completion of my master's thesis has been one full of excitement, learning, patience, losses, and many gains. I would not have been able to get through without the encouragement, support, and laughs shared with those in my life. I am ever thankful to them. It has been a great few years with the Department of Chemistry and Biochemistry at the University of North Carolina at Greensboro.

Always there with helpful advice was my thesis advisor, Dr. Shabnam Hematian. Thank you for giving me a chance and for seeing my potential. You have opened more doors than I knew existed and introduced me to my lab mates with whom I had the pleasure of sharing unforgettable memories with; thank you Amy Waldbusser, Katie Dezarn, Dr. Firoz S. T. Khan, and Hadi Pourhadi. I am fortunate to have you as dear friends, evening companions, fellow tea lovers, and bioinorganic chemists.

I thank the faculty and staff in the department, specifically Dr. Jason Reddick who guided me through my transition into chemistry and his delightful course, Dr. Mitchell Croatt who introduced me to a new language, chemistry, Dr. Jerry Walsh who provides watermelons and inorganic knowledge, and Dr. Franklin Moy for his NMR expertise.

Jarrod L. Stanley, whom I have known for as long as I have attended UNC-Greensboro, was a source of great joy and happiness, a constant in a sea of change. You chose the right lab partner Batman.

Most importantly, my journey was possible because of the enduring support, encouragement and motivation from my family. I thank my parents, Maria Antonia Cera *Ordoñez*. and Jesus Octavio Pacheco Gonzalez, and my brother, Jesus Alberto Pacheco Cera. You inspire me to be better, become more, and to never lose sight of my goals. Everything I am is because of you. I am beyond grateful for the love you have given me. Lo logramos!

TABLE OF CONTENTS

LIST OF TABLES

LIST OF FIGURES

LIST OF CHARTS

LIST OF SCHEMES

CHAPTER I: (HYDR)OXO-BRIDGED HEME COMPLEXES: FROM STRUCTURE TO REACTIVITY

This work was co-authored with the following authors and is published under the following citation:
Maria C. Carrasco and Shabnam Hematian
J. Porphyrins Phthalocyanines **2019**, *23*: 1287-1307

Abstract

Iron–porphyrins (i.e., hemes) are present throughout the biosphere and perform a wide range of functions, particularly those that involve complex multiple-electron redox processes. Some common heme enzymes involved in these processes include cytochrome P450, heme/copper oxidase or heme/non-hem diiron nitric oxide reductase. Consequently, the (hydr)oxo-bridged heme species have been studied for the important roles that they play in many life processes or their application for catalysis and preparation of new functional materials. This review encompasses important synthetic, structural and reactivity aspects of the (hydr)oxo-bridged heme constructs that govern their function and application. The properties and reactivity of the bridging (hydr)oxo moieties are directly dictated by the coordination environment of the heme core, the nature and ligation of the second metal center attached to the (hydr)oxo group, the presence or absence of a linker, and degree of flexibility around that linker within the scaffold. Here, we summarize the structural features of all known (hydr)oxo-bridged heme constructs and use those to categorize and thus, provide a more comprehensive picture of structure–function relationships.

Introduction

The characterization of a large class of oxo- and hydroxo-bridged (i.e., *μ*-oxo and *μ*-hydroxo) iron porphyrin complexes has generated considerable interest in their application for catalysis and preparation of new functional materials. Additionally, iron–porphyrins (i.e., hemes) are present throughout the biosphere and perform a wide range of functions involving dioxygen (O_2) chemistry, such as O_2 transport or storage, O_2-mediated catalysis (e.g., peroxidase, catalase, cytochromes P450 (CYPs)), and reduction of O_2 to water (i.e., cytochrome c oxidase (CcO)). Consequently, the (hydr)oxo-bridged iron porphyrin species have been studied for the important roles that they play in many life processes [1,2]. The current examples of these synthetic and biological *μ*-(hydr)oxo iron porphyrin constructs that are crystallographically characterized can be classified into three categories based on the nature of the second metal center attached to *μ*-(hydr)oxo moiety (i.e., in homo- or heterobinuclear arrangements) and its surrounding ligand environment (i.e., homo- or heteroleptic frameworks), see Fig. 1.1.

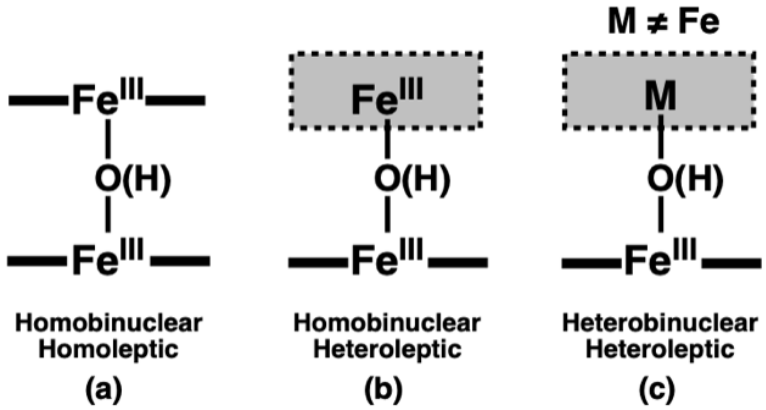

Figure 1.1. Schematic bridging structures of μ-(hydr)oxo iron porphyrin constructs with homo- or heterobinuclear centers in homo- or heteroleptic frameworks

The most common structures of *μ*-(hydr)oxo iron porphyrin are the *μ*-(hydr)oxo heme dimers in which the homobinuclear ferric sites are found in homoleptic ligand environments (Fig. 1.1a). The *μ*-oxo heme dimers, [(P)Fe^{III}–O–Fe^{III}(P)], can form from ferrous heme dioxygen-chemistry [3] or by hydrolysis of ferric hemes in the presence of a base. No specific preference for one method over the other has been established over

the years, and these methods will not be recounted here. These oxo-bridged species are known for their substantial thermodynamic stability. While in the past they were viewed as catalytically inactive species, recent reports have described them as promising oxidative catalysts capable of mimicking cytochrome P450 mono-oxygenase activity despite the lack of selectivity for a wide range of substrates including hydroxylation of C−H bonds, epoxidations, and sulfoxidation of thioether substrates. These reports are discussed in detail under the *Catalysis* and *Other Reactions* sections. Additionally, there is a growing intertest in application of *μ*-oxo heme dimer complexes for development of functional molecular materials such as non-linear optics (NLO), dynamic macrocyclic polymers and hydrogels, molecular cages and sensors. Many studies have also proven that the *μ*-oxo heme dimer complexes of ferriprotoporphyrin IX (i.e., the heme cofactor of hemoglobin) contribute to important biological functions associated with some infectious diseases such as periodontitis (i.e., gum disease) and malaria, *vide infra*.

The second group of *μ*-(hydr)oxo iron porphyrin complexes comprises those with two ferric centers, one bearing a porphyrin ring and the other with a different ligand scaffold (i.e., homobinuclear complexes in heteroleptic ligand environments, Fig. 1.1b). There are only three examples of $[(P)Fe^{III}–O–Fe^{III}(L)]^{n+}$ constructs that are crystallographically characterized. These complexes are among synthetic models for the active site of nitric oxide reductase (NOR) which contains a *μ*-oxo-bridged heme/non-heme moiety in the oxidized active site. These constructs were also studied for photooxidation of various substrates.

Other examples of *μ*-(hydr)oxo iron porphyrin complexes encompass all the heterobinuclear complexes in which the *μ*-(hydr)oxo moiety bridges between a ferric heme and a non-iron metal center (e.g., copper, cobalt, and chromium; see Fig. 1.1c). In particular, *μ*-(hydr)oxo heme-copper complexes have drawn more attention as biomimetic models of heme-copper oxidases such as C*c*O. Despite the significant thermodynamic stability of *μ*-oxo heme dimers $[(P)Fe^{III}–O–Fe^{III}(P)]$, the kinetically stable heterobinuclear $[(P)Fe^{III}–O–Cu^{II}(L)]^{n+}$ constructs can be generated through the reaction of O_2 with equimolar amounts of the corresponding reduced heme and copper complexes. They can

also be synthesized by the acid−base reaction of ferric heme hydroxide compound, [(P)Fe^{III}–OH], and cupric complex, [(L)Cu^{II}] in the presence of a base.

The *μ*-oxo heme-copper complexes are able to readily oxidize nitric oxide ($NO_{(g)}$) to nitrite which occurs through an electrophilic attack of $NO_{(g)}$ on the bridging oxo group accompanied by electron transfer (formally from $NO_{(g)}$ to the ferric heme). Detailed spectroscopic, kinetic-thermodynamic, and density functional theory (DFT) studies of this $NO_{(g)}$ oxidase activity revealed intimated details of the reaction pathway at the molecular level which will be briefly discussed, *vide infra*.

Oxo-Bridged Homobinuclear Homoleptic Systems: [(P)Fe^{III}–O–Fe^{III}(P)]

The *μ*-oxo heme dimers have been extensively studied over the past several decades. In 1969, Fleischer and coworkers [4], and shortly after Hoard and coworkers [5]–with higher resolution data–reported the first X-ray crystal structure for such oxo-bridged complexes (i.e., [(TPP)Fe^{III}–O–Fe^{III}(TPP)]) [6-8]. Since then, over 50 additional structural datasets of various *μ*-(hydr)oxo heme dimers have been deposited in the Cambridge Structural Database (CSD). Table 1.1 summarizes some of the relevant structural parameters for these complexes that are obtained exclusively by X-ray crystallography.

In all known *μ*-(hydr)oxo heme dimers, each ferric center is pentacoordinated bearing a porphyrin ring and a single bridging (hydr)oxo ligand that connects the two ferric centers. The Fe^{III}–O–Fe^{III} core in these compounds is generally near-linear due to the steric requirements for two heme groups coming into close proximity [9,10]. Notably, significant *π*-bonding interactions are present between the bridging oxo and the *d* orbitals of the attached ferric sites, thus their hybridization considerably deviates from sp^3 [11]. Both crystallographic and Extended X-ray Absorption Fine Structure (EXAFS) spectroscopic studies have confirmed that the Fe⋯Fe distances in *μ*-oxo heme dimers are around 3.5 Å and the ferric sites are displaced toward the oxo-bridge by about 0.5 Å from the plane defined by the four porphyrin nitrogen atoms. For example, the ferric centers in [(TPP)Fe^{III}–O–Fe^{III}(TPP)] show larger out-of-plane displacement (i.e., 0.50 Å) from the

plane of four coordinating nitrogen atoms compared to the corresponding five coordinate monomer $[(TPP)Fe^{III}(H_2O)]^+$ (i.e., 0.19 Å) [12].

Due to strong interactions of ferric sites with the bridging oxo moiety, the Fe–O bond lengths are also generally shorter in *μ*-oxo heme dimers compared with ferric–axial ligand distances in corresponding monomer complexes. The *μ*-oxo heme dimers are also electron paramagnetic resonance (EPR)-silent because of strong antiferromagnetic coupling between the two high-spin ($S = {}^5/_2$) ferric sites [13]. The ^{57}Fe Mössbauer spectroscopy, Evans nuclear magnetic resonance (NMR) method, and superconducting quantum interference device (SQUID) magnetometry measurements have confirmed the large antiferromagnetic coupling constants ($J = -120$ to -140 cm^{-1}) for these bridging complexes that is directly correlated with their nearly linear Fe–O–Fe cores and relatively short Fe–O distances (~ 1.75 Å) [14,15].

The bridging oxo moieties in *μ*-oxo heme dimers are commonly basic and upon protonation, which is generally accompanied by varying degrees of re-hybridization, form the corresponding bent *μ*-hydroxo heme dimers [16]. For comparison, the Fe–O–Fe angle of 172° in $[(OEP)Fe^{III}–O–Fe^{III}(OEP)]$ is significantly decreased upon protonation (i.e., Fe–(OH)–Fe angle of the corresponding *μ*-hydroxo heme dimer is 146°) [16], while in some cases such as $[(TPP)Fe^{III}–O–Fe^{III}(TPP)]$ protonation of the bridging oxo only slightly changes the Fe–O(H)–Fe core angle (i.e., < 5°; see Fig. 2.2 and Table 1.1) [17].

Table 1.1. Selected structural features and spectral data for oxo- and hydroxo-bridged heme complexes

Complex	∠(P)Fe–O–M (°)[ε]	∠Twist (°)[δ]	(P)Fe–O (Å)[ϡ]	(P)Fe··M (Å)[ɔ]	Fe-N_p (Å)[α,γ]	ΔN_4··Fe (Å)[ʌ]	Abs. (nm)[β]	Refs.
[(TPP)Fe–O–Fe(TPP)]	174.6	35.4	1.763	3.52	2.087	0.496	408[a]	[4,5]
[(TPP)Fe–(OH)–Fe(TPP)]($B(C_6F_5)_4$)	169.2	29.2	1.821	3.63	2.045	0.411	——	[17]
[($TPPBr_4$)Fe–O–Fe($TPPBr_4$)]	178.7	34.3	1.758	3.52	2.070	0.502	419[i]	[18,19]
[(TTP)Fe–O–Fe(TTP)]	178.3	30.5	1.740/ 1.741	3.48	2.068/ 2.102	0.490/ 0.564	——	[20]
[(TMPyP)Fe–O–Fe(TMPyP)](ClO_4)$_8$	175.2	32.5	1.750	3.50	2.081	0.465	——	[21]
[(*p*-CTPP)Fe–O–Fe(*p*-CTPP)]	180.0	29.2	1.744	3.49	2.081	0.490	——	[22]
[(TBPP)Fe–O–Fe(TBPP)]	174.5	31.0	1.761	3.52	2.080	0.494	408[b]	[23]
[(FF)Fe–O–Fe]	161.1	24.3	1.787	3.53	2.081	0.537	409[c]	[24]

[($TPPF_5$)Fe–O–Fe($TPPF_5$)]	178.5	36.2	1.777	3.55	2.088	0.542	404[j]	[25,26]
[(F_8TPP)Fe–O–Fe(F_8TPP)]	178.3	14.4	1.759	3.52	2.085	0.514	400[d]	[27]
[(Porphen)Fe–O–Fe(Porphen)]	156.8	22.7	1.782	3.49	2.090	0.518	——	[28]
[(OC_2OPor)Fe–O–Fe(OC_2OPor)]	180.0	28.6	1.764	3.53	2.068	0.461	410[b]	[29]
[Ru(OEP)(CO)]$_4$[Fe(*trans*-4-Py_2T_2P)]$_2$O	177.3	29.8	1.762	3.52	2.083	0.469	394[d]	[30]
[Ru(OEP)(CO)]$_4$[Fe(*cis*-4-Py_2T_2P)]$_2$O	171.4	25.8	1.747	3.48	2.057	0.483	394[d]	[30]
[(DEsP)Fe–O–Fe(DEsP)]	166.7	29.5	1.760	3.50	2.072	0.442	——	[31]
[(OEP)Fe–O–Fe(OEP)]	172.2	17.3	1.756	3.50	2.076	0.482	385[d]	[16,32]
[(OEP)Fe–O–Fe(OEP)]	176.2	16.8	1.755	3.51	2.083	0.500	——	[16]
[(OEP)Fe–(OH)–Fe(OEP)](ClO_4)	146.2	8.4	1.938	3.71	2.039	0.381	362[d]	[16]
[(ODM)Fe–O–Fe(ODM)]	178.6	2.4	1.752	3.50	2.065	0.511	414[d]	[9]
[(din-OEP)Fe–O–Fe(din-OEP)]	172.6	18.9	1.756	3.50	2.087	0.482	378[b]	[33]
[(din-OEP)Fe–O–Fe(din-OEP)]	167.8	1.7	1.757	3.49	2.089	0.469	——	[34]
[(trn-OEP)Fe–O–Fe(trn-OEP)]	180.0	0.2	1.758	3.52	2.085	0.456	361[b]	[33]
[(tn-OEP)Fe–O–Fe(tn-OEP)]	175.1	24.2	1.772	3.54	2.095	0.545	369 [b]	[33]
[(tn-OEP)Fe–O–Fe(tn-OEP)]	176.9	21	1.772	3.54	2.088	0.528	369 [b]	[33]
[(TCPP)Fe–O–Fe(TCPP)]	179.8	33.6	1.760	3.52	2.083	0.462	361[h]	[35]
[(PPIXDME)Fe–O–Fe(PPIXDME)]	170.4	27.2	1.748	3.48	2.078	0.416	——	[10]
[(DEP)Fe–O–Fe]	152.0	1.0	1.780	3.45	2.083	0.522	344[d]	[36]
[(ETA)Fe–O–Fe]·CH_3CN	147.9	16.1	1.774	3.41	2.068	0.519	——	[37]
[(ETA)Fe–O–Fe]·C_7H_8	151.2	16.3	1.768	3.42	2.077	0.500	——	[37]
[(ETA)Fe–(OH)–Fe](SbF_6)	152.1	16.4	1.937	3.76	1.976	0.292	376[d]	[38]
[(ETA)Fe–(OH)–Fe](I_3)	142.5	12.9	1.934/ 1.897	3.63	2.007/ 2.051	0.405/ 0.451	380[d]	[39]
[(ETA)Fe–(OH)–Fe](BF_4)	148.6	14.8	1.925/ 1.967	3.75	2.020/ 1.967	0.363/ 0.307	380[d]	[40]
[(ETA)Fe–(OH)–Fe](ClO_4)	141.2	10.8	1.911/ 1.922	3.62	2.063/ 2.054	0.469/ 0.422	372[d]	[40]
[(ETE)Fe–O–Fe]	150.9	0.6	1.783	3.45	2.080	0.532	394[d]	[41]
[(ETE)Fe–(OH)–Fe](ClO_4)	143.8	5.6	1.943	3.69	2.048	0.401	371[d]	[42]
[(ETE)Fe–(OH)–Fe](I_5)	142.4	2.5	1.924/ 1.920	3.64	2.056/ 2.048	0.456/ 0.437	377[d]	[42]
[(ETE)Fe–(OH)–Fe](TNP)	147.3	3.2	1.914	3.67	2.062	0.460	363[d]	[43]
[(DPD)Fe–O–Fe]	158.8	1.5	1.782	3.5	2.105	0.565	395[a]	[44,45]
[(DPXM)Fe–O–Fe]	155.2	3.7	1.789	3.49	2.087	0.566	——	[46]
[(DPA)Fe–O–Fe]	165.7	0.7	1.759	3.49	2.085	0.483	——	*
[(DPX)Fe–O–Fe]	175.8	3.0	1.763	3.52	2.074	0.512/ 0.452	——	*
[(^{6}L)Fe–O–Fe(X)](PF_6)[å]	166.6	——	1.785	3.56	2.074	0.537	416[d]	[47]
[(^{5}L)Fe–O–Fe(Cl)](ClO_4)	157.5	——	1.767	3.48	2.084	0.503	413[d]	[48,49]

[(F_8TPP)Fe–O–Fe(Cl)(TMPA)](ClO_4)	156.6	——	1.777	3.47	2.095	0.464	411[d]	[47,48]
[(NCH_3TPP)Fe-O-Fe(TPP)](ClO_4)	165.3	30.2	1.741/ 1.767	3.48	2.107/ 2.067	0.546/ 0.441	414[l]	[50,51]
[(TMP)Fe–O–Cu(5MeTPA)] ($B(C_6F_5)_4$)	172.8	——	1.760	3.61	2.115	0.601	442[k]	[52]
[(TMPP)Fe–O–Cu(TMPA)]($B(C_6F_5)_4$)	173.5	——	1.720	3.54	2.102	0.548	443[e]	[53]
[(F_8TPP)Fe–O–Cu(TMPA)](ClO_4)	178.2	——	1.740	3.60	2.105	0.554	435[e]	[54,55]
[(F_8TPP)Fe–O–Cu(MePY2)]($B(C_6F_5)_4$)	142.5	——	1.756	3.41	2.094	0.553	438[e]	[55]
[(F_8TPP)Fe–O–Cu(L^{Me_2N})]($B(C_6F_5)_4$)	143.5	——	1.747	3.42	2.096	0.550	449[f]	[56]
[(F_8TPP)Fe–O–Cu(AN)](CF_3O_3S)	149.5	——	1.746	3.44	2.090	0.507	440[g]	[57]
[(^{6}L)Fe–O–Cu]($B(C_6F_5)_4$)	171.1	——	1.749	3.59	2.103	0.579	424[c]	[58]
[(OEP)Fe–O–Cu(Me_6tren)](ClO_4)	176.6	——	1.744	3.57	2.112	0.581	427[d]	[59]
[(OEP)Fe–(OH)–Cu(Me_5dien)($OClO_3$)](ClO_4)	157.1	——	1.928	3.81	2.042	0.414	——	[60]
[(TPP)Fe–O–Cr(Pip)(TPP)]	177.7	29.7	1.751	3.53	2.097	0.533	427[a]	[61]
[(TMPP)Fe–O–Cr(Py)(TPP)]	178.0	32.0	——	3.60	——	——	424[a]	[62]
[(F_8TPP)Fe–O–Co(TMPA)](ClO_4)	171.6	——	1.747	3.58	2.110	0.562	437[d]	[63]
{Au_8(μ-PAnP)$_4$[(TPyP)Fe–O–Fe(TPyP)]}(CF_3O_3S)$_8$	157.8	19.9	1.752	3.44	2.030	0.428	412	[64]
[(TPP)Fe–O–Fe(TPP)]·C_{60}	173.7	30.3	1.758	3.51	2.078	0.467	——	[65]
[(TPP)Fe–O–Fe(TPP)]·C_{70}	180.0	29.0	1.756	3.51	2.083	0.490	——	[66]
[(OEP)Fe–O–Fe(OEP)]·C_{60}	150.2	28.7	1.773	3.43	2.098	0.515	——	[67]

[Λ] Iron displacement from the porphyrin's nitrogen plane (N_4); [α] Nitrogen atoms forming porphyrin core (N_p); [β] UV-visible absorption (Soret band); [γ] Average of eight (or four) Fe-N bond distances; [δ] Degree of torsion (twist) between two porphyrin rings; [ε] Degree of bending in the heme iron–oxo–metal ((P)Fe–O–M) moiety; [ζ] Bond distance between the heme-iron and bridging O-atom; average of two bonds unless two distances are stated; [Ɔ] Heme iron to metal bond distance; * CSD Private Communication; [å] Ligand X^- represents chloride or methoxide; [a] Benzene; [b] Chloroform; [c] Toluene; [d] Dichloromethane; [e] Acetone; [f] 6% Propionitrile : 94% Dichloromethane; [g] Tetrahydrofuran; [h] n-Dimethylformamide; [i] Benzonitrile; [j] Methanol; [k] Acetonitrile; [l] Dichloroethane; [m] 10% Methanol : 90% Chloroform

It is noteworthy that the two porphyrin cores in [(TPP)Fe^{III}–(OH)–Fe^{III}(TPP)]$^+$ adopt ruffled-type conformations in which opposite pyrrole rings are counter-rotated in a way that the *meso* carbons are alternatively displaced upward and downward with respect to the mean of the porphyrin planes (Fig. 1.2).

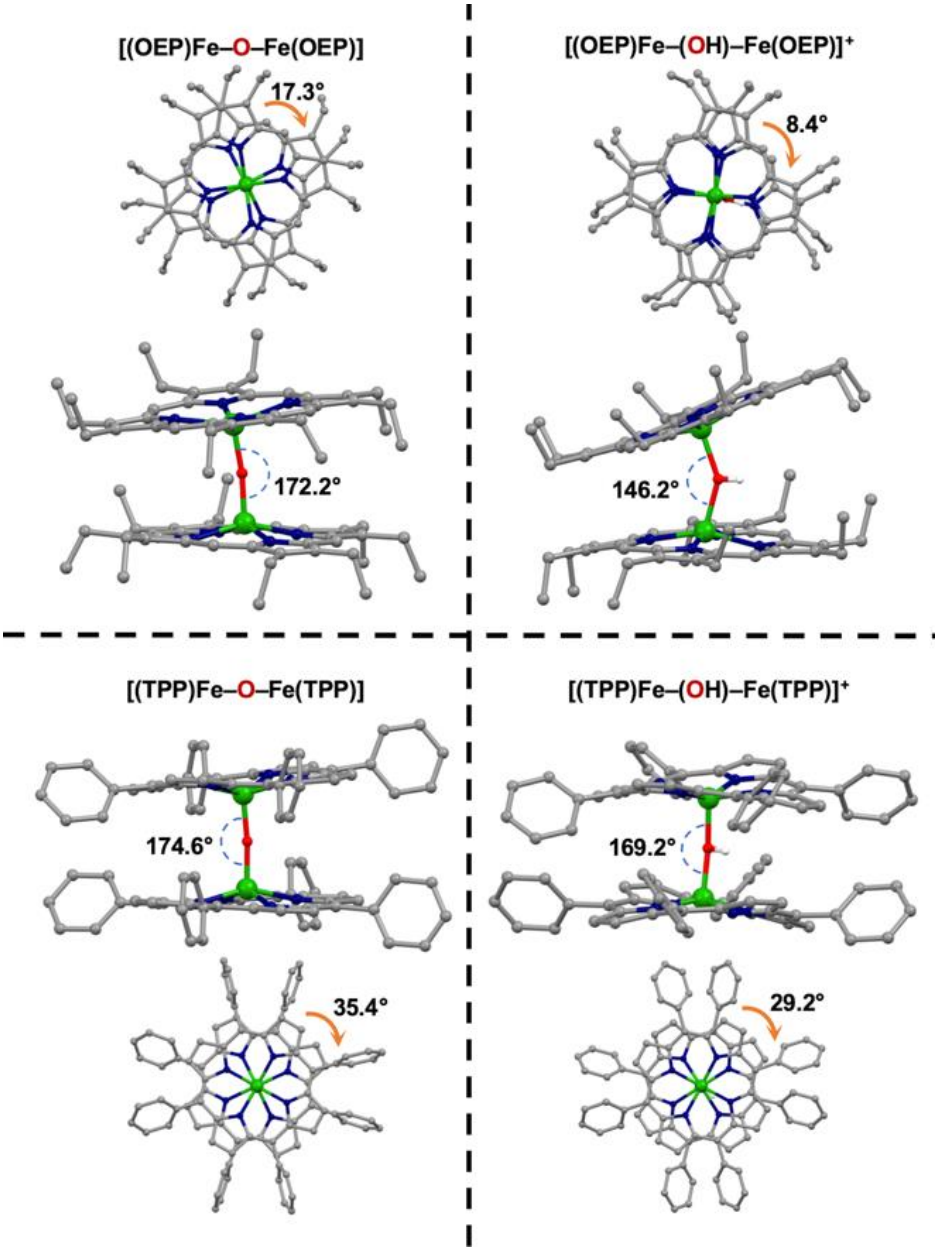

Figure 1.2. Side-by-side views of μ-oxo and μ-hydroxo heme dimers, [(P)FeIII–O(H)–FeIII(P)]n+ (n = 0 or 1), with the OEP or TPP frameworks, displaying their structural differences such as the Fe–O–Fe moiety angles and twist angles.

Another important structural parameter in *μ*-(hydr)oxo heme dimers is the N_p–Fe–Fe'–N'_p dihedral angle (i.e., twist angle). The two possible extreme conformations are eclipsed (i.e., D_{4h} symmetry and twist angle = 0°) and staggered (i.e., D_{4d} symmetry and twist angle = 45°). The smaller average twist angle for [(OEP)Fe^{III}–O–Fe^{III}(OEP)] (~ 17°) compared with that of [(TPP)Fe^{III}–O–Fe^{III}(TPP)] (~ 35°), and other *meso*-substituted

μ-oxo heme dimers can be interpreted in terms of steric hindrance between the bulky peripheral substituents which is absent in the *μ*-oxo heme dimer bearing the OEP frameworks. The facing porphyrin rings in all derivatives of [(TPP)Fe^{III}–O–Fe^{III}(TPP)] are also considerably rotated with respect to each other so that peripheral phenyl rings are almost staggered, see Fig. 1.2. Thus, the twist angle is a sensitive function of the peripheral substituents and interplanar spacing.

In addition to the extensive number of studies on organic-soluble *μ*-oxo heme dimers, many synthetic water-soluble derivatives have also been prepared [21,68]. For these derivatives the bulky peripheral groups can also deter the aggregation process while water solubility can be achieved through charged peripheral substituents such as the negatively charged sulfonates in [(TPPS)Fe^{III}–O–Fe^{III}(TPPS)]$^{8-}$ or the positively charged methylpyridinium groups in [(TMPyP)Fe^{III}–O–Fe^{III}(TMPyP)]$^{8+}$. The structural features of the water-soluble *μ*-oxo heme dimers are mostly comparable with their organic-soluble counterparts, see Table 1.1.

A large variety of additional modifications on the heme cores have led to a number of other novel *μ*-oxo heme dimer structures. For example, efforts for introduction of a potential second metal binding site in a phenanthroline-strapped porphyrin framework or attempts for providing a barrier above the porphyrin ring in “capped” porphyrins resulted in the discovery of the very bent *μ*-oxo moiety in [(Porphen)Fe^{III}–O–Fe^{III}(Porphen)] [28] and perfectly linear arrangement in [(OC_2OPor)Fe^{III}–O–Fe^{III} (OC_2OPor)] [29], see Table 1.1.

The electronic absorption spectra of *μ*-oxo heme dimers are blue-shifted relative to their corresponding ferric heme monomers. For example, in dichloromethane (DCM), the Soret band of dimeric [(OEP)Fe^{III}–O–Fe^{III}(OEP)] is at 385 nm while that of monomeric [(OEP)Fe^{III}(ClO_4)] is at 389 nm. Additionally, the UV-vis spectrum of the protonated dimer, [(OEP)Fe^{III}–(OH)–Fe^{III}(OEP)] shows a strongly blue-shifted Soret band at 362 nm [16], see Table 1.1. These blue shifts of the electronic absorption spectra are ascribed to the excitation coupling between the two heme chromophores which are diagnostic of dimeric constructs with the cofacial orientations.

ELECTROCHEMISTRY

A number of studies have suggested that the stepwise first and second one-electron reduction of the *μ*-oxo diferric heme dimers are metal-centered. The first electrochemical reduction yields a paramagnetic ferric-ferrous *μ*-oxo heme dimer intermediate (g = 1.95) followed by the second reduction step to generate a fully reduced high-spin ferrous-ferrous *μ*-oxo heme dimer intermediate [18,69-72]. These dimer species have been postulated based on a combination of electrochemical analysis and the data obtained from surface-enhanced Raman scattering (SERS), UV-vis absorption and EPR spectroscopies. However, there appear to be some disagreements in the literature over the exact nature of the bridging group (i.e., *μ*-oxo or -hydroxo) in these dimeric intermediates [73].

Furthermore, cyclic voltammetry of *μ*-oxo heme dimers such as [(TPP)Fe^{III}–O–Fe^{III}(TPP)] show two chemically reversible one-electron oxidation processes and in most cases both oxidations appear to take place on porphyrin cores rather than iron centers [15]. The products of these oxidations have not been structurally characterized, but spectroscopic and magnetic measurements strongly support formation of the porphyrin *π*-cation radical with strong antiferromagnetic coupling to the ferric center [74-76].

TETHERED SYSTEMS

Cofacial or “Pacman” type porphyrin systems have a rich history in catalyzing multielectron redox reactions of small molecules (e.g., four electron reduction of O_2 to water) [77,78]. Consequently, the chemistry of tethered *μ*-(hydr)oxo heme dimers where the two porphyrin rings are covalently connected have drawn considerable interest in recent years and have been meticulously reviewed elsewhere [79-82]. Both “rigid” and “flexible” linkers of variable lengths have been used for controlling the Fe⋯Fe distance and degree of opening and closing within the cofacial cleft, see Chart 1.1.

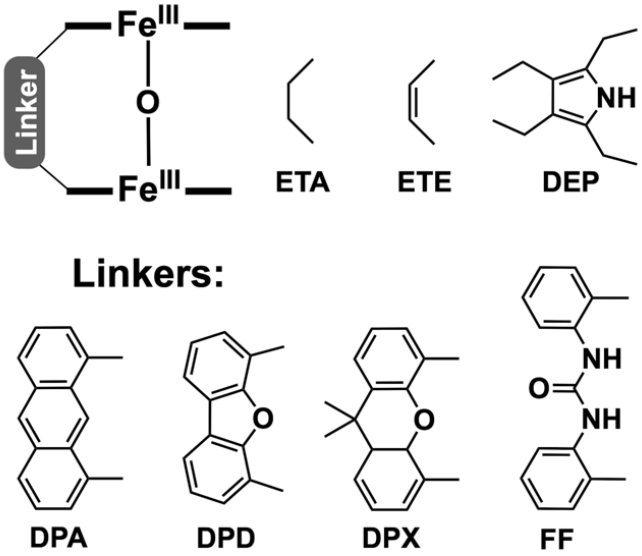

Chart 1.1. Schematic representation of tethered μ oxo heme dimers bearing “rigid” or “flexible” linkers.

Reed and coworkers reported the first example of a *bis*-iron(III)-*μ*-oxo cofacial porphyrin [24]. The urea-linked *bis*-tetraphenyl porphyrin (FF) accommodates a bent Fe–O–Fe angle of 161° possibly due to the hydrogen-bonding network of two water molecules between the bridging oxo moiety and hydrogen atoms of the urea linker, see Chart 1.1. The FF scaffold also allows significant rotational flexibility for the tethered porphyrin rings as evidenced by the twist angle of 24°. Later, Nocera and coworkers prepared a host of *bis*-iron(III)-*μ*-oxo cofacial porphyrins bearing rigid linkers such as dibenzofuran (i.e., DPD, DPDM and DPDF) and xanthene (i.e., DPX and DPXM) [44-46,83,84]. Unlike other *μ*-oxo heme dimers, rotation of the two heme cores with respect to each other is restricted by the rigid dibenzofuran or xanthene linker (Chart 1.1), thereby creating an almost eclipsed conformation with a twist angle of less than 4° (Table 1.1). Interestingly, these tethered platforms with rigid linkers can house a variety of Fe–O–Fe angles; from a near-linear *μ*-oxo structure in DPX (i.e., 176°) to a bent Fe–O–Fe angle of 155° in DPXM.

To bring the two ferric sites in closer contact, Rath and coworkers prepared alternative cofacial constructs bearing linkers with different degrees of flexibility (i.e., ethane-, ethene-, and pyrrole-bridged *μ*-oxo heme dimers, see Chart 1.1) [36,37,41,85]. Perhaps the most striking features of these *bis*-iron(III)-*μ*-oxo constructs are their small cleft size

which directly translates to the very bent Fe–O–Fe angle of about 150° and shorter Fe···Fe distance (i.e., ≤ 3.45 Å) compared to other known *μ*-oxo heme dimers, see Table 1.1. The highly flexible ethane linker in the ETA framework allows for the heme cores to make a 16° twist angle to minimize the steric hindrance of the ethyl groups. In turn, the relatively less flexible pyrrole linker in the DEP framework or the rigid ethene linker in the ETE scaffold restricts the free rotation of the attached heme cores, thus holding them in a fully eclipsed conformation (i.e., twist angle of ≤ 1°). A series of *bis*-iron(III)-*μ*-hydroxo cofacial porphyrins of this group (i.e., ETA, ETE, and DEP) have been generated from protonation of the corresponding *μ*-oxo complexes by addition of strong Brønsted acids with non- or weakly coordinating conjugate bases (e.g., BF_4^-, PF_6^-, SbF_6^-, ClO_4^-, and I^-). In these tethered systems, further bending of the Fe–O(H)–Fe angle upon protonation is also observed; consequently, the two heme cores further approach each other. The extreme closeness of the two heme chromophores leads to even more substantial blue-shifting in the *bis*-iron(III)-*μ*-hydroxo cofacial porphyrins compared to their *μ*-oxo counterparts. Another interesting observation is the lack of equivalency of the spin states in the attached heme cores of these tethered *μ*-hydroxo systems. The computational and spectroscopic studies point to varying degrees of interaction between the linked ferric hemes and different counter anions that may result in subtle environmental perturbations in one of the ferric sites. These asymmetric interactions are generally governed by the size, charge, and nature of the anions, which consequently can lead to increased ring deformation and modulation of the spin state of one of the two ferric heme cores. For instance, the *bis*-iron(III)-*μ*-hydroxo cofacial porphyrins with I_3^- or I_5^- counterions, possess one high-spin ferric site ($S = {}^5/_2$) along with a second ferric site with admixed-intermediate spin state ($S = {}^3/_2$ with a minor contribution from $S = {}^5/_2$).

The stochiometric reaction of a weaker acid such as 2,4,6-trinitrophenol (HTNP) with [(ETE)Fe^{III}–O–Fe^{III}] generates the *μ*-hydroxo adduct, [(ETE)Fe^{III}–(OH)–Fe^{III}]·(TNP) in which the planar structure of the phenoxide group fits within the cofacial cleft cavity, therefore forming a fairly strong hydrogen bond with the bridging hydroxo moiety (i.e. $O_1 \cdots O_8$ distance is 2.58 Å and C–O_8 bond length is 1.24 Å) [86], see Fig. 1.3. Interestingly, the two ferric centers in this adduct are equivalent (high-spin state; $S = {}^5/_2$)

in the solid state and both convert to intermediate spin (S = $^3/_2$) in solution as observed by ^{1}HNMR spectroscopy. The results from several DFT calculations were also in agreement with the experimentally observed ferric spin crossover triggered by hydrogen bonding. Further titration of the [(ETE)Fe^{III}–(OH)–Fe^{III}]·(TNP) with the second equivalent of the phenol results in breakage of the bridging hydroxo moiety and formation of one water molecule. This is accompanied by coordination of one of the resulting phenoxide groups to each ferric site forming [(ETE)Fe^{III}_2(TNP)$_2$] [43]. Hendrickson and Wollmann also reported a similar observation for the reaction of excess organic acids with the untethered *μ*-oxo complex, [(TPP)Fe^{III}–O–Fe^{III}(TPP)] [87,88].

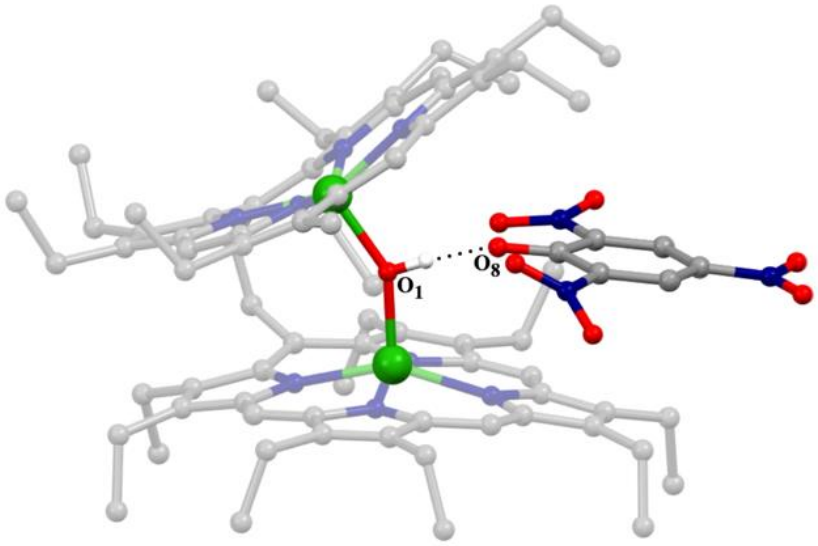

Figure 1.3. X-ray crystal structure of the *bis*-iron(III)-*μ*-hydroxo cofacial porphyrin, [(ETE)Fe^{III}–(OH)–Fe^{III}], and 2,4,6-trinitrophenoxide adduct with a fairly strong hydrogen bond between the phenoxide group and the bridging hydroxo moiety. Recreated with permission from Ref. [43]. Copyright 2016 John Wiley & Sons, Inc.

CATALYSIS

Several tethered and untethered *μ*-oxo heme systems have been studied for both photochemical and thermochemical catalytic oxidations of a variety of substrates under different conditions. In all cases, the ferryl heme species are widely invoked as key oxidizing intermediates that are formed during the catalytic cycles proceeded by

heterolytic cleavage of the Fe–O–Fe moiety [15]. Furthermore, a common unwanted side reaction is self-degradation of the heme sites due to attack of these highly reactive intermediates on the porphyrin ring itself.

The first examples of the photolysis of *μ*-oxo heme dimers were provided by Richman and Peterson in the 1980s. The authors showed that direct excitation of the O → Fe ligand-to-metal charge transfer (LMCT) band (λ_{max} = 320 nm) leads to photochemical disproportionation of [(TPP)Fe^{III}–O–Fe^{III}(TPP)] into the corresponding ferrous and oxo-ferryl monomers (i.e., [(TPP)Fe^{II}] and[(TPP)Fe^{IV}=O]) [89-91]. The resulting ferryl heme monomer represents a strong oxidant that is capable of substrate oxidation through an oxygen atom transfer reaction [92]. Subsequently, the second equivalent of ferrous heme is formed, and the *μ*-oxo heme dimer is regenerated in the presence of O_2, thus the process becomes catalytic. By photolyzing [(TPP)Fe^{III}–O–Fe^{III}(TPP)] in the presence of O_2, catalytic oxidation of a wide range of substrates such as alkyl and aryl phosphines, amines and olefins was accomplished [93,94].

Furthermore, the picosecond absorption studies of the photoexcitation of [(TPP)Fe^{III}–O–Fe^{III}(TPP)] by Rentzepis and coworkers revealed the presence of a very short-lived intermediate with a lifetime of < 100 ps which was described as an excited state localized to a monomer unit. Subsequently, this intermediate converts mainly to the photodissociated pair [(TPP)Fe^{III}]$^+$ plus [(TPP)Fe^{III}–O]$^-$ and, to a lesser extent, forms the photodisproportionation products, [(TPP)Fe^{II}] and [(TPP)Fe^{IV}=O], see Scheme 1.1. In the absence of substrates, the recombination of the photoproducts takes place in less than 5 ns, regenerating the starting *μ*-oxo heme dimers [95]. Later, resonance Raman (RR) studies further confirmed the formation of the five-coordinate low-spin oxo-ferryl (i.e., [(TPP)Fe^{IV}=O]) from the photodisproportionation of [(TPP)Fe^{III}–O–Fe^{III}(TPP)] in a detergent micelle at room temperature (e.g., Fe^{IV}=O vibrational frequency (ν_{FeO}) is at 843 cm^{-1}) [96].

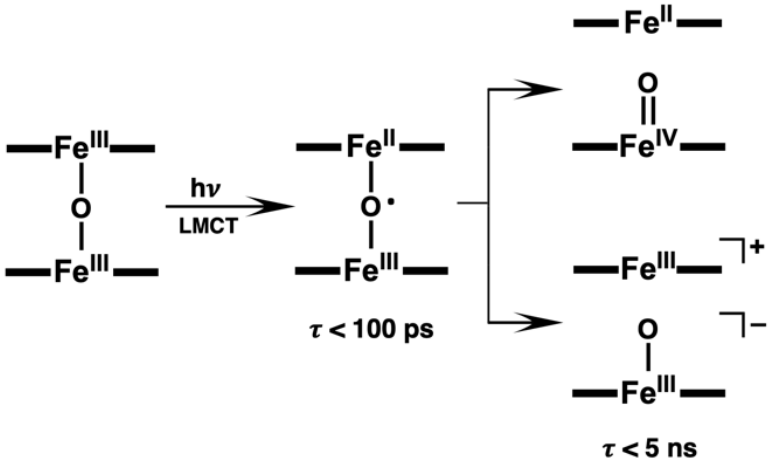

Scheme 1.1. Two chemically feasible photoproducts (i.e., the photodisproportionation products (top) and photodissociated pair (bottom)) resulting from LMCT excitation of *μ*-oxo heme dimers.

Nocera and coworkers have done considerable research on the photophysics of a number *bis*-iron(III)-*μ*-oxo “Pacman” porphyrin systems [78]. In order to understand the effect of a spring-loaded cleft on the photoinduced oxygenation of substrates, a comparative reactivity study of two tethered (i.e., DPD and DPX) and one untethered (i.e., etioporphyrin abbreviated as Etio) *bis*-iron(III)-*μ*-oxo porphyrin systems was performed [83]. The results of the stoichiometric oxygenation reactions of dimethyl sulfide (DMS) revealed that the product quantum yields for formation of both dimethyl sulfoxide (DMSO) and dimethyl sulfone ($DMSO_2$) increase in the order of: [(DPX)Fe^{III}–O–Fe^{III}] < [(Etio)Fe^{III}–O–Fe^{III}(Etio)] < [(DPD)Fe^{III}–O–Fe^{III}]. According to this observation, the authors proposed that the significant vertical flexibility of the DPD platform, triggers the “molecular spring” action of [(DPD)Fe^{III}–O–Fe^{III}], which can hinder recombination and regeneration of the starting *bis*-iron(III)-*μ*-oxo porphyrin system to some extent and/or support a side-on approach of substrate to the oxo-ferryl intermediate. Subsequently, the transient absorption study showed that the cage escape yield is generally low, even for the untethered system [45]. The results suggested that the quantum yields of photocatalytic oxidation of substrates may be significantly increased if the escape yield of photodisproportionation intermediates (i.e., Fe^{II}/Fe^{IV}=O pair) can be improved.

Later, a modified DPD platform bearing three pentafluorophenyl groups in the *meso* positions of the porphyrin rings (DPDF) was investigated [84]. The electron-withdrawing peripheral substituents enhance the oxidizing power of the photogenerated oxo-ferryl species, therefore the corresponding *bis*-iron(III)-*μ*-oxo porphyrin system catalyzes the aerobic photochemical oxidation of phosphines, sulfides, olefins, and hydrocarbons with higher turnover numbers [84,97]. Notably, the presence of the ancillary pentafluorophenyl groups in the [(DPDF)Fe^{III}–O–Fe^{III}] system also lowers the susceptibility of the porphyrin to oxidative decomposition and induces the photoreaction at longer wavelengths in the visible region (λ_{exc} > 425 nm) [84,97]. The photochemical efficiency of substrate oxidation also diminishes with an increase in the steric bulk of the substrates, due to limited access to cleft of the “Pacman” scaffold and active oxidant.

Turning next to the ethane- and ethene-bridged *μ*-oxo heme dimers, Rath and coworkers reported both stoichiometric and catalytic photochemical oxidation of organophosphites (i.e., $P(OR)_3$; R = Me, Et) under anaerobic and aerobic conditions, respectively. The [(ETE)Fe^{III}–O–Fe^{III}] platform with the rigid ethene linker shows higher photochemical catalytic efficiency [37,41,85].

The first reports of related studies on thermochemical catalytic oxidation of hydrocarbons (e.g., hydroxylation of cyclohexane or *2*-methylbutane) using [(TPP)Fe^{III}–O–Fe^{III}(TPP)] with iodosobenzene (PhIO) as a terminal oxidant were published by Guo in 1994. The author also evaluated the effect of peripheral substituents (electron-donating *vs*. electron-withdrawing), reaction temperature, solvent, and exposure to air on the catalytic activity of the *μ*-oxo heme dimers [98-100]. Later, the application of *μ*-oxo heme dimers for direct aerobic oxidation of other hydrocarbons (e.g., cyclopentane, cyclooctane, ethylbenzene or toluene), with the O_2 serving as the terminal oxidant, was investigated [101-103]. Guo and coworkers subsequently examined the influence of dioxygen pressure and flow rate in the homogeneous liquid-phase aerobic oxidation of toluene to benzaldehyde, benzyl alcohol, and benzoic acid under conditions similar to those of commercial operations. Their results from semi-batch and continuous operation mode reveal that at O_2 partial pressure lower than 0.070 MPa at 190 °C, the oxidation of toluene is directly limited by the concentration of dissolved O_2, whereas the oxidation rate of

toluene is zero-order with respect to O_2 at higher partial pressures. Moreover, they showed that the sequential decrease of temperature in a series of three stirred-tank reactors could significantly increase the selectivity and yield of benzaldehyde and benzyl alcohol up to about 17 and 44%, respectively [104,105].

Despite extensive reports on the thermochemical oxidation of substrates using *μ*-oxo heme dimers, the intricate nature and mechanism of formation of the putative ferryl intermediate(s) involved are still unclear. The *μ*-oxo heme dimers are generally regarded as thermally inert species that show little or no tendency toward thermochemical disproportionation. However, a recent study by Meyer and coworkers shows that a non-heme *bis*-iron(III)-*μ*-oxo with macrocyclic tetracarbene (L^{NHC}) ligation, $[(L^{NHC})Fe^{III}–O–Fe^{III}(L^{NHC})]^{4+}$, thermally disproportionates in an acetonitrile solution into the oxo-ferryl and ferrous components. The disproportionation equilibrium for this *μ*-oxo complex in the dark, although very small (i.e., $K_{eq} = 7.5 \times 10^{-8}$ M), is non-zero and translates to Gibbs free energy change (ΔG°) of about 40 kJ.mol^{-1} (i.e., 9.6 kcal.mol^{-1}) at room temperature [106]. A similar disproportionation equilibrium may be responsible for the observed thermochemical reactivity of *μ*-oxo heme dimers toward a wide range of substrates.

OTHER REACTIONS

The *μ*-oxo heme dimers have also been explored for other redox and acid-base reactions. For example, Webster and coworkers reported that *μ*-oxo heme dimers, such as $[(TPP)Fe^{III}–O–Fe^{III}(TPP)]$, can readily catalyze the hydrophosphination of styrene derivatives and effect one or two consecutive activation reactions on the primary phosphines to form secondary or tertiary products in modest to excellent yields [107], see Fig. 1.4. The electron-deficient analogue of the TPP platform with the pentafluorophenyl *meso*-substituents in $[(TPPF_5)Fe^{III}–O–Fe^{III}(TPPF_5)]$ has been utilized for an oxidative desulfurization process of a model oil containing the representative refractory sulfur compounds in petroleum such as dibenzothiophene and its derivatives. The catalytic system operates in a biphasic medium at room temperature and in the presence of H_2O_2 as the terminal oxidant forming the corresponding sulfoxides and sulfones [26].

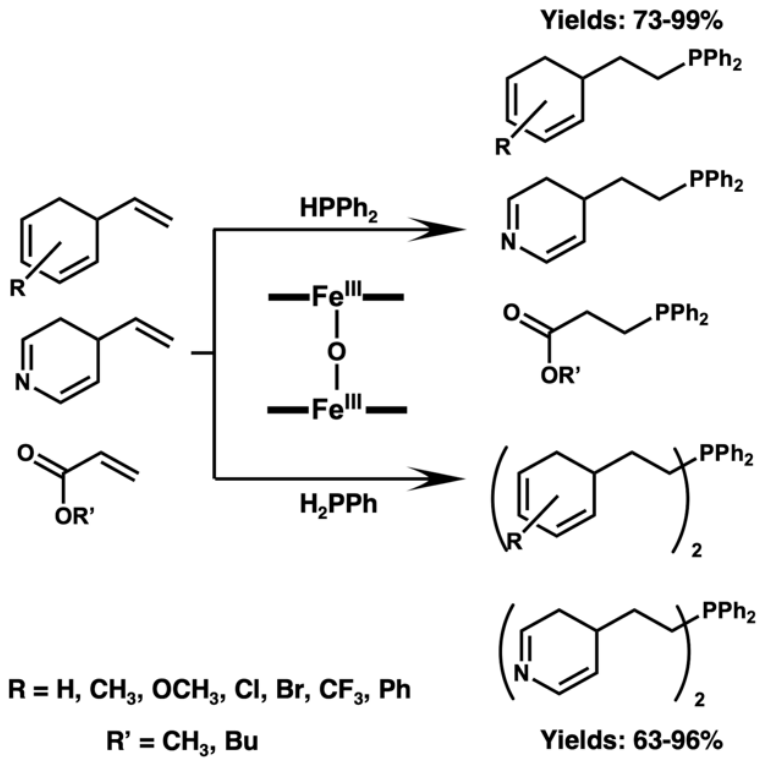

Figure 1.4. Hydrophosphination of some activated alkenes with activated primary (H_2PPh) or secondary ($HPPh_2$) phosphines catalyzed by [(TPP)Fe^{III}–O–Fe^{III}(TPP)] as reported in Ref. [107].

Another example of the *μ*-oxo heme dimers developed for catalyzing redox processes is [(TCPP)Fe^{III}–O–Fe^{III}(TCPP)]. Here, the peripheral carboxylic groups form a network of hydrogen bonds between porphyrin planes of neighboring *μ*-oxo heme dimers creating a two-dimensional (2D) array. Subsequently, the 2D arrays are stacked along the (001) direction supporting the interlayer *π*–*π* interactions (interlayer distance is about 3.7 Å) and ultimately form a continuous three-dimensional (3D) porous network, see Fig. 1.5. The resulting coordination network exhibits moderate heterogeneous catalytic activity for the oxidation of alcohols to aldehydes. Remarkably, the *μ*-oxo heme dimer scaffold plays a dual role as both the catalyst and supramolecular synthon in the catalytic network [35].

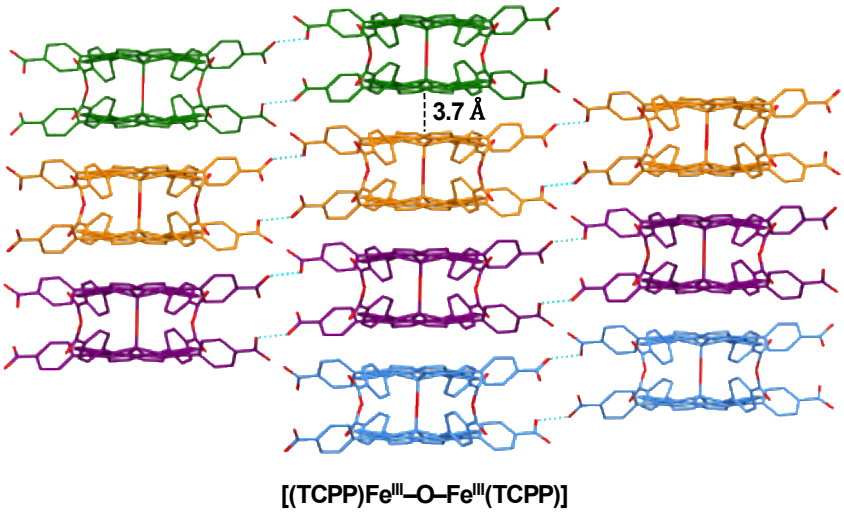

Figure 1.5. Stacking of hydrogen bonded 2D layers of the [(TCPP)Fe^{III}–O–Fe^{III}(TCPP)] units through π-π interactions (about 3.5 to 3.9 Å) among the dimers of each layer. Adapted with permission from Ref. [35]. Copyright 2015 Royal Society of Chemistry.

Reactivity of a series of μ-oxo heme dimers toward various nitrogen oxides (e.g., nitric oxide ($NO_{(g)}$), dinitrogen tetroxide (N_2O_4), and dinitrogen trioxide (N_2O_3)) have also been studied by Fanning, Scheidt and coworkers [108,109]. The reaction of the [(TPP)Fe^{III}–O–Fe^{III}(TPP)] complex with $NO_{(g)}$ in toluene yields the nitro-nitrosyl complex, [(TPP)Fe^{III}(NO_2)(NO)], while its reaction with N_2O_4 or N_2O_3 in toluene produces the corresponding ferric heme nitrate (i.e., [(TPP)Fe^{III}(NO_3)]) [108]. Moreover, the μ-oxo heme dimers can serve as precursors for the preparation of a host of bridged heme dimer species through the acid–base reactions. An example for such species is the first structurally characterized heme hyponitrite adduct, [(OEP)Fe^{III}–($N_2O_2^{2-}$)–Fe^{III}(OEP)], which was generated by the reaction of the corresponding μ-oxo heme dimers (i.e., [(OEP)Fe^{III}–O–Fe^{III}(OEP)]) with hyponitrous acid ($H_2N_2O_2$) accompanied by the release of a water molecule [110].

APPLICATIONS IN FUNCTIONAL MOLECULAR MATERIALS

The μ-oxo heme dimer is a versatile platform for additional substitutions and the construction of preorganized frameworks, therefore there is a growing intertest in the potential application of μ-oxo heme dimer complexes in the field of functional molecular

materials. It has been shown that the nonlinear optical properties of the *μ*-oxo heme dimers are superior in comparison with the corresponding monomers due to their more delocalized *π*-conjugated systems. For example the self-assembled nanostructures of the [(TBPP)Fe^{III}–O–Fe^{III}(TBPP)] complex are endowed with remarkable third-order nonlinear optical (NLO) properties and show almost an order of magnitude larger two-photon absorption (TPA) cross-section value than that of the monomer [23].

Additionally, efforts for development of photoactive materials for photovoltaic and light harvesting applications have led to interesting *μ*-oxo-heme-dimer-fullerene supramolecular architectures. These fullerene-adducts generally exhibit intense charge transfer (CT) bands in the visible range due to effective overlap of their highest occupied molecular orbital (HOMO) and lowest unoccupied molecular orbital (LUMO) between the concave surfaces of the five-coordinate porphyrin moieties and spherical fullerene molecules. Balch and coworkers cocrystallized the [(OEP)Fe^{III}–O–Fe^{III}(OEP)] complex with fullerene in benzene. The Fe–O–Fe angle in [(OEP)Fe^{III}–O–Fe^{III}(OEP)]·C_{60}·C_6H_6 is markedly bent at 150° and a benzene molecule inserted into the space between the two porphyrin rings, see Fig. 1.6. Thus, the significant variation for the Fe–O–Fe angle in the supramolecular assembly and starting *μ*-oxo heme dimer (∠Fe–O–Fe = 172°) reveals that the bridging oxo moiety in these platforms is rather flexible and can be varied by a combination of intermolecular interactions and crystal packing forces [67]. Cocrystallization of [(TPP)Fe^{III}–O–Fe^{III}(TPP)] with the spherical C_{60} fullerene also forms a neutral solid-state supramolecular architecture with significantly modified optical properties. The Fe–O–Fe angle in the [(TPP)Fe^{III}–O–Fe^{III}(TPP)]·C_{60} is similar to that of the parent compound, see Fig. 1.6 and Table 1.1 [65]. Moreover, the complexation of the [(TPP)Fe^{III}–O–Fe^{III}(TPP)] with the ellipsoidal C_{70} fullerene has been studied by Lyubovskaya and coworkers. A close examination of molecular packing of [(TPP)Fe^{III}–O–Fe^{III}(TPP)]·C_{70} reveals that at room temperature, freely rotating C70 molecules occupy the large cavities formed by the *μ*-oxo heme dimers, whereas at lower temperature (T ≤ 100 K) the appearance of additional Van der Waals forces significantly reduces the size of those vacancies, thus hindering the rotation of C_{70} molecules [66].

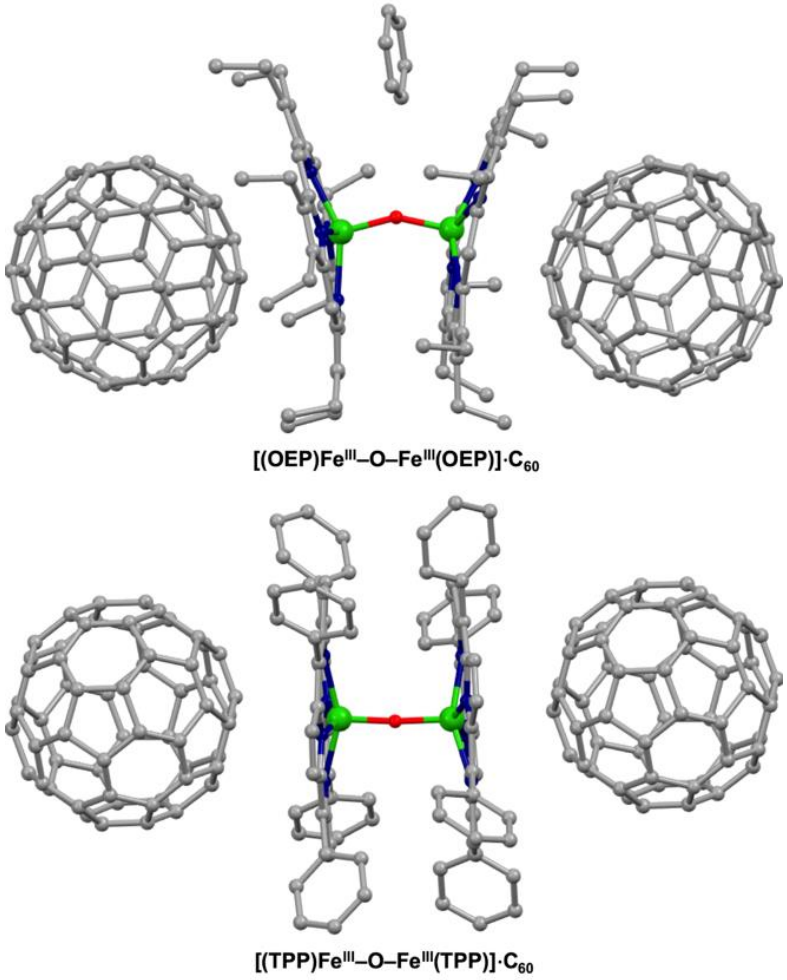

Figure 1.6. Molecular structures of [(P)Fe^{III}–O–Fe^{III}(P)]·C$_{60}$ complexes in which a *μ*-oxo heme dimer is packed between two fullerene molecules. Recreated with permission from Refs. [65,67]. Copyright 2003 American Chemical Society and 2016 John Wiley & Sons, Inc.

The water-soluble *μ*-oxo heme dimer, [(TMPyP)Fe^{III}–O–Fe^{III}(TMPyP)]$^{8+}$, has also been used to induce aggregation of the solid or hollow gold nanospheres into a plasmonic nanoparticle network. Detailed spectroscopic and microscopic measurements of the resulting plasmonic nanoparticle networks supported the “edge-on” configuration in which both heme planes of the *μ*-oxo heme dimer align parallel to the interparticle axis, thus separating the gold nanoparticles by about 1.5 nm which consequently leads to a red-shifted coupled plasmon mode [111]. Here, four methylpyridinium groups (two from each porphyrin ring) are electrostatically adsorbed on the surface of each nanoparticle, see Fig. 1.7.

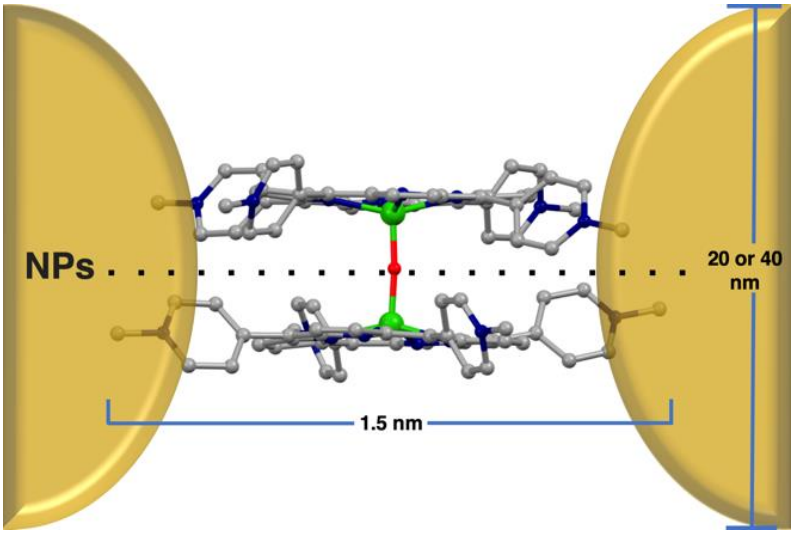

Figure 1.7. Plasmonic nanoparticle networks with the “edge-on” configuration where the Fe–O–Fe bond of a *μ*-oxo heme dimer is perpendicular to the interparticle axis of two gold nanoparticles as reported in Ref. [111].

Yip and coworkers have recently reported a pH-responsive molecular cage that can reversibly undergo conformational transitions shown in Fig. 1.8. The molecular cage, $\{Au_8(\mu\text{-PAnP})_4[(TPyP)Fe^{III}(H_2O)_2]_2(CF_3O_3S)_2\}^{8+}$, readily self-assembles from two cofacial $[(TPyP)Fe^{III}(H_2O)_2]$ complexes and four gold clips, $[Au_2(PAnP)Cl_2]$. Under basic conditions, the formation of a bridging oxo moiety leads to contraction of the cage and twisting of the two heme cores to minimize the steric hindrance. In the resulting *μ*-oxo heme dimer, $\{Au_8(\mu\text{-PAnP})_4[(TPyP)Fe^{III}\text{–O–}Fe^{III}(TPyP)]\}^{8+}$, the two ferric heme sites stay tethered by the four gold clips. The formation of the oxo-bridge accompanies significant conformational changes both in height of the molecular cage (i.e., contraction from 8.6 to 4.4 Å) and twist angle for the two porphyrin rings (i.e., going from a nearly eclipsed conformation to a bridged structure with a dihedral angle of 20°) [64]. A recent report by Schiemann and coworkers also explained a new class of *μ*-oxo heme dimer structures bearing a nitroxide (i.e., stable cyclic radical) pendant arm on each heme core, in which the dynamics of the heme cores and appendages were studied by EPR spectroscopy as well as quantum chemistry based molecular dynamics simulations. The internal structure and dynamics of these *μ*-oxo heme dimers in solution resemble the motion of a step motor [112].

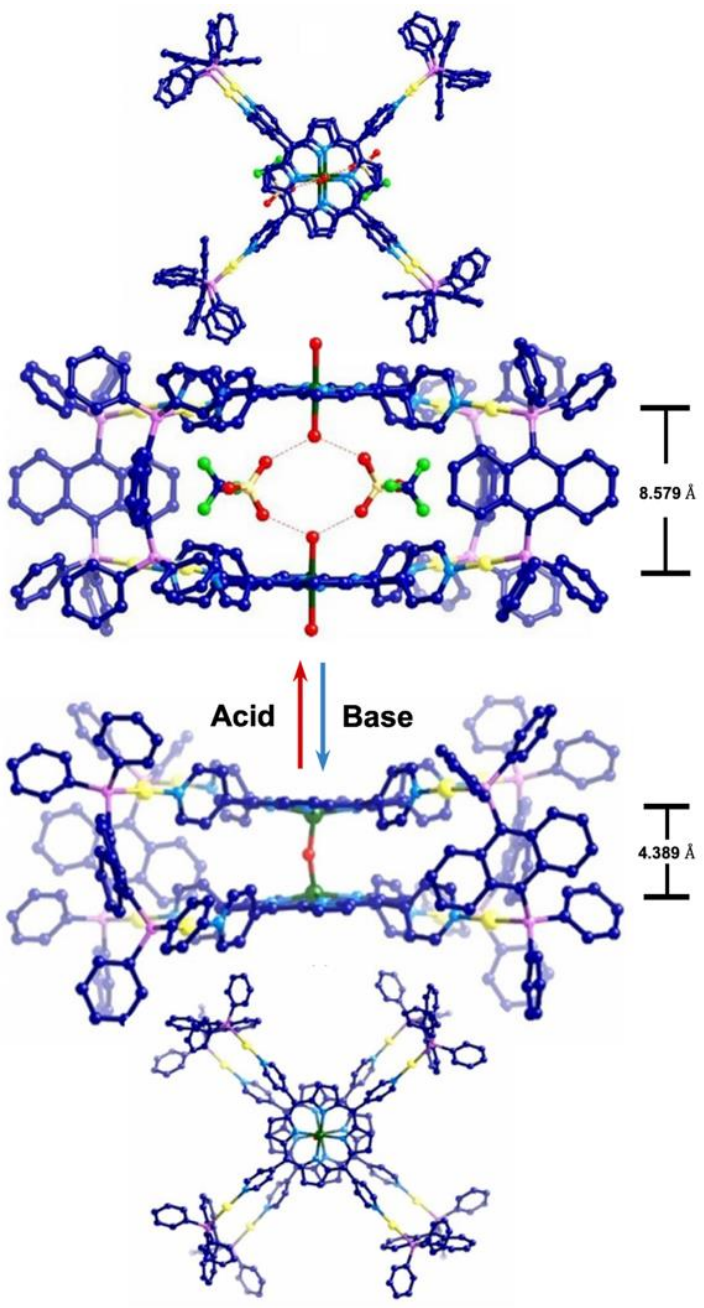

Figure 1.8. The pH-responsive molecular cage reversibly undergoes conformational transitions; e.g., the presence of a base promotes the formation of the *μ*-oxo gold-clip complex, {[Au_8(*μ*-PAnP)$_4$[Fe_2(*μ*-O)(TPyP)$_2$]}(CF_3O_3S)$_8$, thus inducing contraction of the porphyrin interplane distance. Recreated with permission from Ref. [64]. Copyright 2018 John Wiley & Sons, Inc.

Other mixed-metal self-assemblies have also been developed using a similar approach where coordination bonds such as metal-pyridyl interactions are employed to assemble

highly ordered porphyrin structures. For example, Imamura and coworkers prepared two novel hexaporphyrin constructs through introduction of the two pyridyl groups into the *meso* positions of each porphyrin ring in the *μ*-oxo heme dimer. Each pyridyl group coordinates to a ruthenium porphyrin unit forming the two hexaporphyrins, $[Ru(OEP)(CO)]_4[Fe(\textit{cis}\text{-}4\text{-}Py_2T_2P)]_2O$ and $[Ru(OEP)(CO)]_4[Fe(\textit{trans}\text{-}4\text{-}Py_2T_2P)]_2O$ [30].

Shinkai and coworkers reported another class of modified *μ*-oxo heme dimers for the boronic-acid-based saccharide recognition. Here, the peripheral boronic acid substituents on the porphyrin rings can act as the sugar-binding sites. Remarkably, these highly selective and sensitive “sugar tweezers” exhibit large association constants (10^4 to 10^5 M^{-1}) with *D*-glucose and *D*-galactose. The saccharide-binding process triggers chiral twisting of the two heme sites which can be readily monitored by circular dichroism (CD) spectroscopy [113,114].

Further work has also demonstrated that the *μ*-oxo heme dimers can serve as useful platforms for construction of responsive materials such as dynamic macrocyclic polymers, hydrogels, or ion-sensitive membrane electrodes [115]. These *μ*-oxo constructs are especially promising for pH sensing due to the ability of the bridging oxo moiety to reversibly undergo protonation and deprotonation, thus bond breakage (i.e., opening process) or formation (i.e., closing process) at various pH values can take place. For example, Deffieux and Schappacher have investigated a reversible unimolecular macrocyclization method (i.e., end-to-end cyclization reaction) using polystyrenes or poly(ethylene oxide)s with terminal ferric heme groups. For the linear ferric precursors, macrocyclization takes place through hydrolysis of ferric heme ends which is followed by intramolecular condensation to form a stable *bis*-iron *μ*-oxo porphyrin and an assembly of a cyclic polymer ring. The addition of hydrochloric acid to the green cyclic polymer solution, in turn, regenerates the red-brown linear polymer chain with the ferric heme chloride end groups, see Scheme 1.2 [116,117]. The authors also explored a reversible on-and-off switching between the linear and cyclic polymer architectures using a redox process. Here, upon exposure to air, the terminal ferrous heme groups of the linear precursor instantly react with O_2 to form the *bis*-iron *μ*-oxo porphyrin closing the polymer ring [117]. In another study, a similar approach was extended to the dynamic hydrogels

through the incorporation of the terminal ferric heme groups on a 4-arm poly(ethylene oxide) derivative. Hydration of the modified polymer in the presence of a base results in formation of *bis*-iron *μ*-oxo porphyrins, thus chemical crosslinking and swelling of the gel. Here again, acidification of the hydrogels leads to breakage of the Fe–O–Fe crosslinks that regenerates a dynamic network [118].

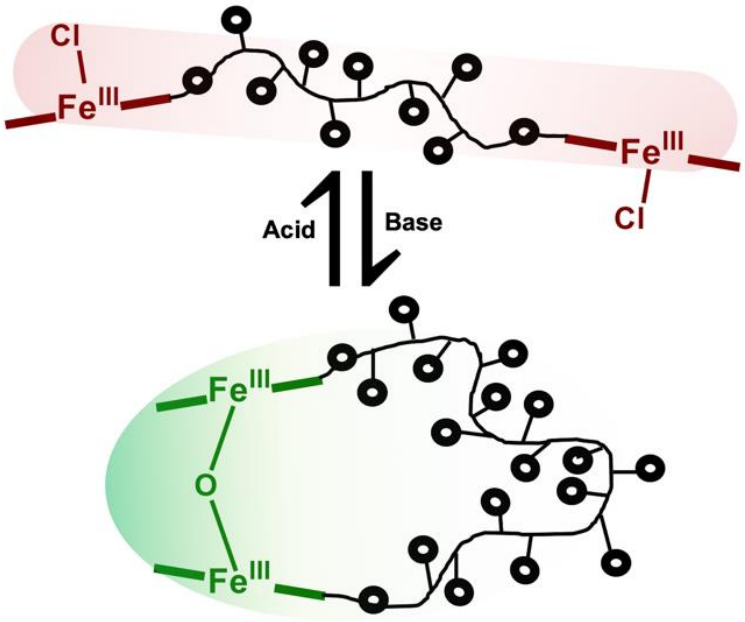

Scheme 1.2. Reversible on-and-off switching between the linear and cyclic polymer architectures as a function of pH, accompanied by a color change.

Additionally, ultrafine nanorods of the organic-soluble *μ*-oxo heme dimer, [(TPP)Fe^{III}–O–Fe^{III}(TPP)] [119], and nanocomposites of graphitic carbon nitride sheets modified with the *μ*-oxo heme dimer (i.e., [(TPP)Fe^{III}–O–Fe^{III}(TPP)]-*g*-C_3N_4) [120] have been developed as photocatalysts for the heterogeneous hydrogen evolution reactions in aqueous media.

BIOLOGICAL RELEVANCE

The *μ*-oxo heme dimer complexes of ferriprotoporphyrin IX have been proven to play critical roles in the molecular mechanism of the chronic infectious gum disease called periodontitis as well as the mechanism of action for antimalarial activity of both quinoline- and non-quinoline-based drugs. The black-pigmented periodontopathogen,

Porphyromonas gingivalis, is a heme using bacterium responsible for the adult periodontitis and displays optimum growth at pH = 7.5 – 8. Several proteins expressed by *P. gingivalis* are engaged in the degradation of the host hemoglobin and final uptake of the ferriprotoporphyrin IX cofactor. Interestingly, Smalley and coworkers have shown that *P. gingivalis* is capable of promoting the formation the *μ*-oxo heme dimers through various pathways. The stacking of the [(PPIX)Fe^{III}–O–Fe^{III}(PPIX)] complexes through weak *π*-bonding interactions eventually leads to larger molecular aggregates which deposit on the bacterial cell surface, protecting *P. gingivalis* against hydrogen peroxide through catalase activity [121,122].

Several other studies have indicated that the degradation of hemoglobin by the malaria parasite, *Plasmodium falciparum*, also releases the ferriprotoporphyrin IX. The released ferric heme is toxic to *P. falciparum* (i.e., due to the lack of a heme oxygenase pathway in the parasite), so it is mostly detoxified by sequestration into the nontoxic crystalline hemozoin (i.e., the optically dense “malaria pigment” in the infected red blood cells) [123]. A combination of X-ray crystallography, NMR, resonance Raman, Mössbauer, and UV−vis absorption spectroscopies has revealed that the antimalarial drugs significantly inhibit the hemozoin crystallization process through the strong “head-on” interactions with the uncrystallized [(PPIX)Fe^{III}–O–Fe^{III}(PPIX)] complexes, see Fig. 1.9 [124-126]. The large amounts of soluble drug-bound *μ*-oxo heme dimer adducts oxidatively damage and eventually kill the parasites.

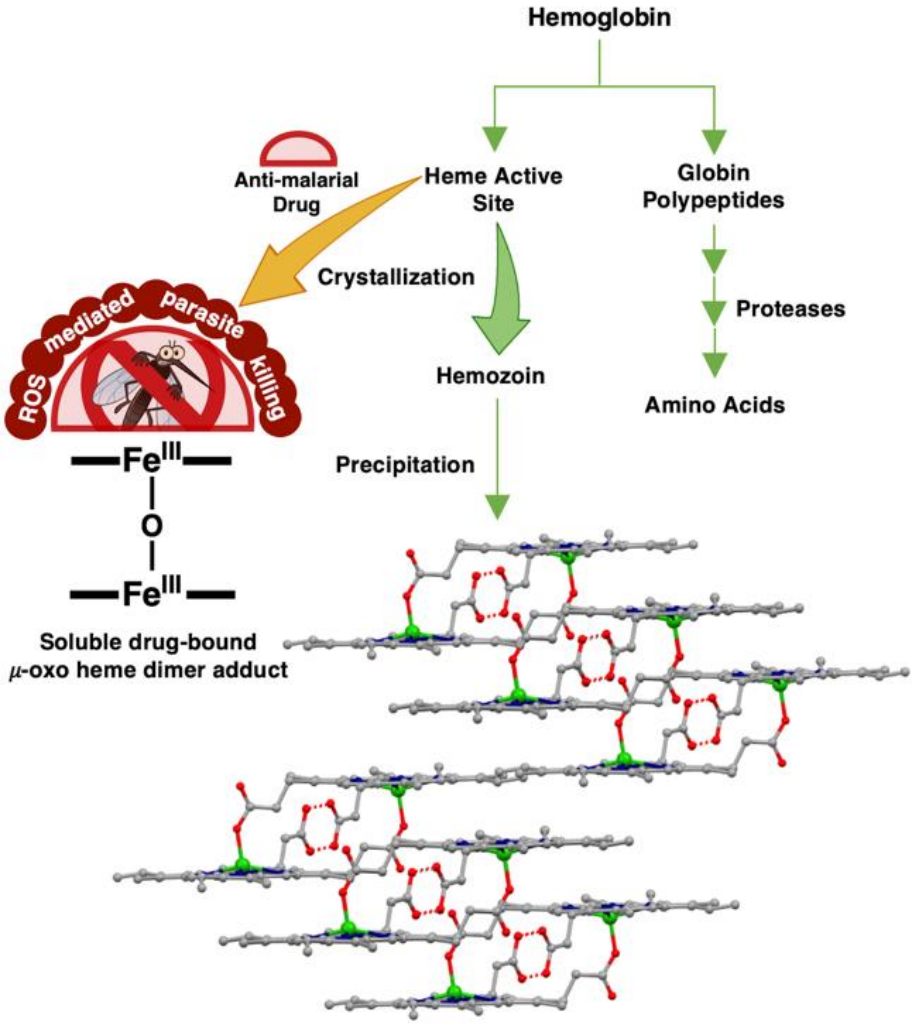

Figure 1.9. During hemoglobin degradation in *P. falciparum,* the toxic heme cofactor is released. Thus, the malarial parasite crystallizes the heme to nontoxic hemozoin. An effective antimalarial drug prevents the hemozoin crystallization process through strong "head-on" interactions with the uncrystallized *μ*-oxo heme dimer (i.e., forming the soluble drug/[(PPIX)Fe^{III}–O–Fe^{III}(PPIX)] adduct) as described in Ref. [123].

Oxo-Bridged Homobinuclear Herteroleptic Systems: [(P)Fe^{III}–O–Fe^{III}(L)]

The inherent stability of homobinuclear, homoleptic *μ*-oxo heme complexes, [(P)Fe^{III}–O–Fe^{III}(P)], has been extensively evaluated, *vide supra* [15,80,82]. The very same stability that has enabled the synthesis of a plethora of *μ*-oxo heme dimers imposes a hurdle for the synthesis of homobinuclear, heteroleptic complexes as is evident by the limited

examples of this class of constructs. The first novel approach toward the synthesis of an asymmetric *bis*-iron(III)-*μ*-oxo complex, differing in the metal coordination environment, was employed by WysŁouch and coworkers. The authors reported the first example of an *N*-substituted porphyrin, and thereupon formation of the $[(NCH_3TPP)Fe^{III}–O–Fe^{III}(TPP)]^+$ complex. Methylation of a nitrogen within the porphyrin ring decreases the Fe–O–Fe' angle by about 9° compared to that of the parent *μ*-oxo complex, $[(TPP)Fe^{III}–O–Fe^{III}(TPP)]$, see Table 1.1. The interaction between the ferric and methylated nitrogen atom is also weaker than other Fe–N bonds in the $[(NCH_3TPP)Fe^{III}–O–Fe^{III}(TPP)]^+$ complex [51].

The synthesis of another category of the $[(P)Fe^{III}–O–Fe^{III}(L)]$ constructs was inspired by the heme/non-heme diiron core of the nitric oxide reductase (NOR) active site. NOR catalyzes the two-proton, two-electron reduction of two nitric oxide ($NO_{(g)}$) molecules to nitrous oxide (N_2O) and water; this reaction plays a crucial role in bacterial denitrification [127,128]. The presence of a *μ*-oxo heme/non-heme diiron center in the fully oxidized state of the NOR active site was confirmed by Moënne-Loccoz and coworkers using resonance Raman and EPR spectroscopies [129-131]. The ligand frameworks for the bioinspired synthetic models of NOR are developed based on the *meso*-substituted porphyrin, F_8TPP, scaffold and the tripodal nitrogen ligand, tris(2-pyridylmethyl)amine (TMPA) that are able to accommodate the heme and non-heme iron sites, respectively. The asymmetric *μ*-oxo complexes of these NOR synthetic models can be prepared by either acid–base chemistry of the fully oxidized constructs or by reaction of the fully reduced binuclear systems with O_2 [47,48]. The first example of a synthetic *μ*-oxo heme/non-heme diiron system was developed by Karlin and coworkers via an acid-base self-assembly reaction of the oxidized components, $[(F_8TPP)Fe^{III}(OH)]$ and $[(TMPA)Fe^{III}(Cl)_2]^+$, in the presence of a base, forming $[(F_8TPP)Fe^{III}–O–Fe^{III}(Cl)(TMPA)]^+$ [48].

TETHERED SYSTEMS

Two covalently tethered *bis*-Fe(III) *μ*-oxo heme/non-heme systems, with the ^{5}L and later ^{6}L ligand platforms, that are closely related to the parent untethered system,

[(F_8TPP)Fe^{III}–O–Fe^{III}(Cl)(TMPA)]$^+$, were also reported by Karlin and coworkers. For [(^{5}L)Fe^{III}–O–Fe^{III}(Cl)]$^+$, the ligand scaffold facilitates intramolecular generation of a *μ*-oxo bridge between two uniquely coordinated metal sites, see Fig. 1.10 [48,132]. Both [(F_8TPP)Fe^{III}–O–Fe^{III}(Cl)(TMPA)]$^+$ and [(^{5}L)Fe^{III}–O–Fe^{III}(Cl)]$^+$ deviate from the near-linear Fe–O–Fe tendencies observed in the related *μ*-oxo heme dimers. While the [(F_8TPP)Fe^{III}–O–Fe^{III}(F_8TPP)] dimer exhibits an angle of 178°, the Fe–O–Fe' cores in the untethered and tethered heme/non-heme systems are considerably bent (i.e., 157° and 158°, respectively) [48].

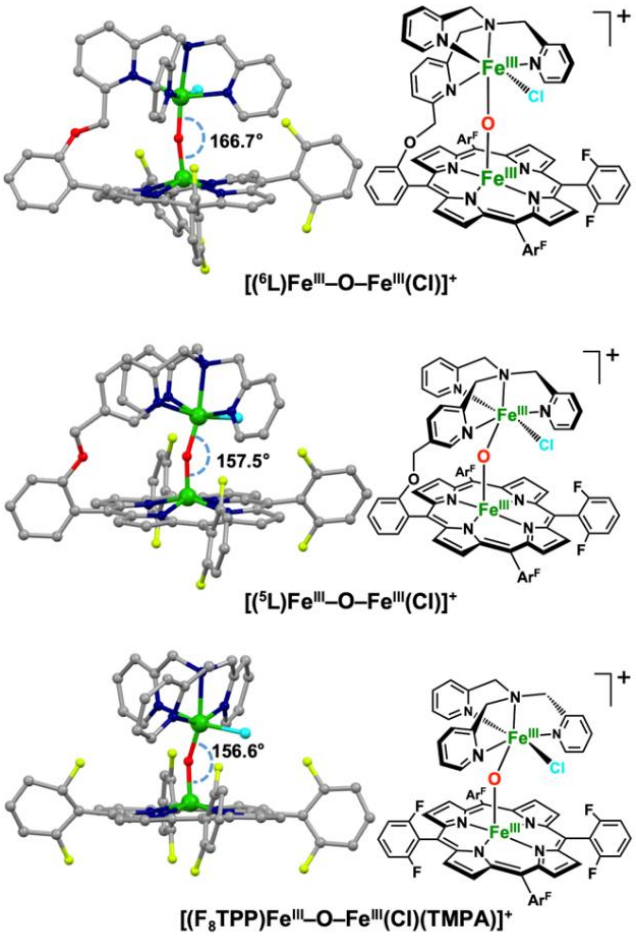

Figure 1.10. Structures of tethered and untethered synthetic *μ*-oxo heme/non-hem diiron complexes discussed in this review.

The X-ray crystal structure of the second tethered system, [(^{6}L)Fe^{III}–O–Fe^{III}(Cl)]$^+$, much like [(^{5}L)Fe^{III}–O–Fe^{III}(Cl)]$^+$, reveals an intramolecular bridging Fe–O–Fe' moiety that is

less bent (i.e., ∠Fe–O–Fe' = 167°) than those of the *μ*-oxo complexes of the ^{5}L or untethered analogues (Fig. 1.10) [47]. Here, the length of the linker and anchoring location to the pyridyl ring of the non-heme site directly dictates the flexibility of the tethered non-heme iron chelate and the degree to which the Fe–O–Fe' moiety bends.

CATALYSIS

Later, Karlin, Meyer and coworkers investigated the photophysics of $[(^{6}L)Fe^{III}–O–Fe^{III}(Cl)]^{+}$ for both stoichiometric and catalytic oxidation of substrates. Anaerobic and aerobic conditions were probed and the transfer of the bridging oxo ligand to various substrates was investigated by ^{18}O-labeling experiments. Under an anaerobic condition, with a suitable substrate present, the photodisproportionation can take place to generate the proposed transient intermediates, $[(^{6}L)Fe^{IV}=O...Fe^{II}(Cl)]$ or $[(^{6}L)Fe^{II}...O=Fe^{IV}(Cl)]$, followed by oxidation of the substrate and formation of the reduced diiron complex, $[(^{6}L)Fe^{II}...Fe^{II}(Cl)]^{+}$. In turn, the intermediates can readily undergo recombination to regenerate the starting *μ*-oxo complex, $[(^{6}L)Fe^{III}–O–Fe^{III}(Cl)]^{+}$, when no substrate is available for the oxygen transfer (OAT). In benzene, oxygen atom transfer does not occur without an exogenous substrate such as triphenylphosphine. The very strong C–H bonds in benzene are not reactive enough toward photooxidation by the heme/non-heme complex. By contrast, toluene and tetrahydrofuran (THF) both enable the photoreduction of $[(^{6}L)Fe^{III}–O–Fe^{III}(Cl)]^{+}$ to $[(^{6}L)Fe^{II}...Fe^{II}(Cl)]^{+}$ as both contain more reactive C–H bonds than those found in benzene. Here, the transiently formed ferryl-oxo species homolytically cleaves the C–H bond of toluene or THF. Exposing these OAT reactions to the air regenerates the *μ*-oxo complex from the reduced form, $[(^{6}L)Fe^{II}...Fe^{II}(Cl)]^{+}$. The newly reformed $[(^{6}L)Fe^{III}–O–Fe^{III}(Cl)]^{+}$ complex thus serves as a catalyst for the continued oxidation of triphenylphosphine, toluene, or THF [133].

Additionally, $[(^{6}L)Fe^{III}–O–Fe^{III}(Cl)]^{+}$ was subjected to neat, chlorinated substrates (e.g., 1,2-dichlorobenzene and chlorobenzene) and exogenous chlorinated substrates (e.g., benzyl chloride) in benzene. Upon photolysis, the aromatic C–Cl bond cleavage reactions proceed to form biphenyl trichlorides or biphenyl monochlorides from dichlorobenzene and chlorobenzene, respectively, while the photochemical oxidative dechlorination of the

benzylic C–Cl bond in benzyl chloride leads to the formation of benzaldehyde in 70% yield. After initial dechlorination, however, the fully oxidized *μ*-oxo heme/non-heme complex was not regenerated; instead, the chlorinated complex, $\{[(^6L)Fe^{III}(Cl)...Fe^{III}(Cl)]_2O\}^{2+}$, involving two tethered systems with a heme/non-heme bridging oxo was formed and characterized via UV-vis spectroscopy and electron spray ionization mass spectrometry (ESI-MS) [133]. The “additional” chloride ligand in the complex compared to the starting *μ*-oxo compound is derived from the substrates and hinders the reformation of the parent $[(^6L)Fe^{III}–O–Fe^{III}(Cl)]^+$ complex under aerobic conditions [133].

Recently, a *bis*-iron(III) *μ*-oxo porphyrin/phthalocyanine (P/Pc) complex, $[(P)Fe^{III}–O–Fe^{III}(Pc)]$, has been shown to catalyze the reduction of O_2 to water. To increase the efficiency of O_2 reduction, iron cores and highly flexible linkers were both incorporated into the ligand scaffold, see Fig. 1.11. The formation of the *μ*-oxo complex was corroborated by both EXAFS and DFT studies, supporting the presence of a greatly bent Fe–O–Fe moiety (146°); furthermore, fitting of Fe K-edge EXAFS data gave Fe–O and Fe–Fe distances of 1.81 and 3.47 Å, respectively, both of which were slightly elongated compared to those of the corresponding *μ*-oxo heme dimer. Electrochemical studies were conducted on the *μ*-oxo phthalocyanine/porphyrin complex as well as the corresponding *bis*-iron(III) *μ*-oxo porphyrin and phthalocyanine dimers. The onset potentials for O_2 reduction (E_o vs. a reversible hydrogen electrode (RHE)) were reported as increasingly positive in the order of: $[(P)Fe^{III}–O–Fe^{III}(P)]$ ($E_o = 0.59$ V) < $[(Pc)Fe^{III}–O–Fe^{III}(Pc)]$ ($E_o = 0.68$ V) < $[(P)Fe^{III}–O–Fe^{III}(Pc)]$ ($E_o = 0.78$ V). The *bis*-iron(III) *μ*-oxo porphyrin/phthalocyanine complex clearly exhibits the lowest overpotential compared to its homobinuclear, homoleptic counterparts. After quantification of O_2 electroreduction products (e.g., H_2O and H_2O_2), it was determined that the four-electron reduction of O_2 to water (i.e., with the yield of 88%) was the primary reaction catalyzed by the $[(Pc)Fe^{III}–O–Fe^{III}(Pc)]$ complex, selectively [134].

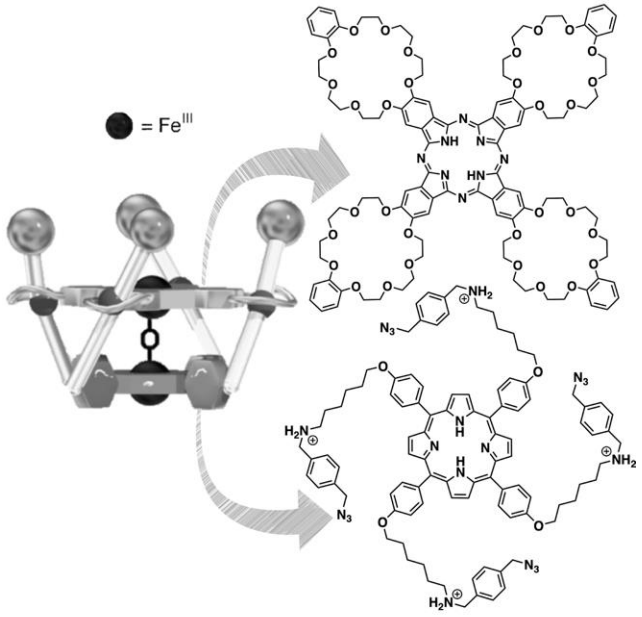

Figure 1.11. Structure of the homobinuclear, heteroleptic *bis*-iron(III) *μ*-oxo porphyrin/phthalocyanine complex. Adopted with permission from Ref.[134]. Copyright 2017 John Wiley & Sons, Inc.

Oxo-bridged Heterbinuclear Heteroleptic Systems: $[(P)Fe^{III}–O–M(L)]^{n+}$

Further interesting progress in the field of heme chemistry includes the development of a class of oxo-bridged, heterobinuclear complexes bearing a copper site in addition to the heme core, $[(P)Fe^{III}–O–Cu^{II}(L)]^{+}$. Such complexes are broadly embraced as synthetic models for the active site of cytochrome *c* oxidase in which heme-a_3 and Cu_B are adjacent to one another. As a crucial component of the electron transport chain, C*c*O catalyzes the four electron, four proton reduction of dioxygen to water and simultaneously generates the electrochemical gradient across the membrane, necessary for ATP production [54,58,59]. Karlin and coworkers have done significant work on synthetic heme/Cu models over the years and demonstrated that the related *μ*-oxo heme/Cu complexes can be prepared by dioxygen or acid−base chemistry [135-137].

The first example of such *μ*-oxo complexes was $[(F_8TPP)Fe^{III}–O–Cu^{II}(TMPA)]^{+}$ which was obtained from the reaction of an equimolar mixture of the $[(F_8TPP)Fe^{II}]$ and $[(TMPA)Cu^{I}(MeCN)]^{+}$ complexes with O_2 at room temperature. Interestingly, despite the

known substantial thermodynamic stability of the *μ*-oxo iron dimer, $[(P)Fe^{III}–O–Fe^{III}(P)]$, the kinetically stable *μ*-oxo heme/Cu complexes, $[(P)Fe^{III}–O–Cu^{II}(L)]^{+}$, are formed. Here, the bridging oxo moiety is derived from O_2 via fast thermal disproportionation of a binuclear peroxide intermediate (i.e., $[(P)Fe^{III}–(O_2^{2-})–Cu^{II}(L)]^{+}$) at room temperature, with the concomitant release of half of an equivalent of O_2 [54,138]. One exception has been reported for synthesis of $[(TMP)Fe^{III}–O–Cu^{II}(5MeTPA)]^{+}$ where the *μ*-peroxo complex remains stable for several months; over an extended period of time, it only very slowly converts to its *μ*-oxo counterpart [52]. Later, it was shown that $[(P)Fe^{III}–O–Cu^{II}(L)]^{+}$ can also be formed via mixing $[(P)Fe^{III}(OH)]$ and $[(L)Cu^{II}]^{2+}$ species [54] or alternatively $[(P)Fe^{III}]$ and $[(L)Cu^{II}(OH)]^{+}$ species [59] in the presence of a base.

Furthermore, X-ray crystallography and Fe and Cu-edge EXAFS studies on the reported $[(P)Fe^{III}–O–Cu^{II}(L)]^{+}$ complexes with the tripodal tetradentate chelates indicated a near-linear Fe–O–Cu arrangement. Mössbauer, EPR, and magnetic susceptibility studies also revealed the strong antiferromagnetic coupling of the high-spin Fe^{III} ($S = {}^{5}/_{2}$) and Cu^{II} ($S = {}^{1}/_{2}$) sites through the *μ*-oxo moiety, rendering an overall spin state of S = 2 [54,59]. The *μ*-oxo heme/Cu complexes also exhibit the very distinctive red-shifted Soret absorption bands (i.e., λ_{max} ~ 435−455 nm, see Table 1.1) compared to those of classical high-spin ferric hemes. The weaker affinity of Cu(II) for the bridging oxo, and therefore the greater degree of *π* charge donation available onto the ferric center by the oxo group, is likely responsible for the characteristic red-shift.

The bridging oxo moiety can be reversibly protonated to give the corresponding *μ*-hydroxo complex, $[(P)Fe^{III}–(OH)–Cu^{II}(L)]^{+}$, and with protonation, bending of the Fe–O(H)–Cu moiety and lengthening of the Fe^{III}−O(H) and Cu^{II}−O(H) bonds occurs, which consequently lowers the degree to which the iron atom is pulled out of the porphyrin plane [54,139,140]. Holm and coworkers reported the only crystal structure of a *μ*-hydroxo heme/Cu complex utilizing the OEP framework (i.e., $[(OEP)Fe^{III}–(OH)–Cu^{II}(Me_5dien)(OClO_3)]^{+}$) [60]. In this complex, the Fe–(OH)–Cu angle is about 157° which is significantly more bent compared to the Fe–O–Cu angle (i.e., 177°) in the related *μ*-oxo heme/Cu complex based on the OEP scaffold, $[(OEP)Fe^{III}–O–Cu^{II}(Me_6tren)]^{+}$ [54,60]. Note, however, that the cupric ligations in these complexes are significantly different from

one another. A similar degree of bending was reported for the protonation of $[(F_8TPP)Fe^{III}–O–Cu^{II}(TMPA)]^+$, wherein the Fe–O–Cu moiety approaches linearity (i.e., 178°) [27] and Fe–(OH)–Cu moiety is significantly more bent (i.e., 157°) as confirmed by EXAFS [139].

Markedly, studies by Karlin and coworkers have revealed that changes in the coordination environment of the cupric site, tridentate vs. tetradentate ligands, can dramatically influence both *μ*-oxo heme/Cu physical properties and reactivity [56,137]. Changing tripodal tetradentate chelates (e.g., TMPA, Me_6tren, or Me_5dien) bound to the cupric center to tridentate ligands (e.g., L^{Me2N}, MePY2, AN) results in significant bending (i.e., ∠Fe−O−Cu is 142−150°) and elevated basicity of the bridging oxo group. As discussed earlier, bending upon protonation can be explained by varying degrees of re-hybridization at the bridging oxygen atom, with the extreme case being a change from *sp* in a perfectly linear *μ*-oxo compound to sp^2 in a very bent *μ*-hydroxo complex with the angle of 120°. Consequently, protonation of the bridging oxo moieties requires varying degrees of geometric and electronic rearrangements as explained by Norton and coworkers; thus, the extent of the overall re-hybridizations can directly dictate the kinetics of the protonation reactions [11,141].

The proton transfer chemistry of an oxo-bridged heterometallic heme/Cu complex and the corresponding *μ*-hydroxo complex has been a matter of great importance for understanding the function of the C*c*O active site. Karlin and coworkers have thus determined the pK_a of the bridging hydroxo moiety in some of the synthetic $[(P)Fe^{III}–O–Cu^{II}(L)]^+$ systems, such as $[(F_8TPP)Fe^{III}–O–Cu^{II}(TMPA)]^+$ (Chart 1.2) [139] and $[(F_8TPP)Fe^{III}–O–Cu^{II}(MePY2)]^+$ (Chart 1.2) [142], through acid−base titration experiments. The tridentate cupric core in the latter resulted in a slightly more basic oxo bridge ($16.7 < pK_a < 17.6$ in CH_3CN; aqueous $pK_a \cong 9.6$) compared to that of the former bearing the tetradentate cupric site ($14 < pK_a < 17$ in CH_3CN; aqueous $pK_a \cong 8$). A comparison of the Fe–O–Cu angles shows that the *μ*-oxo complex of $[(F_8TPP)Fe^{III}–O–Cu^{II}(TMPA)]^+$ is nearly straight (178°) while that of $[(F_8TPP)Fe^{III}–O–Cu^{II}(MePY2)]^+$ is significantly bent (142°), further illustrating the aforementioned observation that as the Fe–O–Cu core becomes more bent, the bridging oxo moiety become more basic.

However, the linearity of the Fe–O–Cu core is not the only factor defining the basicity as the [(F_8TPP)Fe^{III}–O–Cu^{II}(AN)]$^+$ with a larger Fe–O–Cu core (i.e., 150°) exhibits more basicity than [(F_8TPP)Fe^{III}–O–Cu^{II}(MePY2)] with a more bent Fe–O–Cu core (i.e., 142°) [57,143].

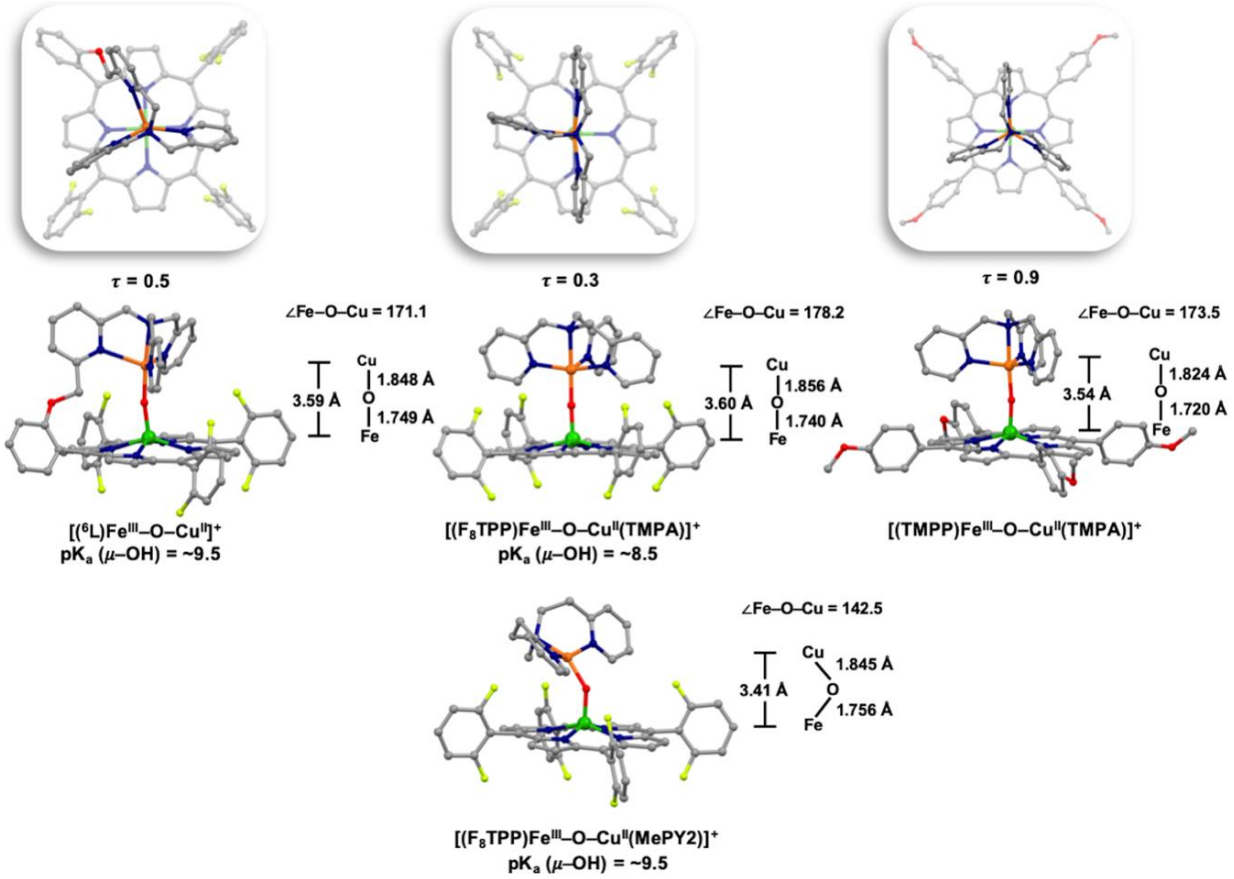

Chart 1.2. Molecular structures of *μ*-oxo heme/Cu complexes reported by Karlin and coworkers. Presented pK_a values are calculated for aqueous media using the estimate that the measured pK_a values in acetonitrile are 7.5 ± 1 unites larger than in water.

TETHERED SYSTEMS

Karlin and coworkers have also prepared several other ligand platforms for the formation of synthetic *μ*-oxo heme/Cu complexes. Two of these platforms are porphyrins bearing covalently tethered tetradentate copper chelates, ^{6}L and ^{5}L that were discussed under

the previous class of oxo-bridged heme complexes, i.e., Oxo-Bridged Homobinuclear Heteroleptic Systems. Chart 1.2 depicts the crystal structures of the untethered $[(F_8TPP)Fe^{III}–O–Cu^{II}(TMPA)]^+$ as well as its tethered analogues, i.e., $[(^5L)Fe^{III}–O–Cu^{II}]^+$ and $[(^6L)Fe^{III}–O–Cu^{II}]^+$ [58]. The *μ*-oxo heme/Cu complex of the ^5L scaffold possesses a very bent Fe−O−Cu core with an angle of ~ 141°, due to the ligand constraints imposed by the linker. This bent geometry can translate to partial sp^2 orbital hybridization of the bridging oxo moiety which can consequently facilitate a faster and more facile protonation process to form the *μ*-hydroxo complex upon the addition of an acid. The addition of 1 equivalent of a weak acid such as *N*-methylmorpholinium triflate with pK_a of 16.6 in acetonitrile does not result in protonation of the untethered $[(F_8TPP)Fe^{III}–O–Cu^{II}(TMPA)]^+$ complex, while the same acid reacts with both tethered systems generating the bridging hydroxo species for the ^6L platform, $[(^6L)Fe^{III}–(OH)–Cu^{II}]^{2+}$, and resulting in cleavage of the oxo bridge for the more strained ^5L platform to form $[(^5L)Fe^{III}–(OH)...Cu^{II}(CF_3O_3S)]^+$ [143]. Therefore, the *μ*-oxo moiety in $[(^6L)Fe^{III}–(OH)–Cu^{II}]^+$ or $[(^5L)Fe^{III}–O–Cu^{II}]^+$ is more basic than that in $[(F_8TPP)Fe^{III}–O–Cu^{II}(TMPA)]^+$, and a *μ*-hydroxo species appears inaccessible in $[(^5L)Fe^{III}–O–Cu^{II}]^+$.

Another interesting structural observation for $[(P)Fe^{III}–(O_2^{2–})–Cu^{II}(L)]^+$, with L being the tetradentate TMPA chelate, comes when comparing the ligand arrangements around the cupric centers in the parent complex, $[(F_8TPP)Fe^{III}–O–Cu^{II}(TMPA)]^+$, and its closely related analogue $[(TMPP)Fe^{III}–O–Cu^{II}(TMPA)]^+$, in which only the identity of the peripheral substituents on the porphyrin ring varies. Despite the fact that both complexes possess similar Fe–O–Cu core angles and identical cupric chelate, the copper centers adopt very different geometries. The TMPA-copper ligation, for the $[(TMPP)Fe^{III}–O–Cu^{II}(TMPA)]^+$ complex, occurs within a nearly perfect trigonal bipyramidal (TBP) geometry ($\tau = 0.9$), while for the $[(F_8TPP)Fe^{III}–O–Cu^{II}(TMPA)]^+$ construct, the copper ligand is sterically hindered due to the presence of the sizeable fluorine atoms projecting off the phenyl groups, thus the cupric center adjusts to a distorted square pyramidal (SP) coordination ($\tau = 0.3$) [54,55].

Notably, $[(^6L)Fe^{III}–O–Cu^{II}]^+$ has a slightly more TBP-like configuration ($\tau = 0.5$) than its untethered analogue, i.e., $[(F_8TPP)Fe^{III}–O–Cu^{II}(TMPA)]^+$. Given the cupric ligand is

attached to an aromatic ring on the *meso* position of the ferric heme, the two free pyridyl arms settle into a different spatial arrangement than those within the untethered heme/Cu complex, see Chart 1.2.

REACTIVITY TOWARD NITRIC OXIDE

Nitric oxide ($NO_{(g)}$) plays a critical role as a versatile signaling molecule in living organisms and can be generated through two unique pathways that are intimately dependent on physiological fluctuations in O_2 concentrations. The production of $NO_{(g)}$ takes place via the nitric oxide synthase (NOS) pathway, requiring L-arginine, during normoxic conditions; hence the added O_2 requirement for this pathway. An alternate pathway for $NO_{(g)}$ generation, required under low O_2 concentrations (i.e., hypoxic conditions) and those associated with cellular stress, is an enzymatic reduction of nitrite deemed to be important in the modulation of mitochondrial respiration [144].

Previous studies demonstrated that C*c*O is capable of nitrite reduction when exposed to hypoxic conditions [145]. Consequently, the initial report by Karlin and coworkers introduced a synthetic heme/Cu assembly mediating the redox interplay between nitrite and $NO_{(g)}$ [146]. Further studies revealed that the partially reduced form of the heme/Cu assembly facilitates nitrite reduction to $NO_{(g)}$ and the cupric center serves as a Lewis acid directing the nitrite ion to bind to the ferrous heme center through *N*-atom coordination. Additionally, the cupric site facilitates the nitrite (N−O) bond cleavage while the ferrous heme provides the reducing electron [53]. Interestingly, in turn the fully oxidized form of the same assembly as a *μ*-oxo heme/Cu complex could oxidize $NO_{(g)}$ back to nitrite. $NO_{(g)}$ oxidation to nitrite was accomplished through the addition of two equivalents of $NO_{(g)}$ to one equivalent of the fully oxidized the parent $[(F_8TPP)Fe^{III}–O–Cu^{II}(TMPA)]^+$ complex to yield $[(F_8TPP)Fe^{II}(NO)]$ and $[(TMPA)Cu^{II}(NO_2)]^+$ [146]

Further studies involved similar *μ*-oxo heme/Cu complexes with variation among the copper ligand framework. These complexes included $[(F_8TPP)Fe^{III}–O–Cu^{II}(AN)]^+$ and $[(F_8TPP)Fe^{III}–O–Cu^{II}(MePY2)]^+$. Tridentate ligands around the copper center gave similar results to those obtained with the tetradentate ligand TMPA, however, with an increase

in reactivity. Alterations in copper-ligand denticity and electronics modulate the reactivity of the *μ*-oxo heme/Cu complexes toward $NO_{(g)}$. This is perhaps achieved through regulating the steric hindrance and electronic environment surrounding the copper center and, thus tuning the basicity and accessibility of the bridging oxo moiety. Remarkably, a higher degree of bending, basicity, and accessibility of the bridging oxo moiety results in an increase in $NO_{(g)}$ oxidase reactivity.

In order to further comprehend $NO_{(g)}$ reactivity with the *μ*-oxo heme/Cu complexes, the parent porphyrin ligand F_8TPP was replaced by a more electron rich analogue TMPP, bearing strong electron-donating peripheral groups. The addition of $NO_{(g)}$ to $[(TMPP)Fe^{III}–O–Cu^{II}(TMPA)]^+$ enables the detection of an intermediate (Scheme 1.3, *bis*-NO intermediate) through UV-vis monitoring at -20 °C [55]. This intermediate isosbestically converts to the final products, $[(TMPP)Fe^{II}(NO)]$ and $[(TMPA)Cu^{II}(NO_2)]^+$, in a first-order process with rate constant $k_{dissoc.} = 6.7 \times 10^{-3}\ s^{-1}$ at −20 °C.

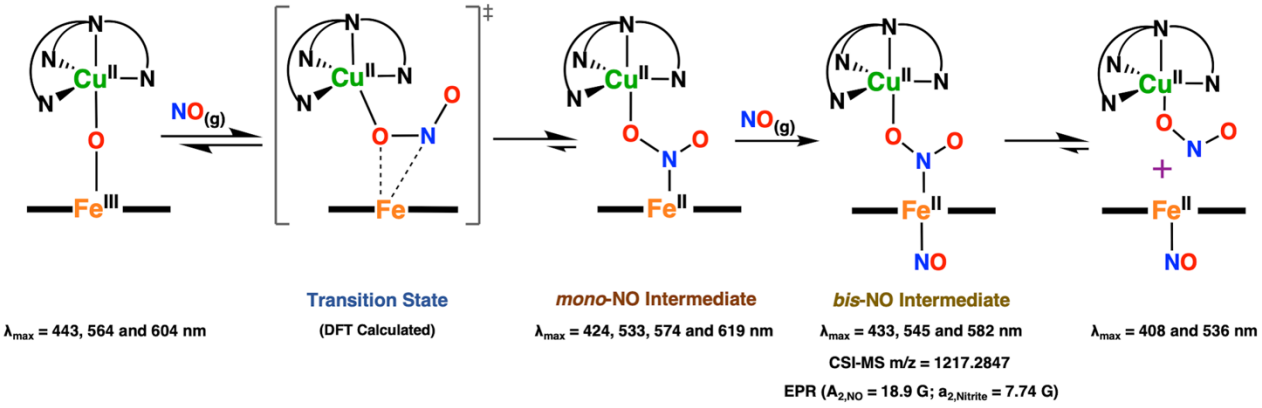

Scheme 1.3. Proposed reaction mechanism for $NO_{(g)}$ oxidase chemistry mediated by *μ*-oxo heme/Cu assemblies, $[(P)Fe^{III}–O–Cu^{II}(L)]^+$, producing observed products. Adapted with permission from Ref. [55]. Copyright 2015 American Chemical Society.

Guided by DFT calculations (i.e., proposing that the observed *bis*-NO intermediate is a ferrous species), $[(TMPA)Cu^{II}(NO_2)]^+$ was mixed with $[(TMPP)Fe^{II}(NO)]$ at –125 °C to determine if nitrite anion, as bound to a cupric site, could bind to a ferrous-nitrosyl complex. Cooling of the mixture resulted in a new UV-vis spectrum identical to that of the *bis*-NO intermediate supporting that the *bis*-NO species comprises a six-coordinate

ferrous heme-nitrosyl species joined to a cupric nitrite entity through nitrogen atom of the bridging nitrite. The exact nature of this intermediate was also confirmed by low-temperature stopped-flow kinetic and EPR spectroscopies as well as cryo-spray ionization mass spectrometry (CSI-MS) at –60 °C (see Scheme 1.3). Furthermore, the reaction proved to be reversible as temperatures rose.

An initial transition state was proposed by DFT calculations in which the formation of a three-membered chelate ring between the iron, bridging oxo, and the nitrogen (N) atom of the $NO_{(g)}$ is observed (transition state, Scheme 1.3). Formation of this a “triangular” structure happens via the electrophilic attack of the initial $NO_{(g)}$ molecule, followed by electron transfer from $NO_{(g)}$ to the ferric heme. The experimentally observed low activation enthalpy and negative activation entropy derived from the kinetic studies also support this sequence of events [55]. A *mono*-NO adduct in which there is an *N*-bound nitrite to the resulting ferrous heme and an oxygen atom bound to the cupric center is the first intermediate. This finding is of significant relevance to C*c*O as a similar ferrous heme−nitro species has been detected in the heme/Cu active-site of the enzyme by resonance Raman.

To generate the second intermediate, a second $NO_{(g)}$ molecule attacks the ferrous heme resulting in the aforementioned *bis*-NO adduct. The second $NO_{(g)}$ is not involved in the redox chemistry and only traps the ferrous heme formed during the prior step to generate a stable ferrous heme nitrosyl product. Remarkably, the binding of the second $NO_{(g)}$ is irreversible and addition of the first $NO_{(g)}$ to *μ*-oxo heme/Cu complex, $[(TMPP)Fe^{III}–O–Cu^{II}(TMPA)]^{+}$ is about an order of magnitude faster than the irreversible binding of the second $NO_{(g)}$ [55,137].

Further broadening the scope of oxo-bridged heterobinuclear heteroleptic systems points to complexes in which the non-iron metal center is comprised of either Cr or Co. The first oxo-bridged heme/Cr complex crystal structure was deposited by West and coworkers for $[(TMPP)Fe^{III}–O–Cr^{III}(Py)(TPP)]$ [62]. Later, Tsuchida and coworkers crystallized another complex, $[(TPP)Fe^{III}–O–Cr^{III}(Pip)(TPP)]$, that closely resembles the former $[(P)Fe^{III}–O–Cr^{III}(P')(L)]^{+}$ [61]. Exchanging the TMPP ligand for a second TPP had little

effect on the Fe–O–Cr moiety, both having a near-linear angle of about 178°, see Table 1.1; however, the twist angle between the two porphyrins slightly decreases in [(TPP)Fe^{III}–O–Cr^{III}(Pip)(TPP)] as opposed to that of [(TMPP)Fe^{III}–O–Cr^{III}(Py)(TPP)] (i.e., 30° and 32°, respectively), perhaps as a subtle measure to decrease the interaction between the phenyl groups of the heme and the phenyl groups of the chromium-bound porphyrin. The observed change in the twist angle is due to shorter the Fe–M distance for [(TPP)Fe^{III}–O–Cr^{III}(Pip)(TPP)] than that of [(TMPP)Fe^{III}–O–Cr^{III}(Py)(TPP)] (i.e., 3.53 and 3.60 Å, respectively) and in part consequence of the varying nature of the axial ligands binding to the chromic cores. As expected, the [(P)Fe^{III}–O–Cr^{III}(P')(L)]$^+$ complexes exhibit considerable antiferromagnetic coupling between Cr(III) ($S = {}^3/_2$) and Fe(III) ($S = {}^5/_2$) consistent with an assignment of 1 as an S = 1 electronic ground state species.

In addition to [(P)Fe^{III}–O–Cr^{III}(P')(L)]$^+$ complexes, one oxo-bridged crystal structure involving a cobalt core instead of a chromium site has been reported by Karlin and coworkers, that of [(F_8TPP)Fe^{III}–O–Co^{II}(TMPA)]$^+$ [63]. While O_2 chemistry with the parent [(F_8TPP)Fe^{III}–O–Cu^{II}(TMPA)]$^+$ complex gave a peroxo-bridged heme/Cu complex, identification of a peroxo-bridged heme/Co complex was not possible. Furthermore, there is a greater degree of bending in the Fe–O–M moiety than that of in the parent complex, [(F_8TPP)Fe^{III}–O–Cu^{II}(TMPA)]$^+$ (i.e., ∠Fe–O–Co is 172° and ∠Fe–O–Cu is 178°, respectively). Lastly, the Fe–O distance for [(F_8TPP)Fe^{III}–O–Co^{II}(TMPA)]$^+$ (1.75 Å) is between those of the parent compounds, [(F_8TPP)Fe^{III}–O–Cu^{II}(TMPA)]$^+$ (1.74 Å) and [(F_8TPP)Fe^{III}–O–Fe^{III}(TMPA)]$^+$, (1.78 Å) and the Co core adopts a trigonal bipyramidal surrounding while the cupric center in the parent complex accommodates a distorted square pyramidal geometry.

Rezzano and coworkers have also reported iron/copper porphyrin-based nanostructures with the positively and negatively charged porphyrins for sensor application. The J-aggregates of those porphyrins are stabilized by Fe–O–Cu bonds, electrostatic forces, and *π*-stacking interactions. The Raman features of these supramolecular assemblies can be used for sensing a variety of species such as H_2O_2, NO_2^-, SO_3^{2-}, and N_3^-. The authors proposed that the putative [(T_4PyP)Fe^{III}–O–Cu^{II}(T_4PyP)]$^{7+}$ units are stacked by the neighboring [H_4TPPS]$^{2-}$ complexes [147]. The proposed [(P)Fe^{III}–O–Cu^{II}(P)]$^{n+}$

complex would be the only example of an oxo-bridged heterobinuclear homoleptic system.

Conclusion

From the results presented herein, it is evident that the chemistry of (hydr)oxo-bridged heme complexes spans studies in synthetic inorganic chemistry, biology, materials science, energy and environmental sciences. In order to develop a detailed understanding of their structure-functions relationships, it is necessary to integrate perspectives and techniques from all subdisciplines. We have highlighted the recent progress and contributions in synthesis, structural and spectroscopic investigations, and reactivity and catalytic studies of a variety of (hydr)oxo-bridged heme constructs. The wealth of (hydr)oxo-bridged binuclear structures in the Cambridge Structural Database, and detailed studies of the functions and properties of these assemblies explain the increasing prevalence of the (hydr)oxo-bridged heme constructs in a very wide range of industrial applications such as homogenous or heterogenous catalysis, sensing, optoelectronics, or their involvement in healthcare.

As we point out, the properties and reactivity of the bridging (hydr)oxo moieties are controlled by the coordination environment of the heme core, the nature of the second metal center attached to the (hydr)oxo group and its and chelating scaffold, and the flexibility or rigidity of the entire framework. Further investigations and deeper understanding of the properties and reactivities of these (hydr)oxo-bridged heme constructs are likely to improve their performance and may uncover many additional applications.

Abbreviations

TPP: tetraphenylporphyrin
Porphen: (5,10-(1,10-phenanthroline-2,9-diyl)-*bis*(4-phenylene-2-phenyl)porphyrinato)
$TPPBr_4$: (2,3,12,13-tetrabromo-5,10,15,20-tetraphenylporphyrinato
TTP: *meso*-tetrakis(*p*-tolyl-porphyrinato)

TMPyP: tetrakis(1-methylpyridinium-4-yl)porphyrinato

TPPS: tetrakis(4-sulfonatophenyl)porphyrinato

p-CTPP: (5,10,15,20-tetra(4-chlorophenyl)porphyrinato

TBPP: tetrakis(*p*-bromophenyl-porphyrinato

FF: Face-to-Face *aka* 5-(*o*-aminophenyl)-10,15,20-triphenylporphyrin

$TPPF_5$: (5,10,15,20-tetrakispentafluorophenyl)porphyrinato

F_8TPP: tetrakis(2,6-difluorophenyl)porphyrinate

OC_2OPor: four-atom-linked capped porphyrin

OEP: 2,3,7,8,12,13,17,18-octaethylporphyrinato

trans-4-Py_2T_2: 5,15-di(4-pyridyl)-10,20-ditolylporphyrinato

cis-4-Py_2T_2: 5,10-di(4-pyridyl)-15,20-ditolylporphyrinato

DEsP: diester porphyrin

ODM: 5,15-dimethyl-2,3,7,8,12,13,17,18-octaethylporphyrin

TCPP: *meso*-tetra(4-carboxyphenyl)porphyrin

din-OEP: 5,10-dinitrooctaethylporphyrin or 5,15-dinitrooctaethylporphyrin

trn-OEP: 5,10,15-trinitrooctaethylporphyrin

tn-OEP: 5,10,15,20-tetranitrooctaethylporphyrin

PPIXDME: protoporphyrin IX dimethyl ester

DEP: diethylpyrrole-bridged *bis*-porphyrin

ETA: ethane-linked *μ*-oxo *bis*-octaethylporphyrin

ETE: 1,2-*bis*(2,3,7,8,12,13,17,18-octaethylporphyrinnyl)ethene

DPD: (dibenzofuran-2,9-diyl)-*bis*((3,8,12,17-tetraethyl-2,7,13,18-tetramethylporphyrinato

DPA: 2,8,13,17-tetraethyl-3,7,12,18-tetramethylporphyrin-5-yl)anthracene

DPX: 2,8,13,17-tetraethyl-3,7,12,18-tetramethylporphyrin-5-yl)-9,9-dimethylxanthene

^6L: 5-(*o*-*O*-[(*N*,*N*-*bis*(2-pyridylmethyl)-2-(6-methoxyl)pyridinemethanamine)phenyl]-10,15,20-tris(2,6-difluorophenyl)porphine

^5L: *α,β,γ-tris*(2,6-Difluorophenyl)-*δ*-(((2-(*bis*(2-pyridylmethyl)amino)methyl-5-pyridyl)methoxy)phenyl)porphyrinato

TMPA: *tris*(2-pyridylmethyl)amine

NCH_3TPP: *N*-methyl-5,10,15,20-tetraphenylporphyrinato

TMP-5MeTPA: 10,15,20-*tris*(2,4,6-trimethylphenyl)-5-(2'-*bis*((5"-methyl-2"-pyridylmethyl)aminomethyl)pyridine-5'-carboxylic-aminophenyl) porphyrinate(2−)

MePY2: *bis*(2-pyridyl-ethyl)methylamine

L^{Me2N}: *N,N-bis*{2-[2-(*N',N*'-4-dimethylamino)pyridyl]ethyl}methylamine)

AN: 3,3'-imino-*bis*(N,N-dimethylpropylamine)

Me_6tren: *tris*[(*N,N*-dimethylamino)-ethyl]amine

Me_5dien: 1,1,4,7,7-pentamethyldiethylenetriamine

PAnP: 9,10-*bis*(di-phenylphosphino)anthracene

TPyP = *meso*-tetra(4-pyridyl)-porphyrinato

P = porphyrinate dianion

Pc = phthalocyaninate dianion

CHAPTER II: A SERIES OF *TETRAKIS*(PENTAFLUOROPHENYL)BORATE SALTS OF PROTONATED NITROGEN BASES: OBSERVING THE SPIN-SPIN COUPLING OF THE ^{14}N COUPLED ACIDIC PROTONS WITH ^{1}H NMR SPECTRA

The following work was accomplished with the aid of Firoz S. T. Khan and Shabnam Hematian.

Abstract

The present investigation describes a general preparation of protonated amines, or nitrogen bases, having the weakly-coordinating counteranion pentafluoro-substituted *tetra*-phenylborate, $[B(C_6F_5)_4]^-$. These have been spectroscopically characterized through ^{1}H- and ^{19}F-NMR as well as IR spectroscopies. Interestingly, the ^{1}H-NMR spectra highlight a distinguished triplet splitting pattern for the N-H proton of protonated amines due to ^{14}N-^{1}H coupling. The chemical shifts and ^{14}N-^{1}H coupling constants ($^{1}J_{NH}$) correlate well with the pK_a of the respective protonated amines and, most importantly, can be used to identify the site of nitrogen protonation based on nitrogen hybridization; this becomes useful in biological molecules or nitrogen based chelates in which there are multiple nitrogen sites available for protonation. The solid structure of the crystallized acids displays hydrogen bonds between the protonated amines and the co-crystallized solvent, diethyl ether, in the crystal lattice. Due to the weaker coordinating tendency of $[B(C_6F_5)_4]^-$, the protonated amines can be well utilized for chemical transformations in lower-polarity media.

Introduction

The ability to accept or donate a proton is one of the highly important fundamental properties of a molecule which serves as a tool to gain insight into many chemical and biochemical reactions.[148] This is closely related to the broader perspective of acidity

and basicity which are quantified by the pK_a of the molecule. For bases, it is determined from the dissociation constant of the corresponding protonated species (conjugate acid). Thus, the pK_a value of a molecule plays a major role in determining its protonation state in a particular solvent.

Protonated forms of nitrogen-based bases, such as amines, have been widely used as pK_a determining agents for several complexes, including manganese and heme/copper complexes.[139,142,149] However, depending on the counteranion used and ion pairing in solution, the utilization of such acids can be difficult in low-polarity solvents because of solubility issues. Therefore, a need arises to fine-tune the ion pairing for use in wider applications with a non-nucleophilic and non-coordinating anion.

The counterion *tetrakis*(pentafluorophenyl)borate, $[B(C_6F_5)_4]^-$, is employed for the preparation of these protonated amines in order to increase their solubility in a range of organic solvents including the more polar acetonitrile and acetone but also lower polarity solvents such as dichloromethane (DCM), tetrahydrofuran (THF), *2*-methyltetrahydrofuran (MeTHF), diethyl ether (Et_2O), and even toluene. The protonated amines can thus be used as weak acids in titration experiments for pK_a measurements in low polarity solvents or in mechanistic studies for stepwise or coupled electron and proton transfer reactions (i.e., PT/ET, ET/PT, or PCET). A second advantage of this counterion is its low chemical reactivity, largely due to its very innocent, non-coordinating nature in both organic and inorganic reactions. This is an important characteristic for a counterion to have when working with metals and their chelates; any counterions that can coordinate to metals could change the structure and reactivity of such complexes.

The pK_a of the protonated amines described *vide infra* has previously been reported in water, acetonitrile (MeCN), and tetrahydrofuran (THF).[150-154] Previous examples of some protonated amines with a triflate counterion have been synthesized in absolute ethanol.[142] Also reported was the synthesis of the organic acid $[H(Et_2O)_2]B(C_5F_6)_4$ using hydrogen chloride in ether and the $Li[B(C_5F_6)_4]$ salt.[155]. Here, we describe the facile, one-step preparation of protonated nitrogen bases covering a pK_a range (in MeCN) from 12.3 to 18.46.

While rare, the ^{14}N-^{1}H coupling – seen here as the triplet splitting of N-H protons – is observed as the electric field about the ^{14}N nucleus becomes symmetrical and allows the spin-lattice relaxation time to increase.[156] Spin–spin coupling between ^{14}N and ^{1}H nuclei is observed in the ^{1}H-NMR spectra of all protonated amine $BArF_{20}$ salts in CD_2Cl_2, except for benzylammonium $BArF_{20}$ which displays a broad proton peak for the three exchangeable protons. Finally, trends between the decrease in pK_a of these ammoniums and increasing N-H proton chemical shifts, as well as increasing coupling constants, are observed through amine classes.

Results and Discussion

Synthesis and Characterization

We here describe the facile preparation of eight protonated amines with the *tetrakis*(pentafluorophenyl)borate [$B(C_6F_5)_4$] anion. The protonated amines can be separated into three major categories: ammoniums, pyridiniums, and anilinium. Within the ammoniums, we present tertiary and primary ammoniums (i.e., triethyl- and trimethyl- and benzylammonium), as well as a cyclic ammonium, 4-methylmorpholinium. The three pyridiniums presented *vide infra* include 2-methyl-, 2,6-dimethyl-, and 2,4,6-trimethylpyridinium. The final protonated amine used here is N,N-dimethylanilinium. All protonated amines were paired with the counteranion [$B(C_6F_5)_4$] ($BArF_{20}$), a bulky and very weakly-coordinating ion. The $BArF_{20}$ salts used were $LiBArF_{20}\cdot 2.35\ Et_2O$ and $KBArF_{20}$ for the acid-base and metathesis reactions, respectively (see S.I. for details).

NMR Spectroscopy

The protonation of all the amines in the present investigation are confirmed through ^{1}H NMR spectroscopy. The ^{1}H NMR spectra of the protonated amines displayed a triplet splitting of the N-H proton for all protonated nitrogen bases (or weak acids) (Fig. 2.1). The exception to this was benzylammonium $BArF_{20}$ ($BnNH_3^+$) which displayed a broad singlet likely due to the presence of three exchangeable N-H protons. As shown in Fig. 2.1, there

is a visible trend between N-H proton shifts and the pK_a of these protonated nitrogen bases (see also Table 2.3); weak acids in which the N-H bonds are sp^2 hybridized (i.e., pyridiniums) display proton deshielding as the pK_a decreases. A similar trend is seen for the protonated amines with sp^3 hybridized N-H bonds (i.e., ammoniums and anilinium).

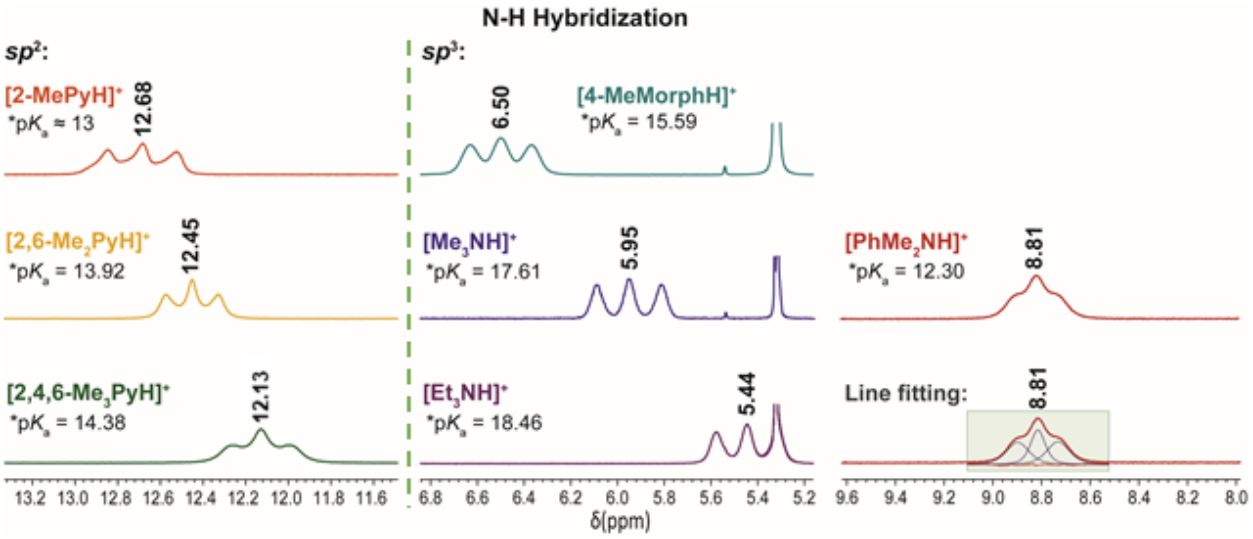

Figure 2.1. N-H proton shifts for protonated amines. Spectra on the left are for the N-H bonds in sp^2 hybridized orbitals where the spectra to the right are for those in sp^3 hybridized orbitals. Peak line fitting of the dimethylanilinium N-H triplet demonstrates broadening of the outer peaks while remaining equal in area to the center peak. *pK_a values reported in MeCN [150-154].

Due to the rapid relaxation of the ^{14}N nucleus, couplings between ^{14}N and ^{1}H atoms are infrequently observed in ^{1}H NMR; where a triplet splitting is expected, broad singlets are observed. The only example of a triplet splitting of the ^{14}N coupled proton in solution is reported for arginine residues, specifically the guanidinium protons, in collagen peptides; here, a 1:1:1 splitting was observed as well as a coupling constant ($^{1}J_{NH}$) of 52 Hz.[157] Two-dimensional solid-state NMR has also been used to observe the triplet splitting of the proton bonded to the nitrogen of *N*-acetyl-D,L-valine.[156] Other reports of triplet splittings in solution ^{1}H NMR were reported for long range couplings of ^{1}H and ^{14}N nuclei in either quaternary ammonium or bicyclic ammonium salts.[158,159]

Triplet signals for the ^{14}N-coupled acidic proton in the ^{1}H-NMR spectra of the acyclic and cyclic tertiary ammoniums (δ = 5.44 to 6.50 ppm) are very symmetrical with a 1:1:1

splitting pattern (i.e., $[Me_3NH]^+$ and $[Et_3NH]^+$, and [4-MeMorphH]$^+$). However, for $[PhMe_2NH]^+$ (δ = 8.81 ppm) the two outer peaks of the triplet appear to broaden with respect to the center peak. Integration of each peak of this triplet revealed that the 1:1:1 splitting is conserved. Coupling constants observed for triethylammonium ($^1J_{NH}$ = 52.9 Hz) , trimethylammonium ($^1J_{NH}$ = 53.5 Hz) and 4-methylmorpholinium ($^1J_{NH}$ = 53.2 Hz) are characteristic for ^{14}N-^1H couplings. Of note in the spectrum of 4-methylmorpholinium (Fig. 2.12) are the four unique proton signals corresponding to two axial and two equatorial protons in the ring; it can be inferred that a chair flip of these molecules is slower than the NMR time scale. As for dimethylanilinium, its triplet has a coupling constant of 42 Hz. Here, the slight decrease in coupling, despite an decrease in pK_a, could be attributed to the nitrogen electrons (for the conjugate base) delocalizing through the aromatic ring; the bond between a proton and the ^{14}N atom would thereby contain less *s*-character than the typical sp^3 bond. For the pyridiniums, their triplets also demonstrate a 1:1:1 splitting and appear symmetrical in peak intensity except in the case of $[2,4,6\text{-}Me_3PyH]^+$ in which the outer peaks broaden. The coupling constants found for these were 65.1 Hz, 61.3 Hz, and 53.6 Hz for [2-MePyH]$^+$, $[2,6\text{-}Me_2PyH]^+$, and $[2,4,6\text{-}Me_3PyH]^+$ respectively. A trend between proton coupling and pK_a was observed; as the pK_a of the pyridiniums ([2-MePyH]$^+$, $[2,6\text{-}Me_2PyH]^+$, and $[2,4,6\text{-}Me_3PyH]^+$) decreases, their coupling constants increase (53.6, 61.3, and 65.1 Hz, respectively). Also, in the case of ammoniums, there was no correlation with pK_a values; however, the general ^{14}N-^1H coupling constant is about 52-53 Hz.

We hypothesized that the three exchangeable protons on $[BnNH_3]^+$ were contributing to the broadening of the N-H peak. By adding a strong acid (4 equivalents), we were able to resolve the N-H triplet for $[BnNH_3]^+$, possibly due to the acid driving the protonation/deprotonation equilibrium towards protonation thereby favoring the fully protonated benzylammonium in solution (Figure 2.2). This acid was prepared via the salt-metathesis with the commercial benzylamine hydrochloride which was likely not fully protonated.

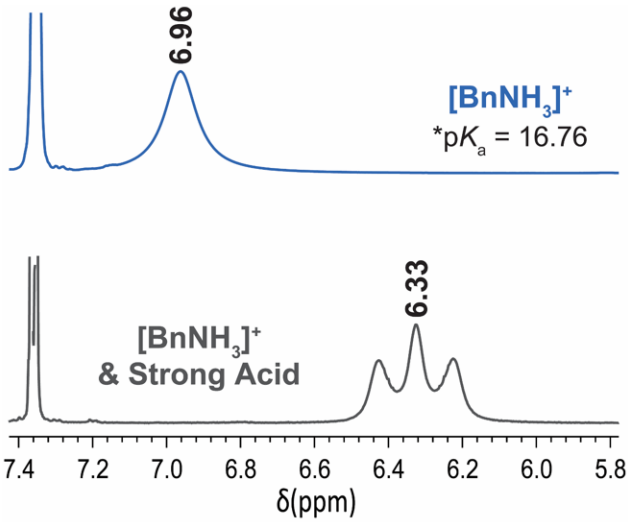

Figure 2.2. ^{1}H-NMR spectra of the N-H proton region of benzylammonium before and after addition of the strong organic acid $[H(OEt_2)_2]B(C_6F_5)_4$.

IR Spectroscopy

For solid-state characterization, infrared (IR) spectroscopy was used for all protonated amines. No clear trend between N-H stretches and pK_a was observed. For the protonated amine class, all N-H stretches were relatively sharp single peaks, these being at 3241, 3356, 3306 and 3238 cm^{-1} for $[Et_3NH]^+$, $[Me_3NH]^+$, $[BnNH_3]^+$, and [4-MeMorphH]$^+$ respectively. For $[PhMe_2NH]^+$, the N-H frequency is 3250 cm^{-1}. Within the pyridiniums, both [2-MePyH]$^+$ and $[2,4,6\text{-}Me_3PyH]^+$ contained N-H stretches with double shoulders (3358 and 3367 cm^{-1}, respectively) whereas $[2,6\text{-}Me_2PyH]^+$ was a sharp single peak (3356 cm^{-1}) (Table 2.1).

Table 2.1. IR spectroscopy stretching frequencies for the N-H bonds.

Protonated Nitrogen Base	N-H stretch (cm^{-1})	Protonated Nitrogen Base	N-H stretch (cm^{-1})
$[Et_3NH]^+$	3241	$[PhMe_2NH]^+$	3250
$[Me_3NH]^+$	3356	$[2,4,6\text{-}Me_3PyH]^+$	3367
$[BnNH_3]^+$	3306	$[2,6\text{-}Me_2PyH]^+$	3356
[4-MeMorphH]$^+$	3238	$[2\text{-MePyH}]^+$	3358

X-ray crystallography

Molecular structures of the acids described in the present study were determined by single-crystal X-ray diffraction (SC-XRD) studies. The crystals suitable for SC-XRD were grown from the concentrated solutions of the acids in diethyl ether at −30 °C inside the glove box. The data collection and refinement parameters are listed in Tables S2.1 and S2.2 while the selected bond distances and angles are mentioned in Tables 2.2 and 2.3. In all six structures, a hydrogen bonding interaction is present between the protonated amine and oxygen atom of diethyl ether ($Et_2O\cdots H{-}N^+_{acid}$) (Figures 2.3 and 2.4). The location of protons on the nitrogen atoms were found through difference Fourier mapping in the XRD structure and is further confirmed by proton NMR spectroscopy (*vide supra*).

The colorless crystals of $[Me_3NH]B(C_6F_5)_4$ were grown from their concentrated diethyl ether solution and the complex crystallizes in $P2_1/n$ space group where the crystallographic asymmetric unit contains a protonated trimethylammonium along with a diethyl ether molecule and anion $B(C_6F_5)_4$. The H-bonding interaction between the protonated amine and O-atom of diethyl ether is evident from a separation of 2.7741(17)

Å between N and O atoms. The average N-C bond distance increases from 1.448 Å in Me_3N to 1.490 Å in the protonated species.[160] Similarly, the C-N-C bond angle has also been found to slightly increase from 111.8° in trimethylamine to 112.3° in the trimethylammonium complex. Such structural changes further confirm the presence of a proton on the N-atom of amine and not on the O-atom of diethyl ether. Similar structural changes are also observed for other crystallized acids (Table 2.3).

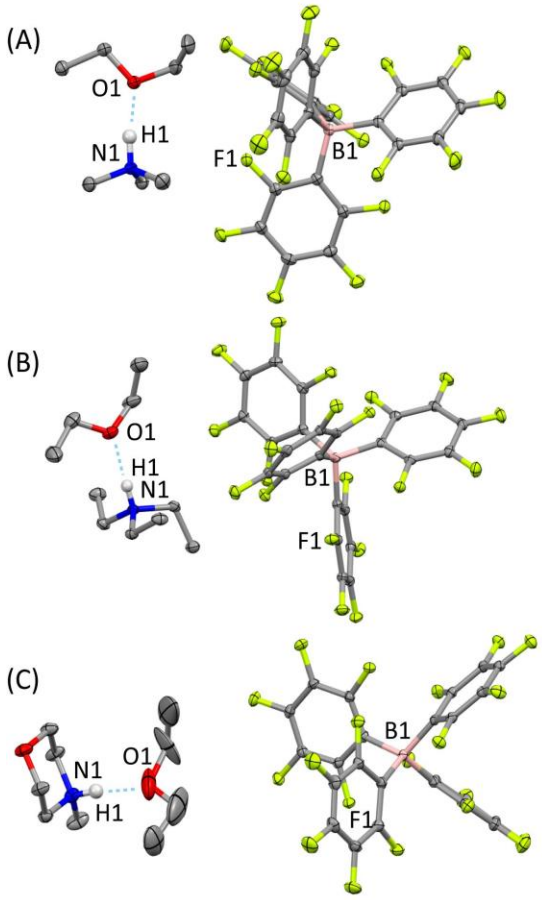

Figure 2.3. Perspective views of (A) $[Me_3NH]B(C_6F_5)_4.(C_2H_5)_2O$, (B) $[Et_3NH]B(C_6F_5)_4.(C_2H_5)_2O$, (C) $[4\text{-MeMorphH}]B(C_6F_5)_4.(C_2H_5)_2O$ showing 50% thermal contours for all non-hydrogen atoms (all of the hydrogens except for the N-proton have been omitted for clarity). Dotted line shows the H-bonding interaction between the protonated acid and diethyl ether.

The complex $[PhMe_2NH]B(C_6F_5)_4$ crystallizes in $P2_1/n$ space group and the crystallographic asymmetric unit contains a protonated N,N-dimethylanilinium along with a diethyl ether molecule disordered over two orientations and anion $B(C_6F_5)_4$. The

occupancy factor of the major component in diethyl ether disorder is 0.771. The average N-C bond distance was also found to increase compared to its amine analog; however, the C-N-C bond angle was found to decrease from 119.5° to 111.8° upon protonation. This was because the amine is extremely planar in nature but subsequent protonation changes the geometry around the N-atom and it becomes tetrahedral. The molecular structure of $[PhMe_2NH]B(C_6F_5)_4$ without any H-bonded diethyl ether has already been reported in a private communication and the changes in average N-C bond distance as well as in the C-N-C bond angle were similar to the H-bonded complex reported here.[161]

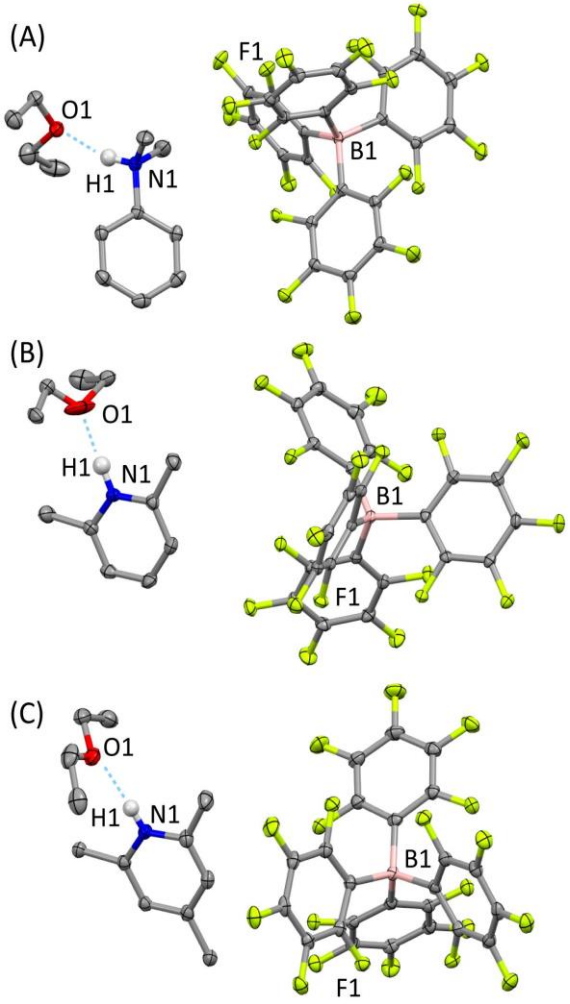

Figure 2.4. Perspective views of (A) $[PhMe_2NH]B(C_6F_5)_4.(C_2H_5)_2O$, (B) $[2,6\text{-}Me_2PyH]B(C_6F_5)_4.(C_2H_5)_2O$, and (C) $[2,4,6\text{-}Me_3PyH]B(C_6F_5)_4.(C_2H_5)_2O$, showing 50% thermal contours for all non-hydrogen atoms (all of the hydrogens except for the N-proton have been omitted for clarity). Dotted line shows the H-bonding interaction between the protonated acid and diethyl ether.

However, such structural changes, in terms of average N-C bond distance, upon protonation were not pronounced in pyridine-based weak acids. For example, the average N−C bond length slightly increases in 2,4,6-Me_3Py from 1.346 to 1.353 Å but it remains very much the same in case of 2,6-Me_2Py. But the C-N-C bond angle variation follows the same trend as in case of amine-based acids where the bond angles increase by about 5° in both [2,6-Me_2PyH]B(C_6F_5)$_4$ and [2,4,6-Me_3PyH]B(C_6F_5)$_4$. The H-bonded diethyl ether molecule in [2,6-Me_2PyH]B(C_6F_5)$_4$ is disordered over two orientations and the occupancy of the major fraction refines to be 0.595.

Table 2.2. Select bond distances and angles for the protonated amines and their corresponding neutral analogs.

	N-C (Å)		∠C-N-C (°)		Reference (amine)
	Amine	Protonated species	Amine	Protonated species	
$PhMe_2N$	1.441 1.426 1.390	1.500 1.497 1.479	119.5	114.0 110.8 110.6	[162]
2,6-Me_2Py	1.352 1.346	1.351 1.343	120.0	124.6	[163]
2,4,6-Me_3Py	1.348 1.343	1.353 1.352	118.1	123.6	[164]
4-MeMorph	1.471 1.467 1.460	1.505 1.490 1.489	110.9 109.8 107.9	112.2 111.8 109.2	[165]
Me_3N	1.448 1.448 1.448	1.494 1.488 1.487	110.7 110.7 110.7	111.3 111.0 110.4	[160]
Et_3N	1.471 1.475 1.481	1.508 1.507 1.057	111.8	113.2 113.1 110.6	[166]

A closer inspection of the symmetry in the X-ray structure hints towards a possible correlation with the N-H peak splitting in the ^{1}H NMR (*vide supra*). The N-H triplet seems

to be sharper for more symmetrical acids such as $[Me_3NH]^+$, $[Et_3NH]^+$ and [4-MeMorphH]$^+$ and for more asymmetrical ones for e.g., $[2,6\text{-}Me_2PyH]^+$ or $[2,4,6\text{-}Me_3PyH]^+$. This is also reflected in the ^{14}N-^1H coupling where for ammonium based protonated amines, the $^1J_{NH}$ values are very similar while they increase as the asymmetry increases in the molecules.

Table 2.3. Hydrogen bonding distances and angles between protonated amines and diethyl ether.

Protonated Amines	pK_a in MeCN	N···O (Å)	∠N–H···O (°)
$PhMe_2NH^+$	12.3	2.782/2.744	165.8/177.7
$2,6\text{-}Me_2PyH^+$	13.92	2.816/2.668	169.5/170.5
$2,4,6\text{-}Me_3PyH^+$	14.38	2.805	173.6
4-MeMorphH$^+$	15.59	2.716	169.7
Me_3NH^+	17.61	2.774	165.5
Et_3NH^+	18.46	2.801	177.9

Conclusion

A series of protonated amines with the very weakly coordinating anion $[B(C_6F_5)_4]$ were prepared by metathesis or acid-base chemistry. These were characterized using ^1H- and ^{19}F-NMR as well as IR spectroscopies and were further analyzed with single crystal X-ray diffraction. These can be used in either titration experiments for pK_a determination or mechanistic studies in low-polarity solvents. A fascinating feature seen in seven ^1H NMR spectra was the triplet splitting of the ^{14}N coupled acidic protons. The combination of slowed quadrupolar relaxation of the ^{14}N nuclei and proton exchange rate enable the visualization of the spin-spin coupling between ^{14}N and ^1H nuclei in solution.

Perhaps of greatest importance is the ability to differentiate between acids based on the hybridization about the nitrogen atom through N-H chemical shifts and their coupling constants ($^1J_{NH}$). This has the potential to be a valuable reference for molecules containing multiple nitrogen sites that could be protonated, as well as with varying hybridizations, such as in biological samples where the nitrogen moieties are buried within protein structures and experience slow proton exchange rates. For N-H chemical shifts,

as the acidity of either the ammoniums or pyridiniums increased, the proton shift became more and more deshielded. Coupling constants ($^1J_{NH}$) for ammoniums (either cyclic or acyclic) were found to be ≈53 Hz, except $[PhMe_2NH]^+$ ($^1J_{NH}$ = 42 Hz), whereas those for pyridiniums were found to be in the range of 53.6 to 65.1 Hz.

The protonated amines have been structurally characterized; each displays a hydrogen bonding interaction between the nitrogen of protonated amine and oxygen atom of a diethyl ether molecule. Considerable structural and geometrical changes are observed upon protonation which is best reflected by the increase in the average C-N bond distance and angle. Such structural changes are more pronounced in the case of alkylamines than in the more geometrically rigid pyridine-based molecules. Moreover, the shape of N-H triplet peaks for ^{14}N-^1H coupling constant ($^1J_{NH}$) in the proton NMR of the molecules seems to be symmetry dependent and are comparatively sharper for molecules with higher symmetry such as in protonated alkylamines.

Supporting Information

Materials and Instruments

All chemicals and solvents were of commercially available grade and used as received unless otherwise mentioned. Acetonitrile (MeCN) was purchased from Sigma-Aldrich and Diethyl ether was purchased from Fisher Scientific. The solvents were further purified by passing through an 18 cm or 60 cm-long column of activated alumina under argon using an Innovative Technologies or Inert PureSolv Micro solvent purification system. The solvents were further deoxygenated by bubbling them with argon for an hour prior to sending to the glovebox. These solvents were then stored in dark glass bottles inside the glovebox over 3 or 5 Å molecular sieves for more than 72 hours prior to use. The protonated amines were synthesized and handled under an inert atmosphere using either argon and standard Schlenk line techniques or a Vacuum Atmospheres OMNI-Lab inert atmosphere (<0.5 ppm of O_2 and H_2O) glovebox filled with nitrogen.

Benzylammonium chloride (99%), and 2,4,6-collidine (99%) were purchased from Alfa Aesar. Trimethylamine hydrochloride (>98%), triethylamine hydrochloride (>98%), 2-methyl pyridine (98%), 2,6-lutidine (≥99%), N,N-dimethylaniline (≥99.5%),and 4-methylmorpholine(≥99.5%) were purchased from Sigma Aldrich. Hydrogen chloride in diethyl ether (2 M) was purchased from Acros Organics. $K[B(C_6F_5)_4]$ and $Li[B(C_6F_5)_4](2.35\ Et_2O)$ (99.9%) were purchased from Boulder Scientific Company. Dichloromethane-d_2 (99.8%) was purchased in 1 g ampules from Cambridge Isotope Laboratories.

^{1}H-NMR and ^{19}F-NMR spectra were recorded either on a JEOL 400 or 500 MHz instrument. The residual ^{1}H resonances of the solvents were used as a reference. Infrared (IR) spectra were obtained using a Thermo Scientific Nicolet iS5 Fourier Transform IR (FT-IR) spectrometer equipped with an iD7 attenuated total reflection (ATR) accessory. Single-crystal X-ray data were collected using a Gemini R (Agilent Technologies) diffractometer at the X-ray diffraction facility of the Joint School of Nanoscience and Nanoengineering (JSNN). The temperature of the data collection was controlled using the system Cryojet (manufactured by Oxford Instruments).

Synthesis and Characterization

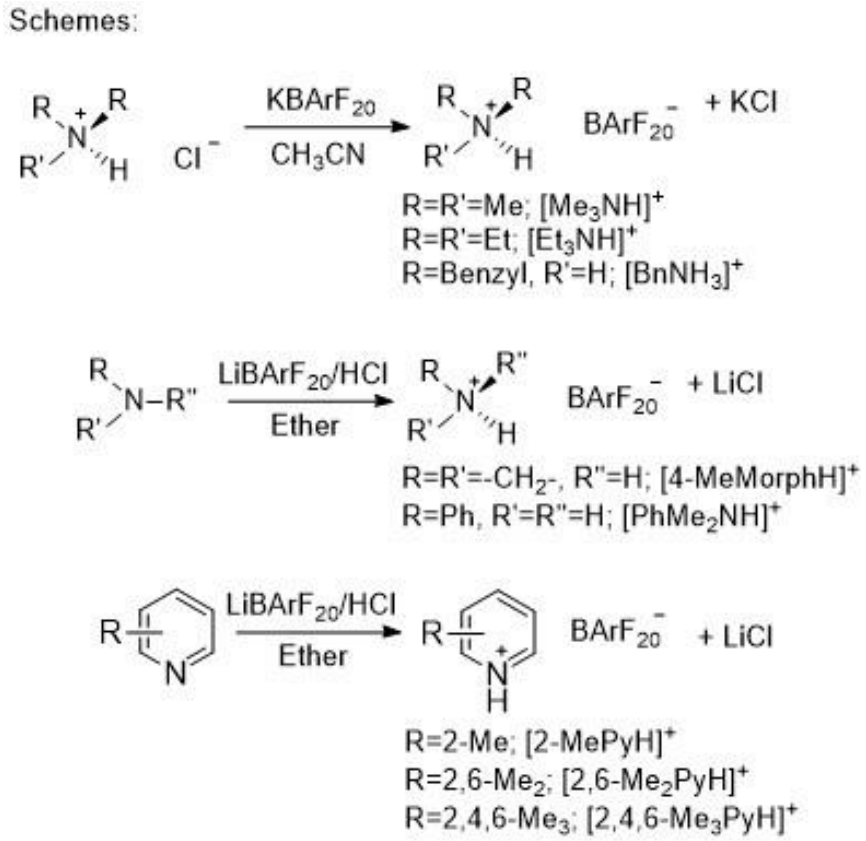

Scheme 2.1. General preparation of protonated nitrogen bases.

Preparation of the $BArF_{20}$ acids from the amine hydrochloride salts was performed by a general procedure (Scheme 2.1); details are given for trimethylammonium $BArF_{20}$ as a representative case.

$[Me_3NH]B(C_6F_5)_4$

The trimethylamine hydrochloride salt was dried under vacuum before transferring into the glovebox. Into a 50 mL Schlenk flask was added a solution of $KBArF_{20}$ (487 mg, 676 mmol) in MeCN (12 mL). Then, a solution of the trimethylamine hydrochloride (64.7 mg, 676 mmol) in MeCN (11 mL) was added into the Schlenk flask. Upon combination of the two solutions, a fine, white precipitate was seen. The mixture was stirred for 30 minutes

before filtration to remove the KCl. The resultant solution was then evaporated under reduced pressure and the white solid was redissolved in the minimum amount of Et_2O. The solution was kept in the freezer at -30°C. After 3 days, colorless crystals were observed suitable for X-ray structural determination. 87% Yield (410 mg, 0.5 Et_2O per acid molecule). FT-IR (solid) [cm^{-1}]: $\nu_{(N-H)}$= 3357 (Figure 2.22). ^{1}H-NMR (DCM-d_2): δ 6.80 (t, $^1J_{NH}$ = 53.5 Hz, 1H); 3.03 (d, 9H) (Figure 2.7). ^{19}F-NMR (DCM-d_2): δ -133.21; -163.22; -167.27 (Figure 2.8).

$[Et_3NH]B(C_6F_5)_4$

Colorless crystals were collected from cold Et_2O, 346 mg (65%, 0.8 Et_2O per acid molecule). FT-IR (solid) [cm^{-1}]: $\nu_{(N-H)}$= 3241 (Figure 2.23). ^{1}H-NMR (DCM-d_2): δ 5.44 (t, $^1J_{NH}$ = 52.9 Hz, 1H); 3.26 (dq, 6H); 1.38 (t, 9H) (Figure 2.5). ^{19}F-NMR (DCM-d_2): δ -133.14; -163.29; -167.31 (Figure 2.6).

$[BnNH_3]B(C_6F_5)_4$

White powder was collected, 427 mg (67%, 2 Et_2O per acid molecule and MeCN). FT-IR (solid) [cm^{-1}]: $\nu_{(N-H)}$= 3307 (Figure 2.24). ^{1}H-NMR (DCM-d_2): δ 6.96 (br s, 3H); 7.49 (d, 3H); 7.35 (m, 2H); 4.20 (s, 2H) (Figure 2.9). ^{19}F-NMR (DCM-d_2): δ -133.22; -163.21; -167.23 (Figure 2.10).

Preparation of the $BArF_{20}$ acids from the conjugate base was performed by a general procedure; details are given for 2,4,6-trimethylpyridinium $BArF_{20}$ as a representative case.

$[2,4,6\text{-}Me_3PyH]B(C_6F_5)_4$

In the glovebox, a solution of $LiBArF_{20}$ (573 mg, 625 mmol, 1 eq.) in Et_2O (6 mL) was made in a Schlenk flask. This was transferred out of the glovebox to inject in 2,4,6-collidine (83 µL, 625 mmol, 1 eq.). Then, the solution was cooled down with a cold bath (Dry ice, MeCN, -30°C). After cooling the solution, hydrogen chloride in ether (2 M, 2 mL, 6 eq.) was injected into the Schlenk flask. Upon swirling the solution, a white precipitate began to form. The solution was kept at -30°C for 30 minutes and swirled every 5 minutes.

The solution was brought up to room temperature before the solvent was evaporated. In the glovebox, the white solid was redissolved in Et_2O before being filtered. The solution was then placed in the freezer at -30°C. After a few days, colorless crystals were observed suitable for X-ray structural determination. Yield (396 mg, 74%, 0.75 Et_2O per acid molecule). FT-IR (solid) [cm^{-1}]: $\nu_{(N-H)}$= 3367 (Figure 2.26). ^{1}H-NMR (DCM-d_2): δ 12.13 (t, $^1J_{NH}$ = 53.6 Hz, 1H); 7.40 (s, 2H); 2.71 (s, 6H); 2.58 (s, 3H) (Figure 2.14). ^{19}F-NMR (DCM-d_2): δ -133.08; -163.45; -167.39 (Figure 2.15).

[2,6-Me_2PyH]B(C_6F_5)$_4$

White powder was collected, 398 mg (78%, 0.5 Et_2O per acid molecule). FT-IR (solid) [cm^{-1}]: $\nu_{(N-H)}$= 3308 (Figure 2.27). ^{1}H-NMR (DCM-d_2): δ 12.45 (t, $^1J_{NH}$ = 61.3 Hz, 1H); 8.33 (t, 1H); 7.65 (d, 2H); 2.81 (s, 6H) (Figure 2.16). ^{19}F-NMR (DCM-d_2): δ -133.08; -163.41; -167.37 (Figure 2.17).

[2-MePyH]B(C_6F_5)$_4$

White powder was collected, 438 mg (83%, 0.5 Et_2O per acid molecule). FT-IR (solid) [cm^{-1}]: $\nu_{(N-H)}$= 3358 (Figure 2.28). ^{1}H-NMR (DCM-d_2): δ 12.68 (t, $^1J_{NH}$ = 65.1 Hz, 1H); 8.53 (td, 1H); 8.46 (t, 1H); 7.92 (m, 2H); 2.87 (s,3H) (Figure 2.18). ^{19}F-NMR (DCM-d_2): δ -133.12; -163.33; -167.30 (Figure 2.19).

[4-MeMorphH]B(C_6F_5)$_4$

Colorless crystals were collected, 358 mg (70%, 0.3 Et_2O per acid molecule). FT-IR (solid) [cm^{-1}]: $\nu_{(N-H)}$= 3239 (Figure 2.25). ^{1}H-NMR (DCM-d_2): δ 6.50 (t, $^1J_{NH}$ = 53.2 Hz, 1H); 4.20 (dd, J = 13.9, 3.6 Hz, 2H_d); 3.73 (ddd, J = 13.9, 11.6, 2.7 Hz, 2H_c); 3.49 (m, 2H_b); 3.22 (dddd, J = 12.5, 11.6, 3.6, 2.5 Hz, 2H_a); 3.03 (d, 3H) (Figure 2.12). ^{19}F-NMR (DCM-d_2): δ -133.21; -163.05; -167.13 (Figure 2.13).

[PhMe$_2$NH]B(C_6F_5)$_4$

Colorless crystals were collected, 331 mg (62%, 0.7 Et_2O per acid molecule). FT-IR (solid) [cm^{-1}]: $\nu_{(N-H)}$= 3251 (Figure 2.29). ^{1}H-NMR (DCM-d_2): δ 8.81 (t, $^1J_{NH}$ = 42.0 Hz, 1H); 7.64

(m, 3H); 7.41 (m, 2H); 3.35 (s, 6H) (Figure 2.20). ^{19}F-NMR (DCM-d_2): δ -133.14; -163.26; -167.27 (Figure 2.21).

Crystallographic Studies

Suitable X-ray quality single crystals were grown in the glovebox from concentrated solutions in diethyl ether kept at −30 °C. All reflection intensities were measured at 100(2) K using a Gemini R diffractometer (equipped with Atlas detector) with CuKα radiation (λ = 1.54178 Å) under the program CrysAlisPro (Version CrysAlisPro 1.171.38.43f, Rigaku OD, 2015). The same program (but a different version viz. CrysAlisPro 1.171.40.53, Rigaku OD, 2019) was used to refine the cell dimensions and for data reduction. The structure was solved with the program SHELXT-2018/2 and was refined on F2 by full-matrix least-squares technique using the SHELXL-2018/3 program package. Analytical absorption correction based on gaussian integration was applied using a multifaceted crystal model by CrysAlisPro. Non-hydrogen atoms were refined anisotropically. In the refinement, hydrogen atoms, except those involved in H-bonding, were treated as riding atoms using SHELXL default parameters while those involved in H-bonding were located with electron difference map. For [MeN-morpH]B$(C_6F_5)_4$.$(C_2H_5)_2O$, the crystal lattice also contains disordered diethyl ether molecule, for which its contributions has been taken out using the program SQUEEZE for the final refinement. All details of the SQUEEZE refinement are mentioned in the final CIF file.

NMR Spectroscopy

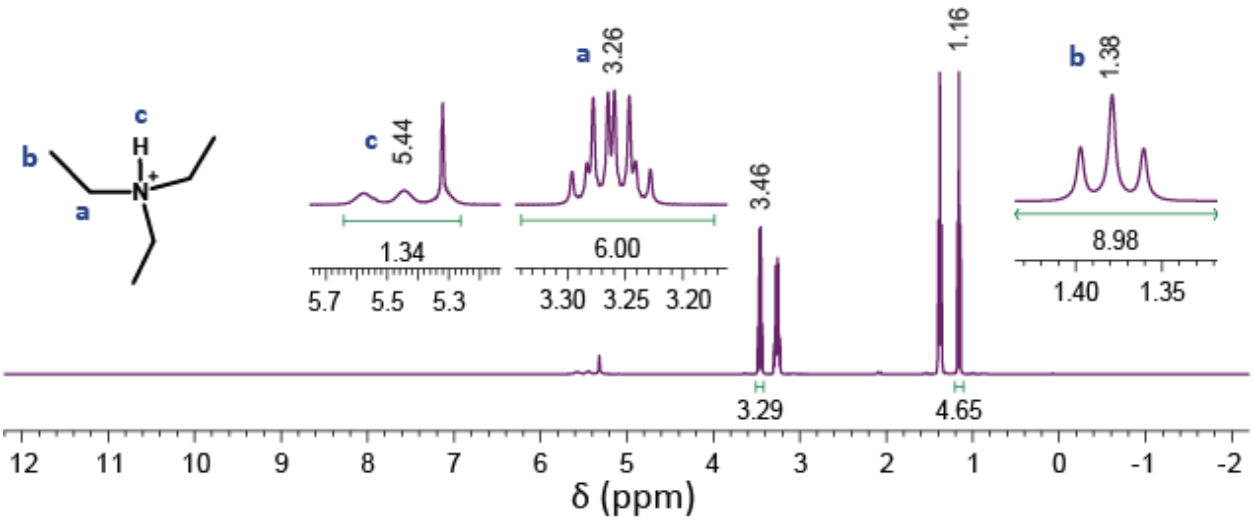

Figure 2.5. ^{1}H-NMR spectrum of $[Et_3NH]B(C_6F_5)_4$ in CD_2Cl_2 at room temperature.

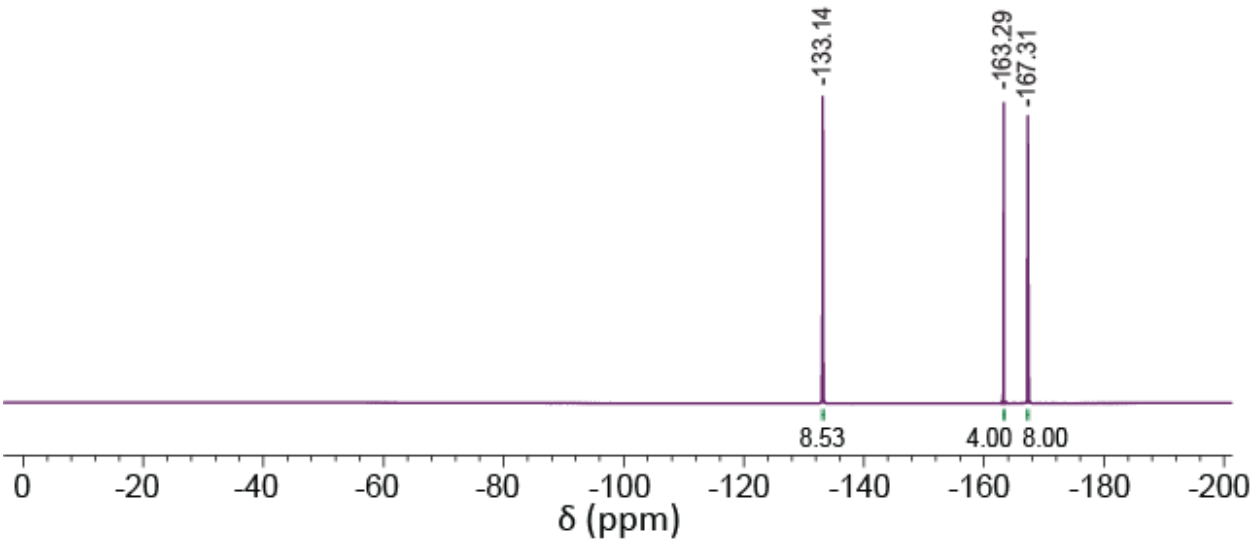

Figure 2.6. ^{19}F-NMR spectrum of $[Et_3NH]B(C_6F_5)_4$ in CD_2Cl_2 at room temperature

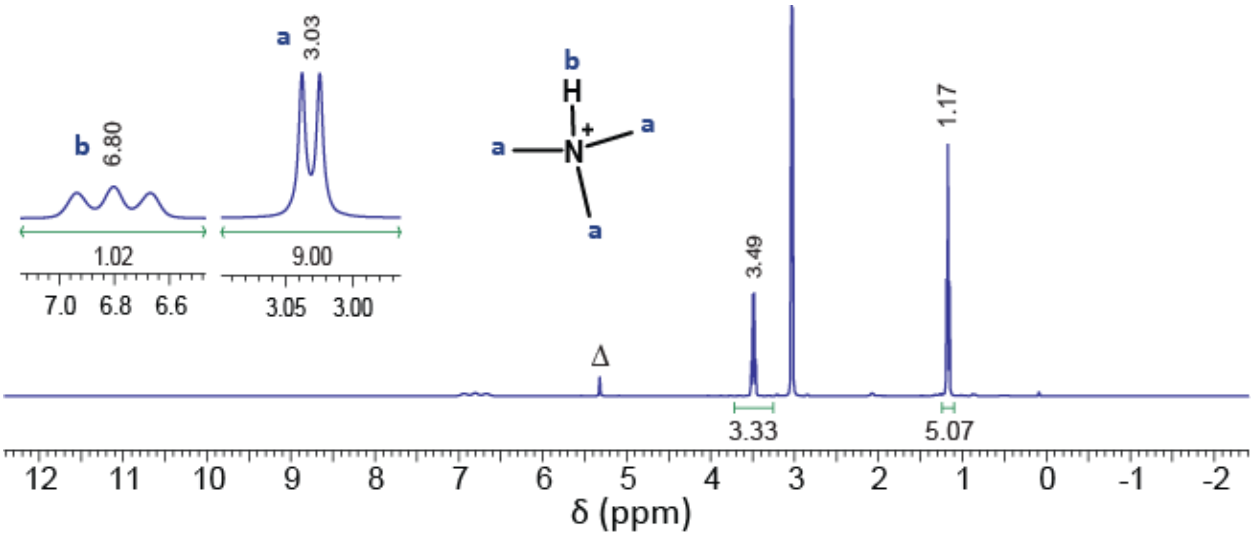

Figure 2.7. ^{1}H-NMR spectrum of $[Me_3NH]B(C_6F_5)_4$ in CD_2Cl_2 at room temperature.

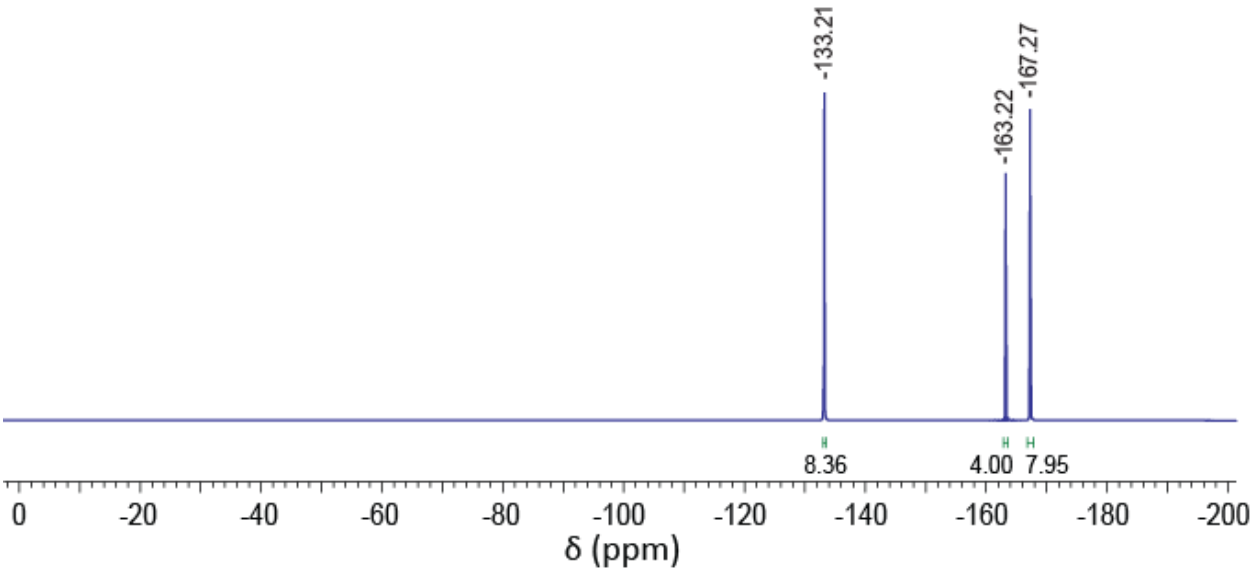

Figure 2.8. ^{19}F-NMR spectrum of $[Me_3NH]B(C_6F_5)_4$ in CD_2Cl_2 at room temperature.

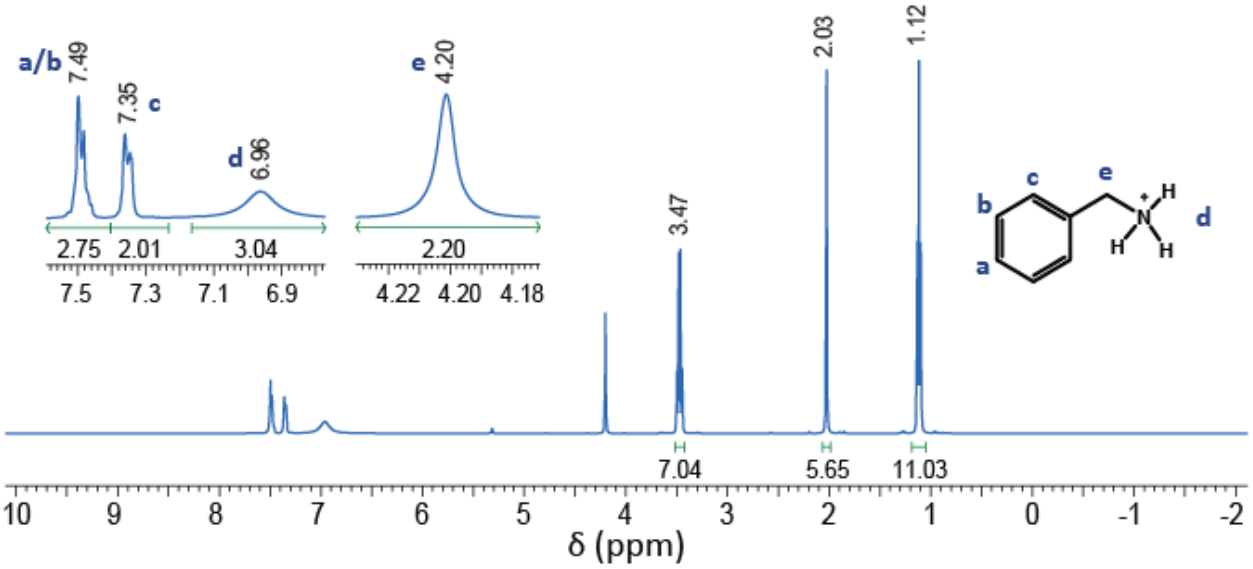

Figure 2.9. ^{1}H-NMR spectrum of $[BnNH_3]B(C_6F_5)_4$ in CD_2Cl_2 at room temperature.

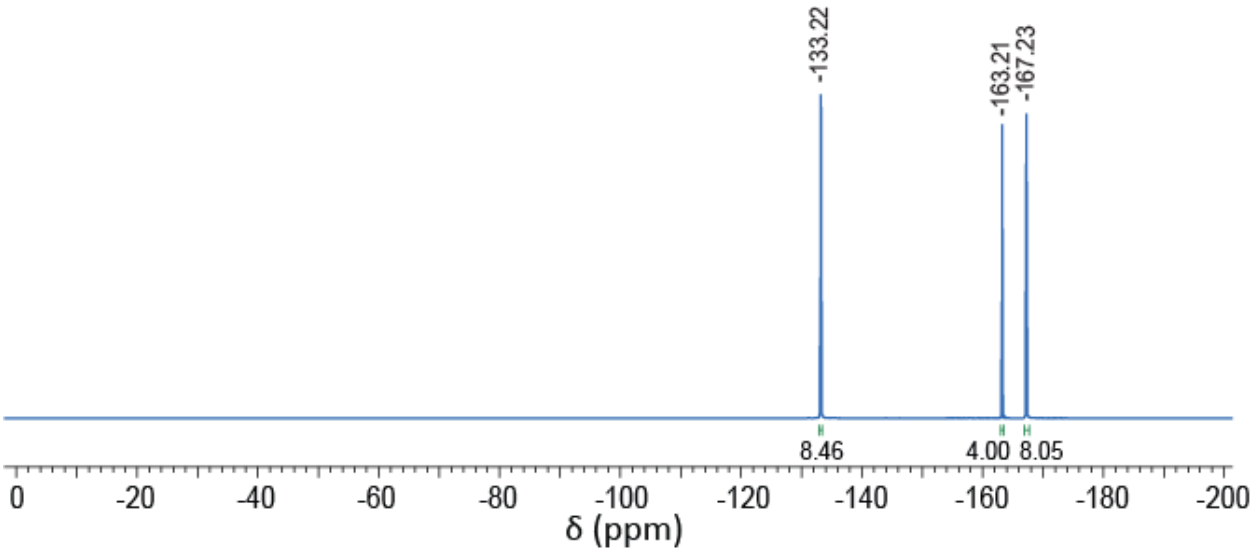

Figure 2.10. ^{19}F-NMR spectrum of $[BnNH_3]B(C_6F_5)_4$ in CD_2Cl_2 at room temperature.

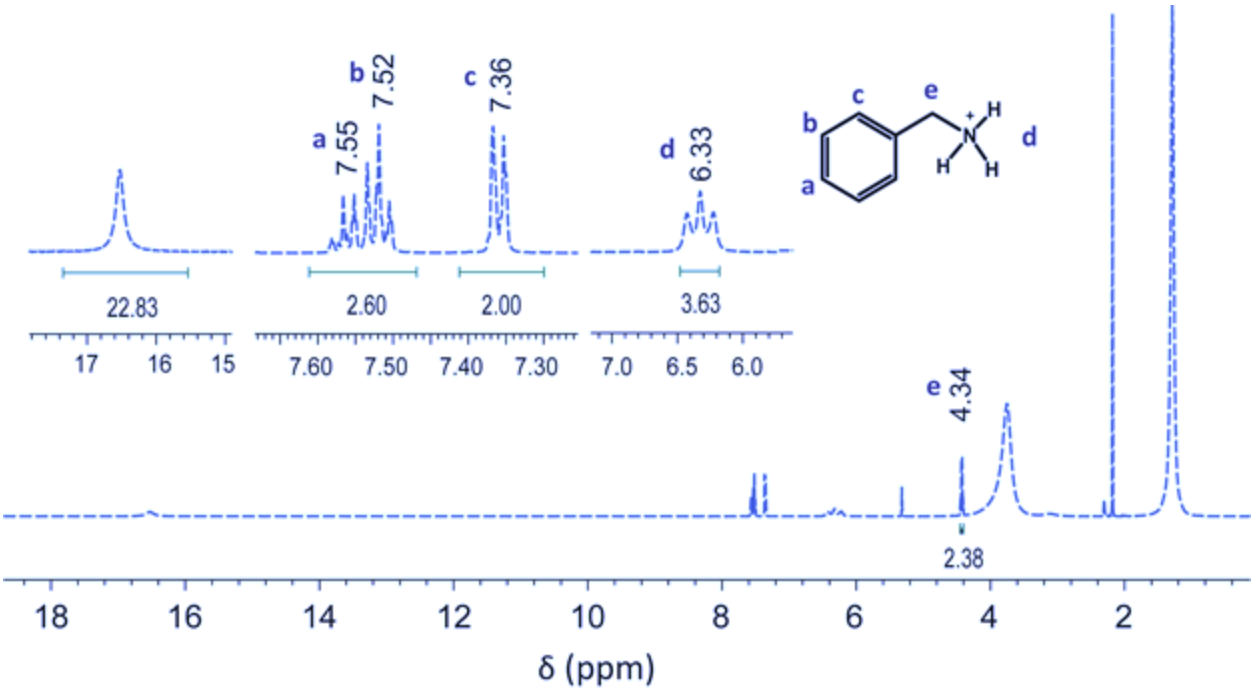

Figure 2.11. ^{1}H-NMR spectrum of $[BnNH_3]B(C_6F_5)_4$ with 4 equivalents of $[H(OEt_2)_2]B(C_6F_5)_4$ in CD_2Cl_2 at room temperature.

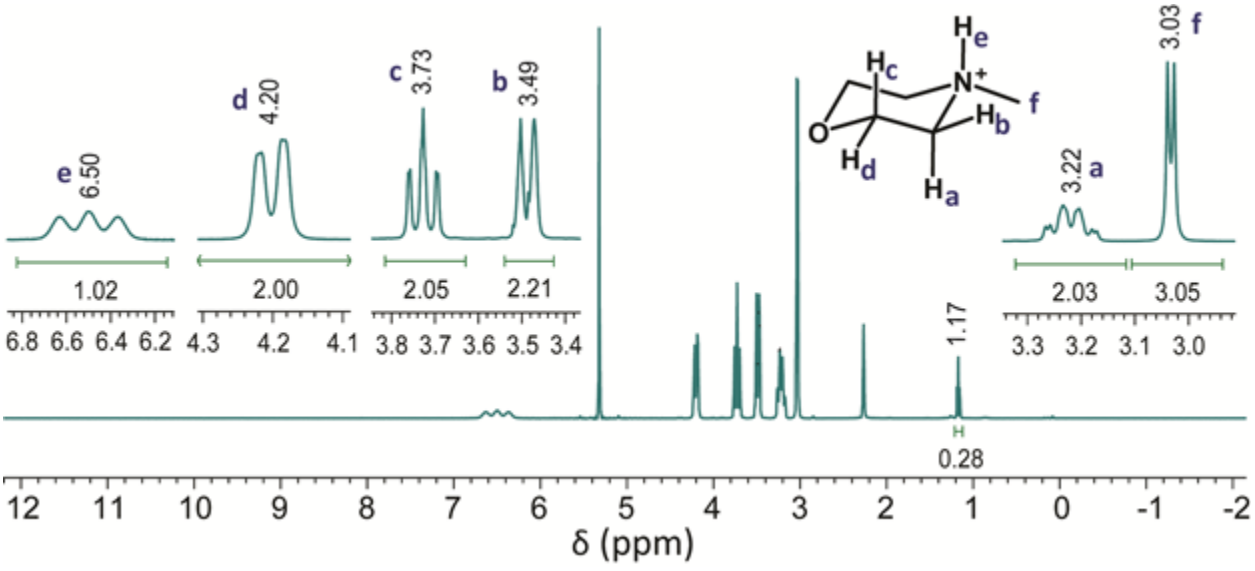

Figure 2.12. ^{1}H-NMR spectrum of $[4\text{-MeMorphH}]B(C_6F_5)_4$ in CD_2Cl_2 at room temperature.

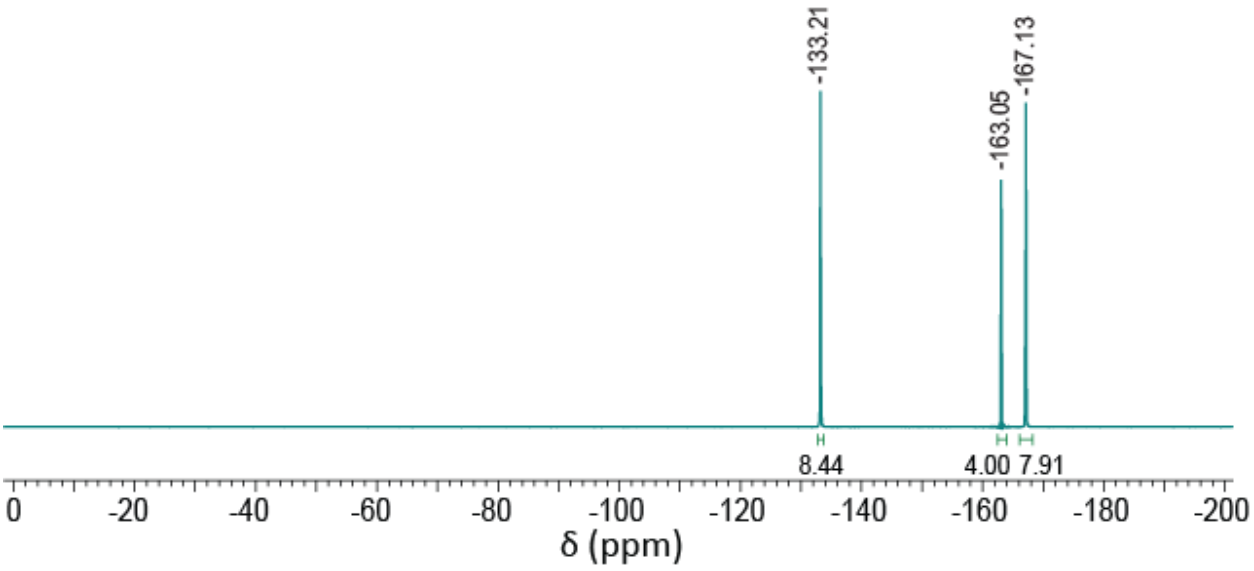

Figure 2.13. ^{19}F-NMR spectrum of [4-MeMorphH]B(C_6F_5)$_4$ in CD_2Cl_2 at room temperature.

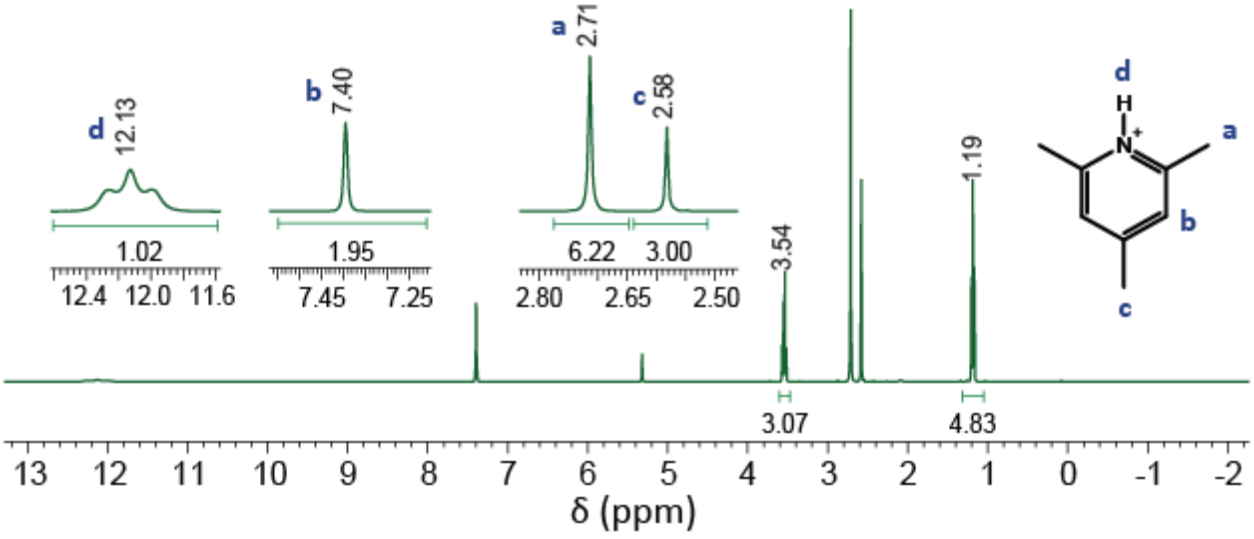

Figure 2.14. ^{1}H-NMR spectrum of [2,4,6-Me_3PyH]B(C_6F_5)$_4$ in CD_2Cl_2 at room temperature.

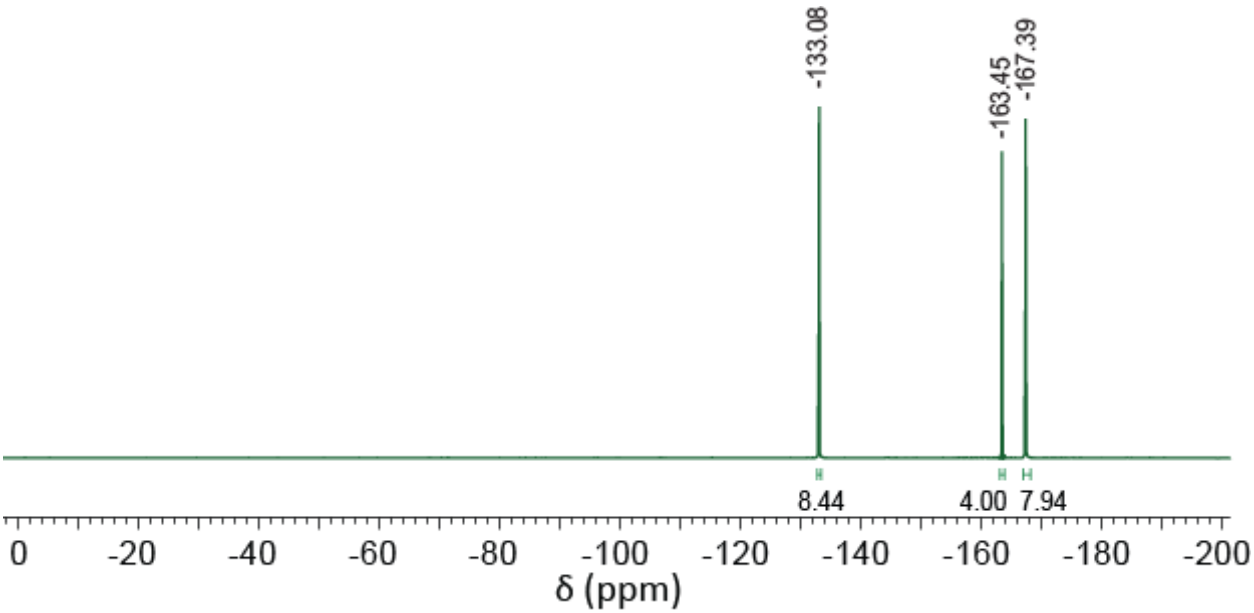

Figure 2.15. ^{19}F-NMR spectrum of [2,4,6-Me$_3$PyH]B(C$_6$F$_5$)$_4$ in CD$_2$Cl$_2$ at room temperature.

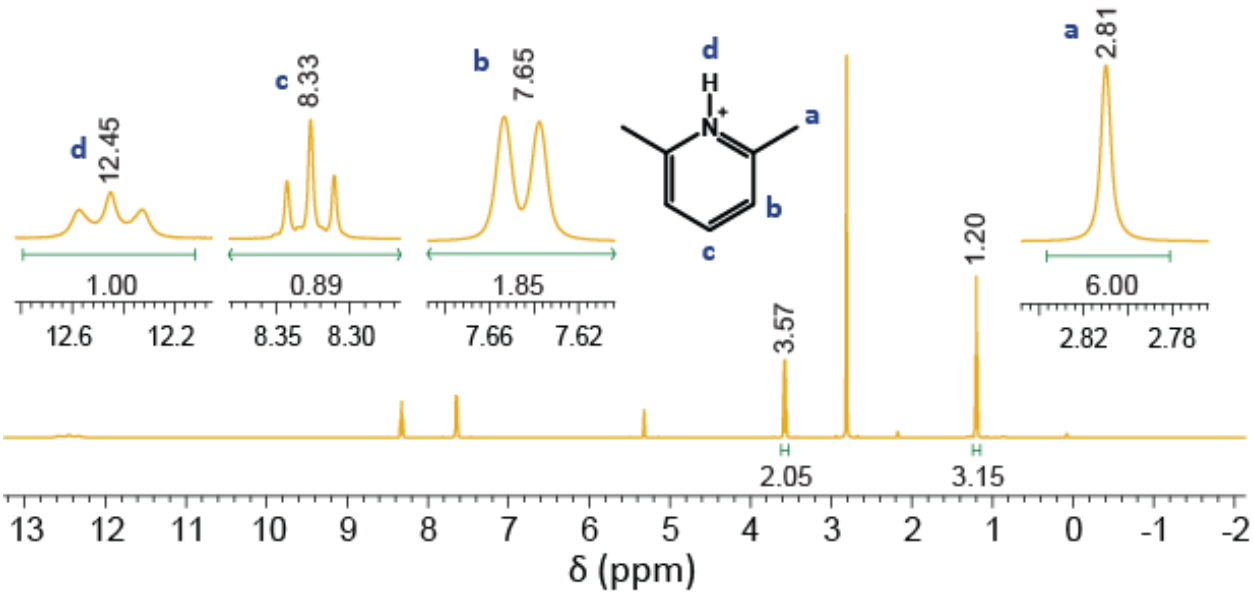

Figure 2.16. ^{1}H-NMR spectrum of [2,6-Me$_2$PyH]B(C$_6$F$_5$)$_4$ in CD$_2$Cl$_2$ at room temperature.

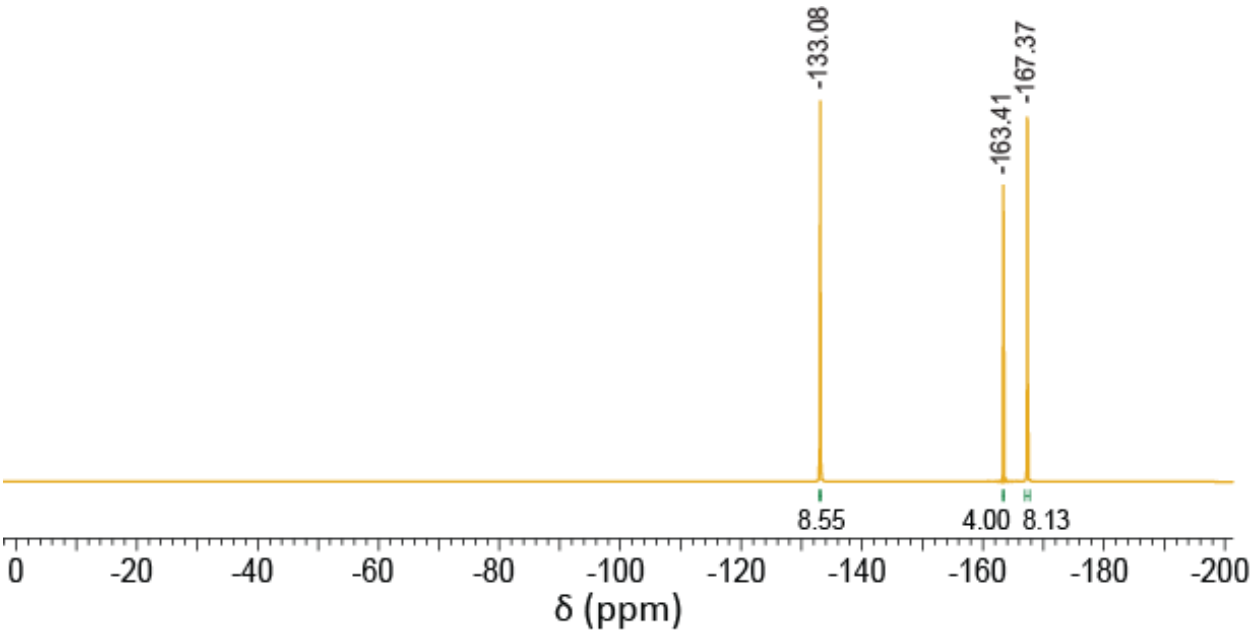

Figure 2.17. ^{19}F-NMR spectrum of [2,6-Me$_2$PyH]B(C$_6$F$_5$)$_4$ in CD$_2$Cl$_2$ at room temperature.

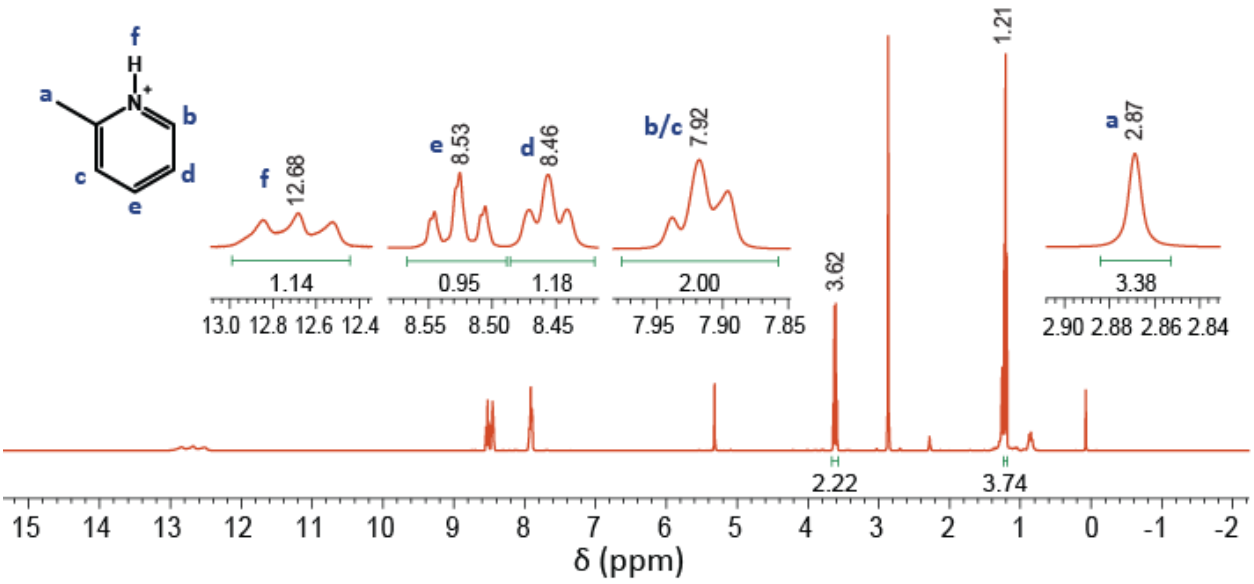

Figure 2.18. ^{1}H-NMR spectrum of [2-MePyH]B(C$_6$F$_5$)$_4$ in CD$_2$Cl$_2$ at room temperature.

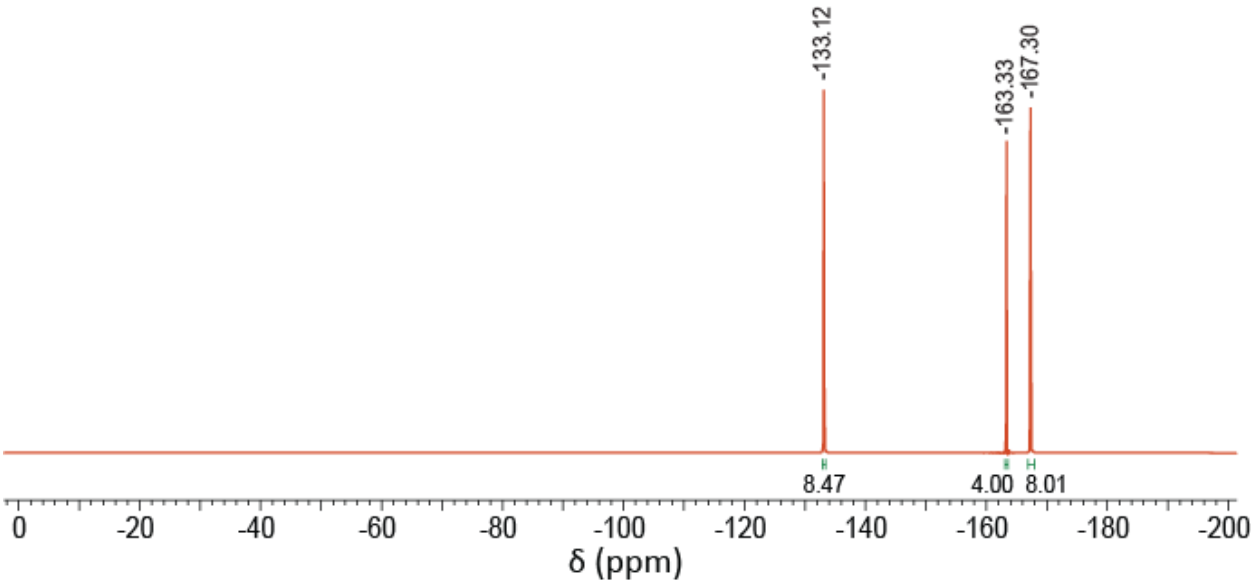

Figure 2.19. ^{19}F-NMR spectrum of [2-MePyH]B(C_6F_5)$_4$ in CD_2Cl_2 at room temperature.

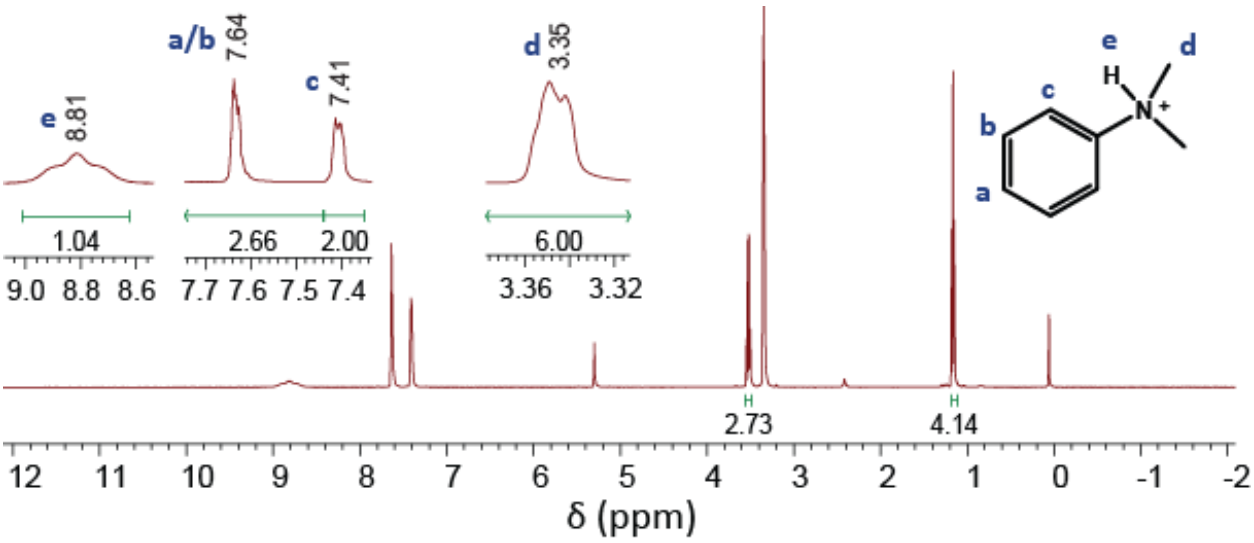

Figure 2.20. ^{1}H-NMR spectrum of [PhMe$_2$NH]B(C_6F_5)$_4$ in CD_2Cl_2 at room temperature.

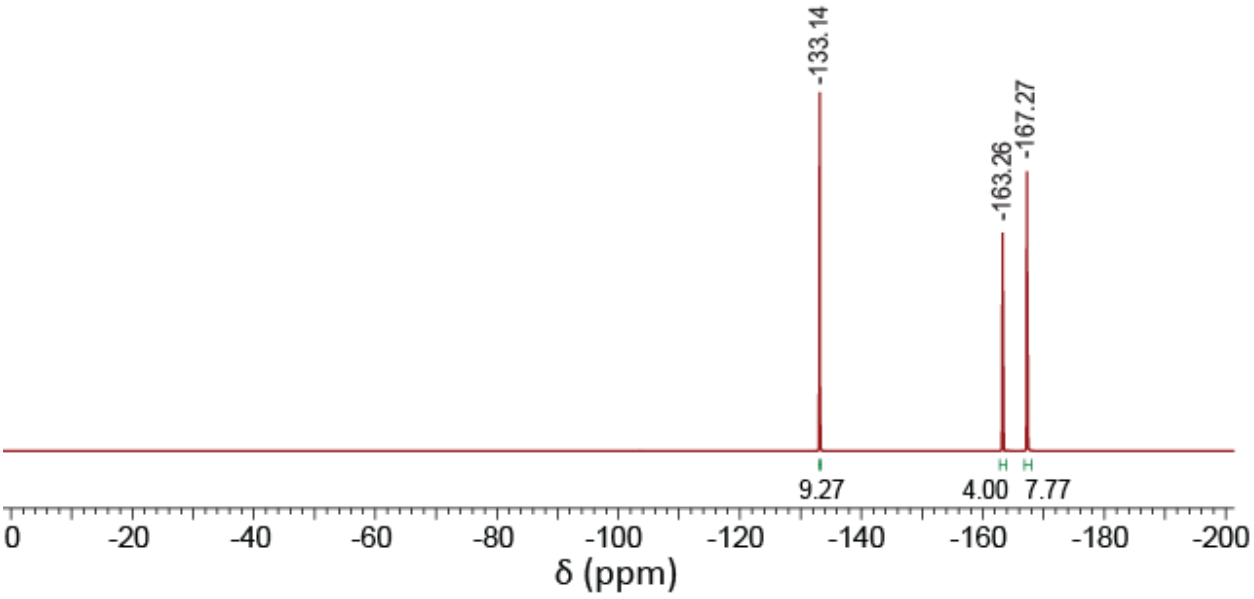

Figure 2.21. ^{19}F-NMR spectrum of [PhMe$_2$NH]B(C$_6$F$_5$)$_4$ in CD$_2$Cl$_2$ at room temperature.

Table 2.4. Coupling constants ($^1J_{NH}$) of the ^{14}N-^{1}H triplets for protonated amines.

Protonated amine	$^1J_{NH}$ (left-center peaks, Hz)	$^1J_{NH}$ (center-right peaks, Hz)
N,N-Dimethylanilinium	41.96	41.96
2-Methylpyridinium	65.40	64.72
2,6-Dimethylpyridinium	61.29	61.29
2,4,6-Trimethylpyridinium	53.55	53.55
N-methylmorpholinium	53.31	53.00
Benzylammonium	---	---
Trimethylaminium	53.59	53.44
Triethylaminium	52.86	52.85

FT-IR Spectroscopy

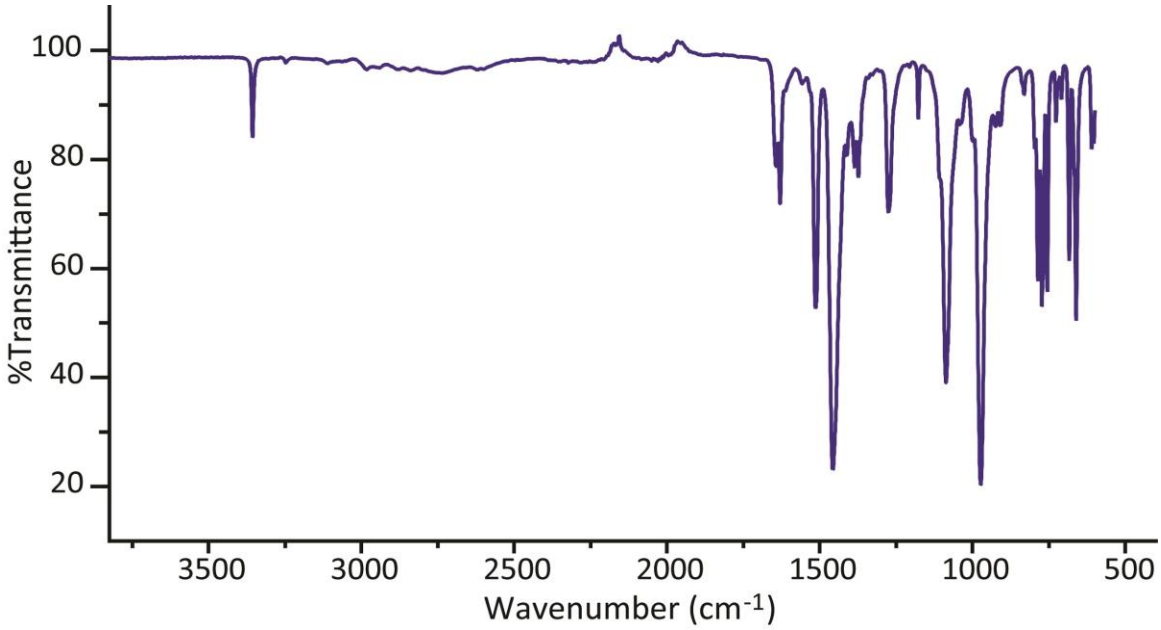

Figure 2.22. FT-IR spectrum of $[Me_3NH]B(C_6F_5)_4$.

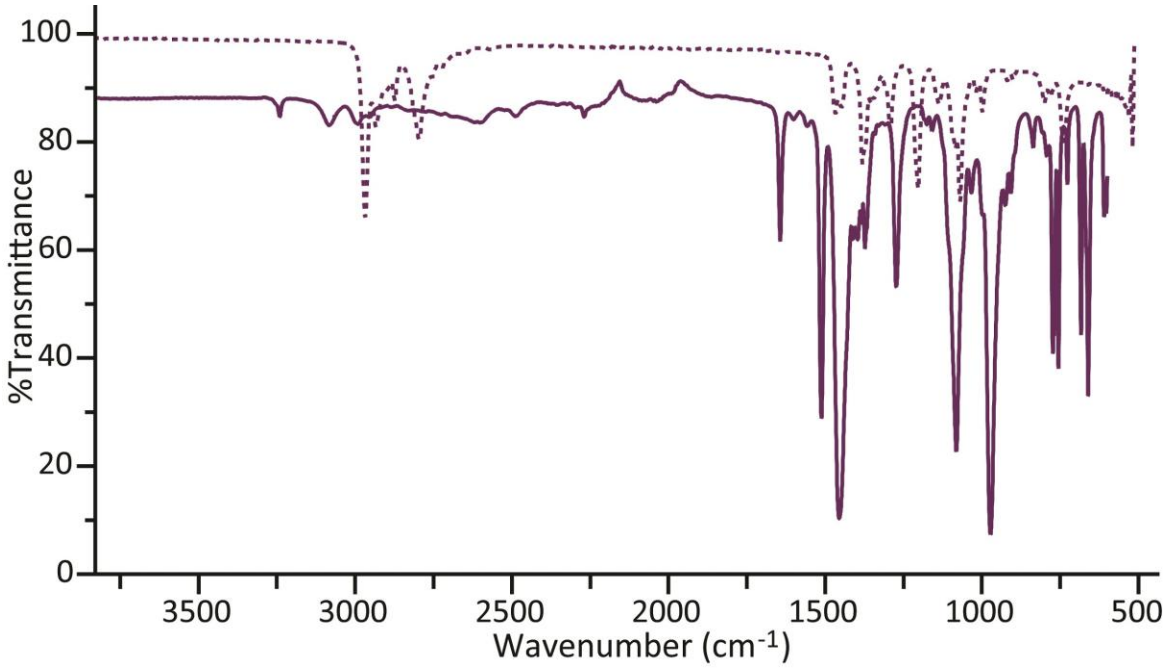

Figure 2.23. FT-IR spectral comparison of Et_3N (dotted line) and $[Et_3NH]B(C_6F_5)_4$ (solid line).

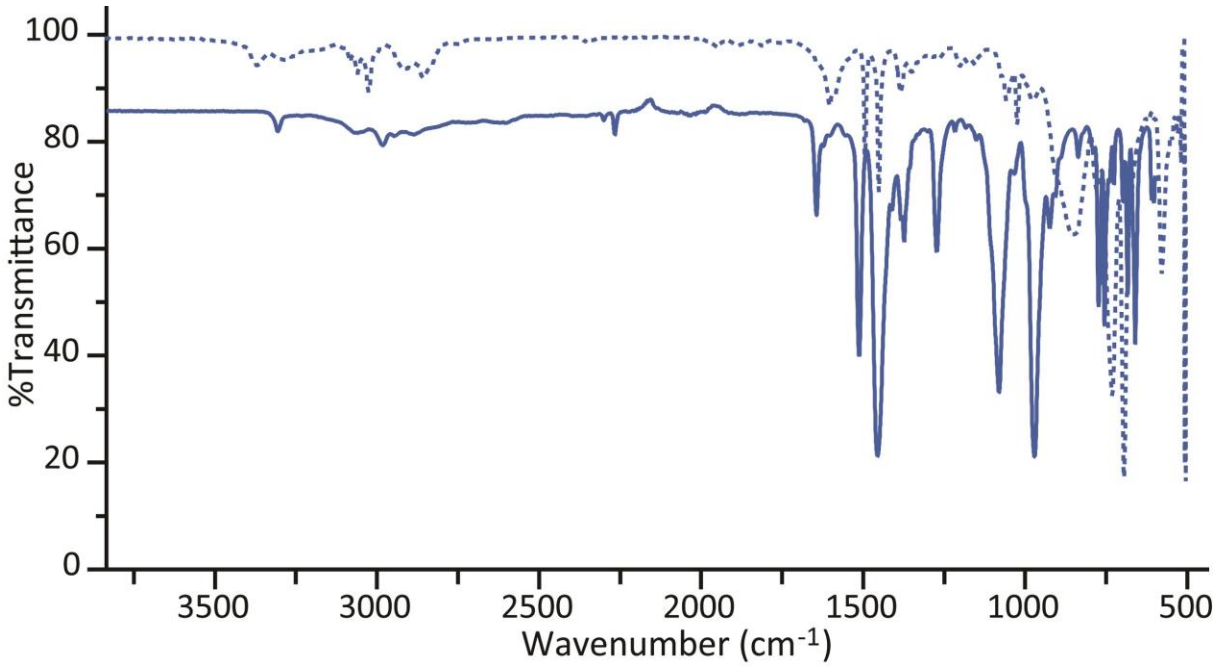

Figure 2.24. FT-IR spectral comparison of $BnNH_2$ (dotted line) and $[BnNH_3]B(C_6F_5)_4$ (solid line).

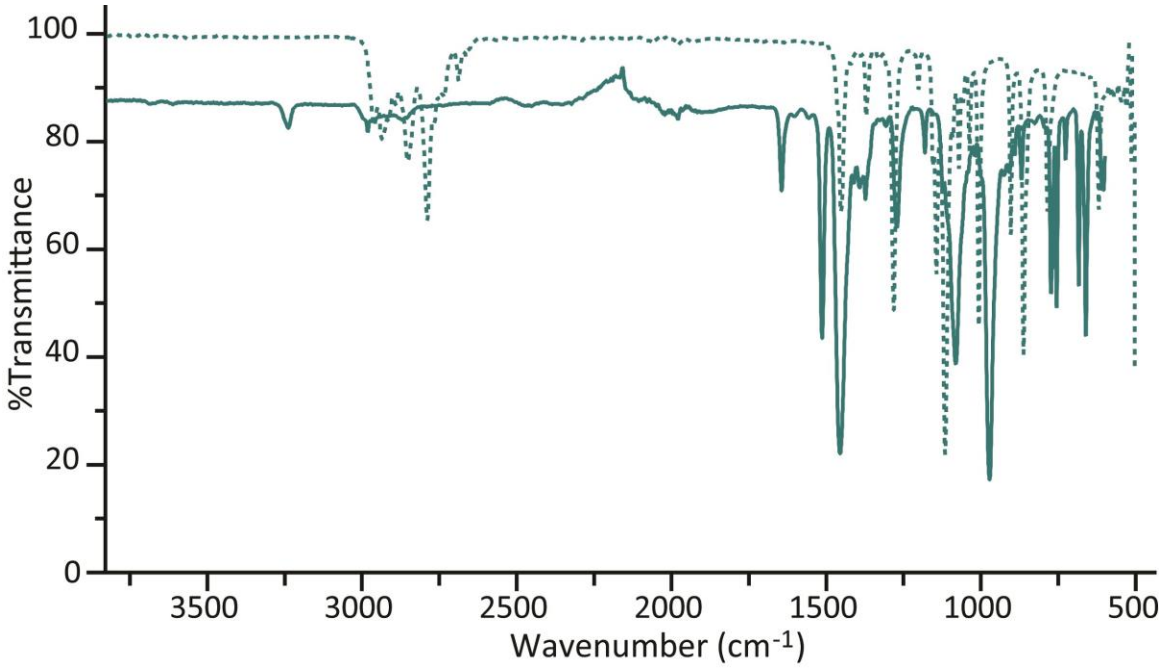

Figure 2.25. FT-IR spectral comparison of 4-MeMorph (dotted line) and [4-MeMorphH]$B(C_6F_5)_4$ (solid line).

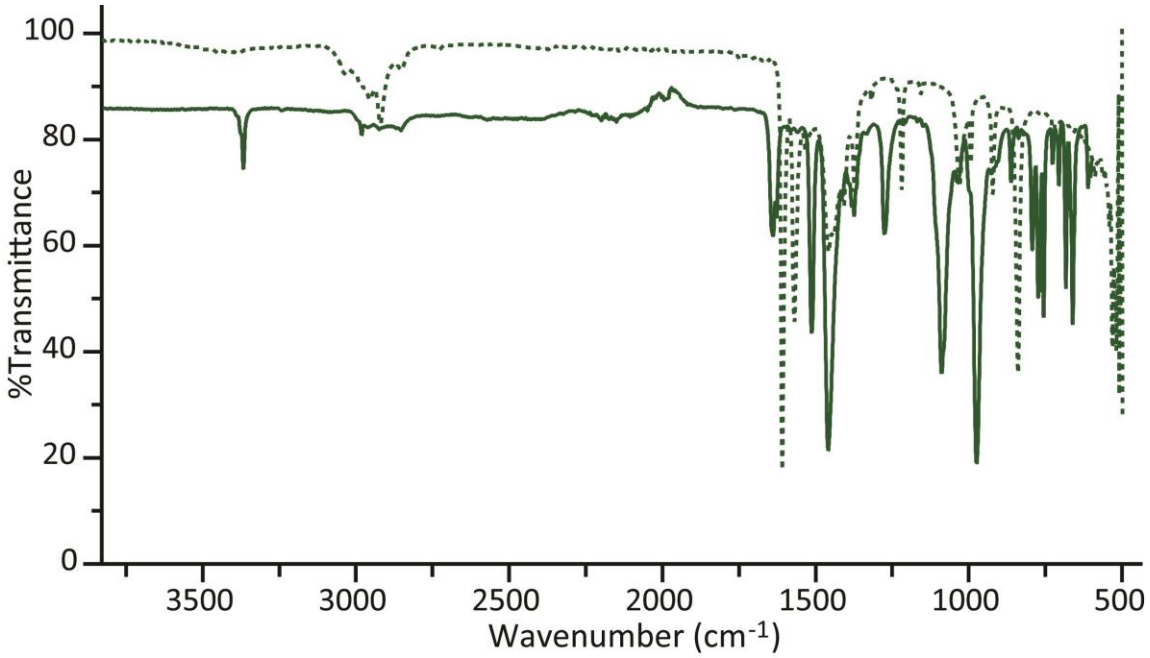

Figure 2.26. FT-IR spectral comparison of 2,4,6-Me_3Py (dotted line) and [2,4,6-Me_3PyH]$B(C_6F_5)_4$ (solid line).

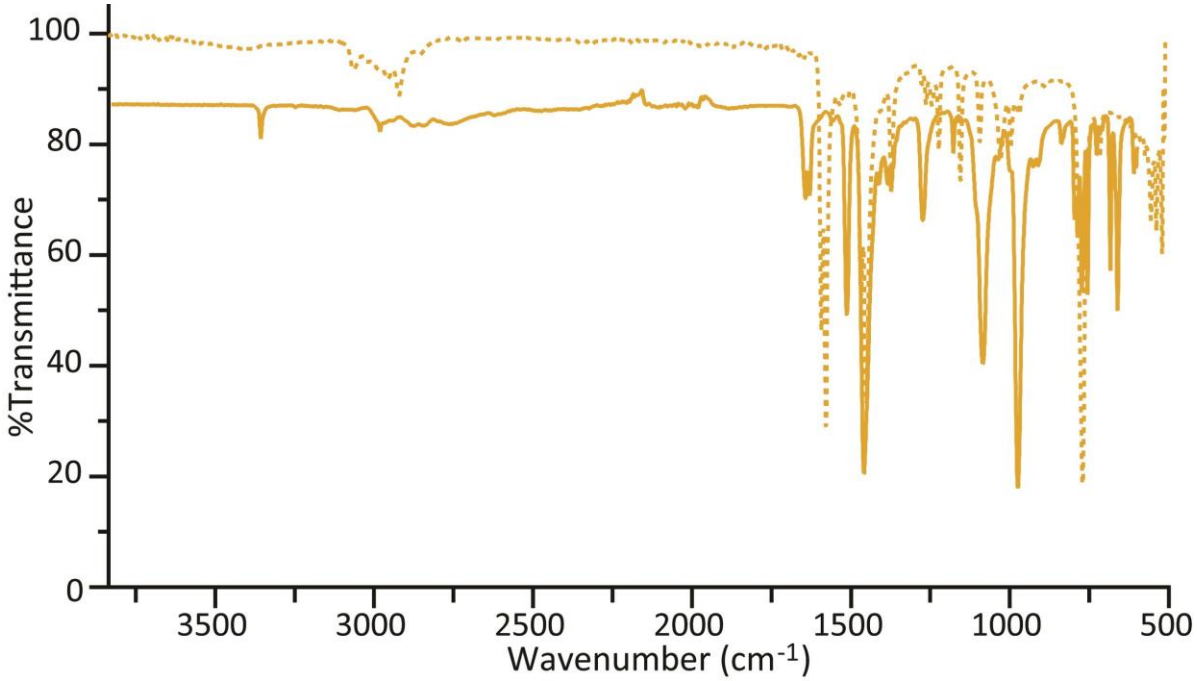

Figure 2.27. FT-IR spectral comparison of 2,6-Me_2Py (dotted line) and [2,6-Me_2PyH]$B(C_6F_5)_4$ (solid line).

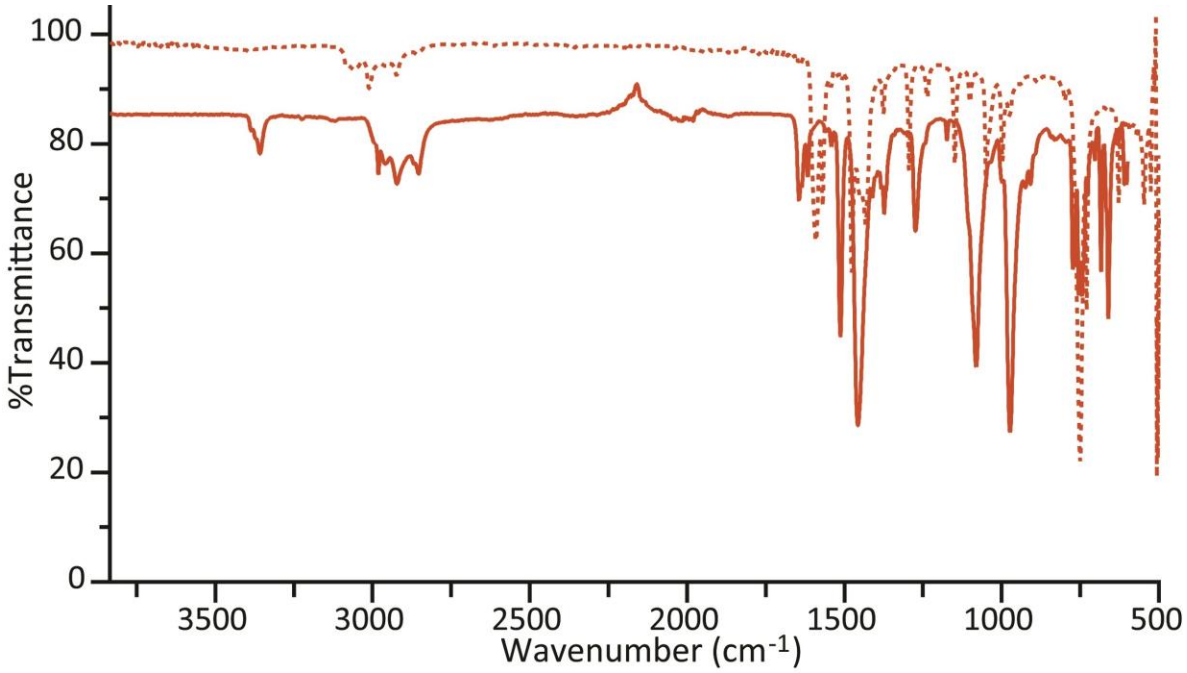

Figure 2.28. FT-IR spectral comparison of 2-MePy (dotted line) and [2-MePyH]B(C_6F_5)$_4$ (solid line).

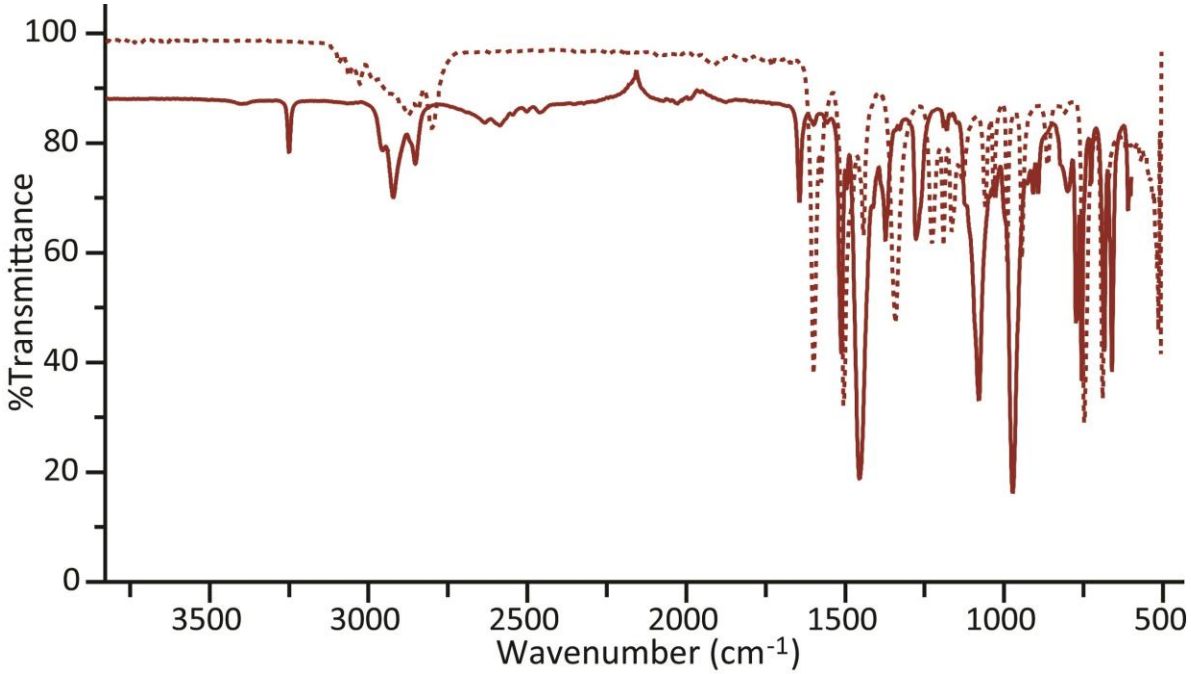

Figure 2.29. FT-IR spectral comparison of $PhMe_2NH$ (dotted line) and [$PhMe_2NH$]B(C_6F_5)$_4$ (solid line).

Single-crystal X-ray Crystallography

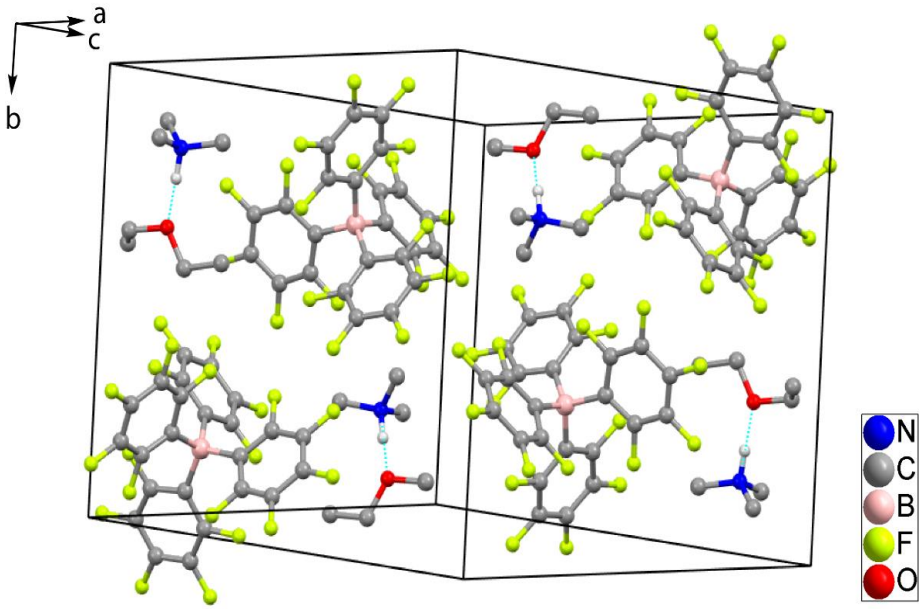

Figure 2.30. Diagram illustrating the molecular packing of $[Me_3NH]B(C_6F_5)_4.(C_2H_5)_2O$ at 100 K (all of the hydrogens except for the N-proton have been omitted for clarity).

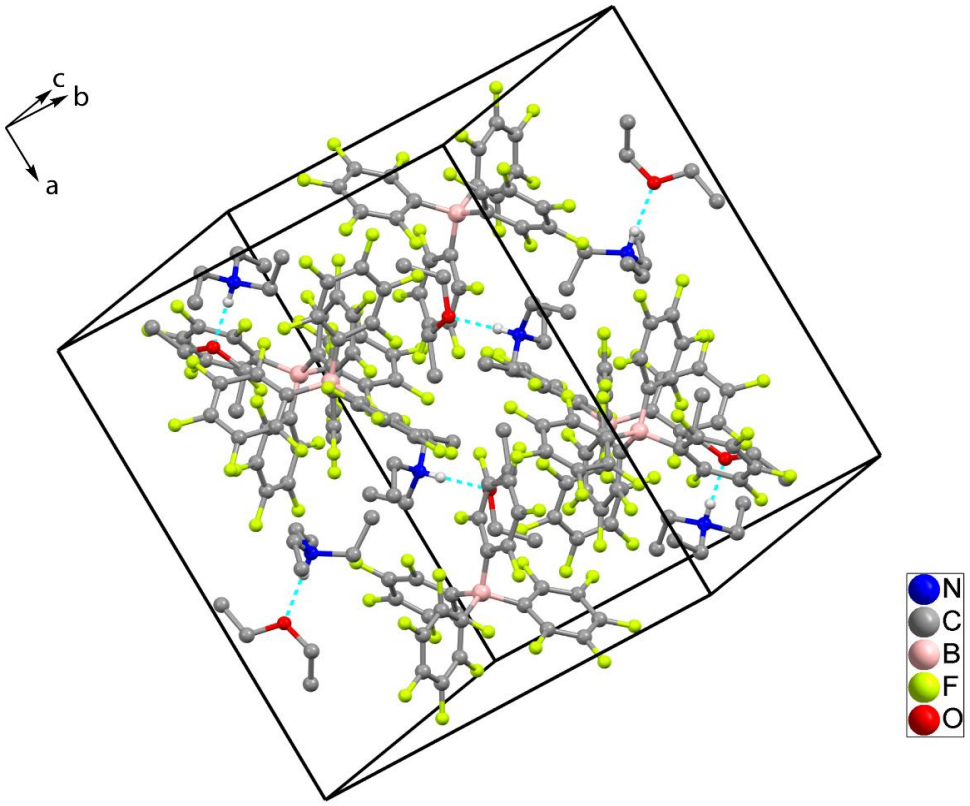

Figure 2.31. Diagram illustrating the molecular packing of $[Et_3NH]B(C_6F_5)_4.(C_2H_5)_2O$ at 100 K (all of the hydrogens except for the N-proton have been omitted for clarity).

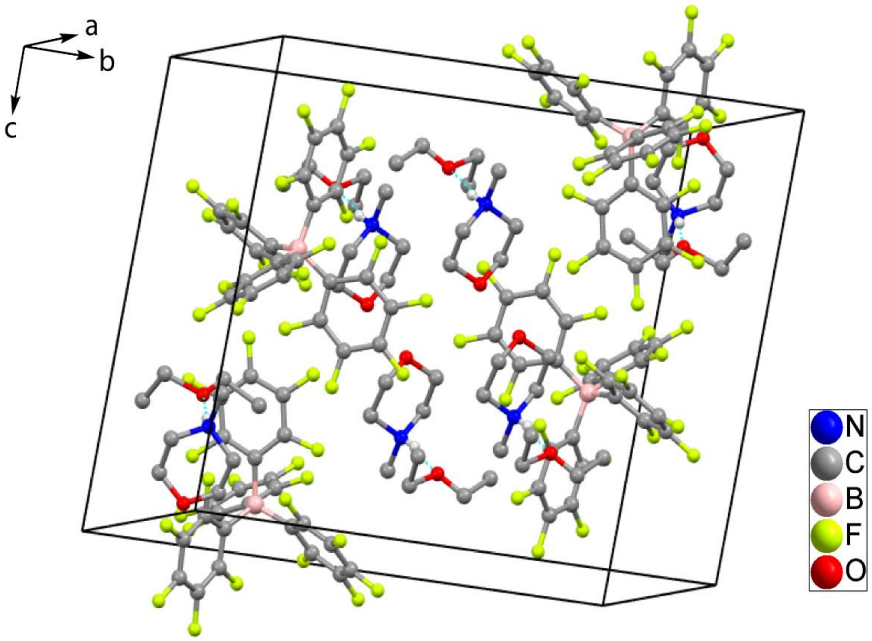

Figure 2.32. Diagram illustrating the molecular packing of [4-MeMorpH]B(C_6F_5)$_4$.(C_2H_5)$_2$O at 100 K (all of the hydrogens except for the N-proton have been omitted for clarity).

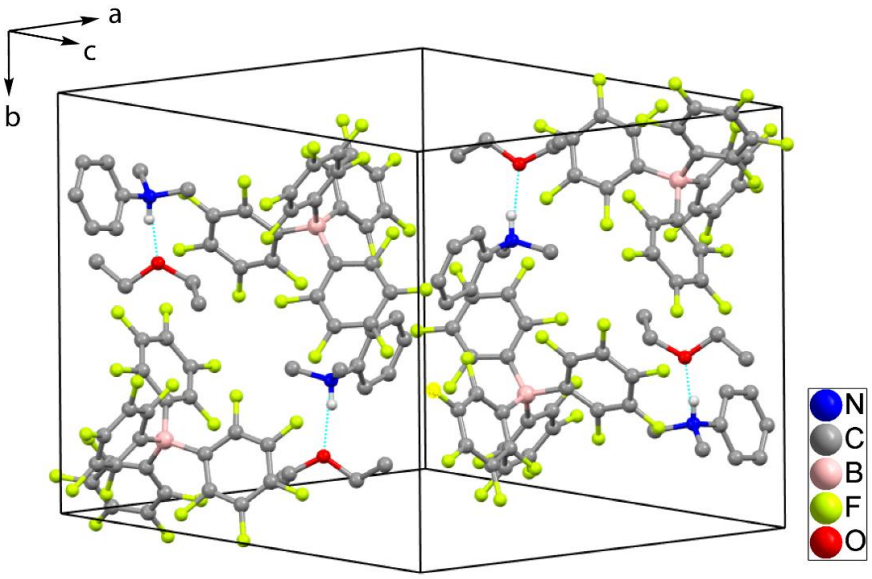

Figure 2.33. Diagram illustrating the molecular packing of [PhMe$_2$NH]B(C_6F_5)$_4$.(C_2H_5)$_2$O at 100 K (all of the hydrogens except for the N-proton have been omitted for clarity).

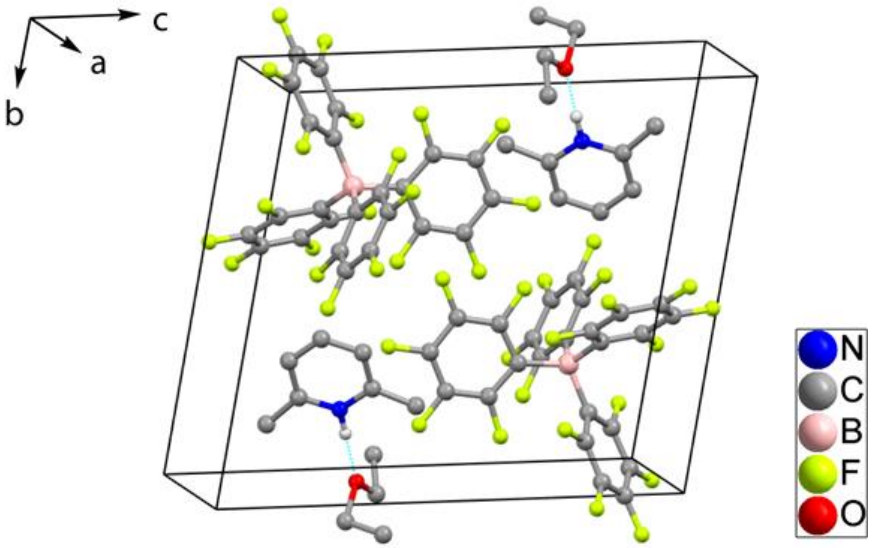

Figure 2.34. Diagram illustrating the molecular packing of [2,6-$Me_2PyH]B(C_6F_5)_4.(C_2H_5)_2O$ at 100 K (all of the hydrogens except for the N-proton have been omitted for clarity

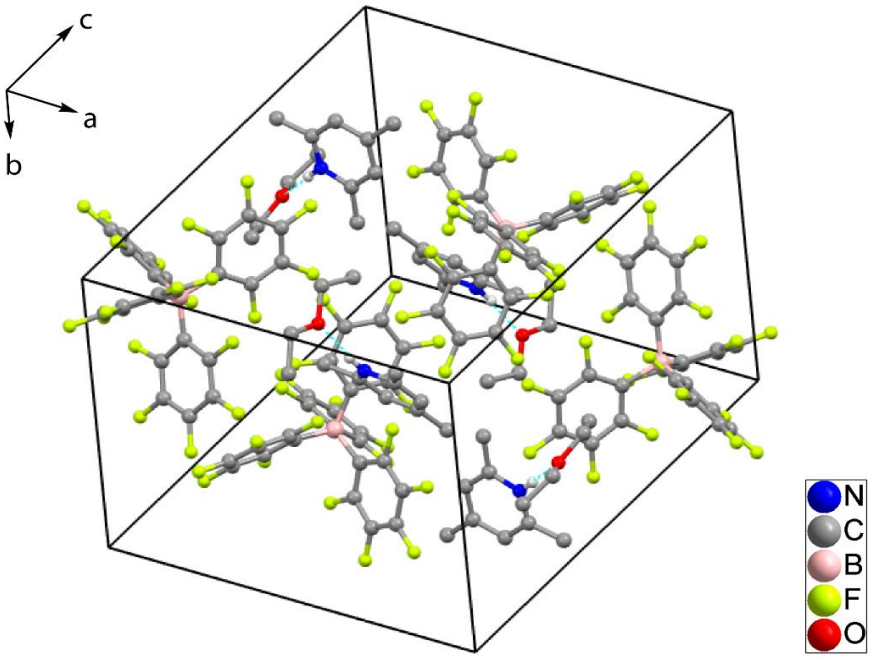

Figure 2.35. Diagram illustrating the molecular packing of [2,4,6-$Me_3PyH]B(C_6F_5)_4.(C_2H_5)_2O$ at 100 K (all of the hydrogens except for the N-proton have been omitted for clarity).

Table 2.5. Crystallographic Data and Data Collection Parameters.

	[$PhMe_2NH$]$BArF_{20}$.$(C_2H_5)_2O$	[2,4,6-Me_3PyH]$BArF_{20}$.$(C_2H_5)_2O$	[2,6-Me_3PyH]$BArF_{20}$.$(C_2H_5)_2O$
Formula	$C_{36}H_{22}BF_{20}NO$	$C_{36}H_{22}BF_{20}NO$	$C_{35}H_{20}BF_{20}NO$
T (K)	100(2)	100(2)	100(2)
Formula weight	875.35	875.35	861.33
Crystal system	Monoclinic	Monoclinic	Triclinic
Space group	*P* 2_1/n	*P* 2_1/n	*P* -1
a, Å	14.9558(2)	14.4017(2)	8.9116(4)
b, Å	15.6222(2)	16.2969(2)	13.3322(5)
c, Å	16.5644(3)	16.1025(3)	14.7542(5)
α , deg	90	90	101.560(3)
β, deg	114.105(2)	106.786(2)	96.514(3)
γ, deg	90	90	90.220(3)
V, Å3	3532.66(10)	3618.27(10)	1705.68(12)
Z	4	4	2
Radiation (λ, Å)	CuKα (1.54178)	CuKα (1.54178)	CuKα (1.54178)
*d*calcd, g•cm^{-3}	1.646	1.607	1.677
F(000)	1752	1752	860
Crystal size (mm^3)	0.502 x 0.257 x 0.168	0.404 x 0.319 x 0.147	0.279 x 0.221 x 0.062
Theta range for data collection	3.361 to 71.900°	3.631 to 71.892°	3.078 to 71.898°
μ, mm^{-1}	1.555	1.518	1.599
No of unique data	6912	7069	6617
Completeness to theta	99.7%	99.7%	99.2%
No. of restraints	0	0	0
No. of params. refined	569	541	579
GOF on F^2	1.050	1.026	1.009
$R1^{a\ [I>2\sigma(I)]}$	0.0317	0.0392	0.0393

$R1^a$ (all data)	0.0339	0.0425	0.0562
$wR2^b$ (all data)	0.0870	0.1113	0.1068
Largest diff. peak and hole	0.340 and −0.226 e.Å-3	0.345 and -0.280 e.Å^{-3}	0.388 and -0.253 e.Å^{-3}

Table 2.6. Crystallographic Data and Data Collection Parameters.

	[HNMe-morp]B(C_6F_5)$_4$. (C_2H_5)$_2$O	[HNMe$_3$]B(C_6F_5)$_4$. (C_2H_5)$_2$O	[HNEt$_3$]B(C_6F_5)$_4$. (C_2H_5)$_2$O
Formula	$C_{33}H_{22}BF_{20}NO_2$	$C_{31}H_{20}BF_{20}NO$	$C_{34}H_{26}BF_{20}NO$
T (K)	100(2)	100(2)	100(2)
Formula weight	855.32	813.29	855.37
Crystal system	Monoclinic	Monoclinic	Orthorhombic
Space group	*P* 2$_1$/n	*P* 2$_1$/n	*P*bca
a, Å	10.6017(2)	14.7769(2)	19.1157(2)
b, Å	21.1391(4)	14.3967(2)	16.9019(2)
c, Å	16.9979(2)	16.3053(2)	21.2863(2)
α , deg	90	90	90
β, deg	106.165(2)	111.528(2)	90
γ, deg	90	90	90
V, Å3	3658.80(11)	3226.78(8)	6877.43(13)
Z	4	4	8
Radiation (λ, Å)	CuKα (1.54178)	CuKα (1.54178)	CuKα (1.54178)
*d*calcd, g•cm^{-3}	1.553	1.674	1.652
F(000)	1712	1624	3440
Crystal size (mm^3)	0.371 x 0.244 x 0.169	0.627 x 0.513 x 0.244	0.500 x 0.343 x 0.151
Theta range for data collection	3.420 to 71.900°	3.457 to 71.895°	4.062 to 71.898°
μ, mm^{-1}	1.505	1.646	1.576

No of unique data	7149	6308	6735
Completeness to theta	99.9%	99.6%	99.8%
No. of restraints	0	0	0
No. of params. refined	526	496	523
GOF on F^2	1.046	1.047	1.046
$R1^{a}$ [I> 2σ(I)]	0.0482	0.0390	0.0349
$R1^{a}$ (all data)	0.0587	0.0412	0.0376
$wR2^{b}$ (all data)	0.1288	0.1072	0.0959
Largest diff. peak and hole	1.312 and -0.739 e.Å^{-3}	0.395 and -0.294 e.Å^{-3}	0.688 and -0.367 e.Å^{-3}

CHAPTER III: UNDERSTANDING THE NATURE OF THE BRIDGING OXYGEN-BASED LIGAND OF THE RESTING STATE OF CCO ACTIVE SITE: TITRATION OF HEME/COPPER μ–OXO ASSEMBLIES WITH PROTONATED NITROGEN BASES FOR THE PK_A DETERMINATION OF THE μ–HYDROXO SPECIES

The following work was accomplished with the aid of Shabnam Hematian.

Introduction

An enzyme at the heart of respiratory processes, cytochrome *c* oxidase (C*c*O) enables the reduction of dioxygen to water at its bimetallic center comprised of a heme site (heme a_3) and copper center (Cu_B); antiferromagnetic coupling was confirmed via magnetic susceptibility studies and EPR measurements that further suggested the presence of a bridging ligand.[167,168] Despite extensive studies, the nature of the active site bridging ligand in the resting state of the enzyme remains unknown. Recently, femtosecond crystallographic studies from the *Thermus thermophilus* (*T. thermophilus)* enzyme and from density functional theory (DFT) calculations indicate the possibility of an oxygen-based ligand (i.e., water, hydroxo, or oxo) bridging the two metal centers (Figure 3.1).[169,170] What is known is that protonation of the bridge induces structural changes including bending of the Fe–O–Cu moiety.[139] Consequently, the protonation state of this ligand can control the redox potential of the bimetallic center and play a key role in proton translocation across the mitochondrial inner membrane.

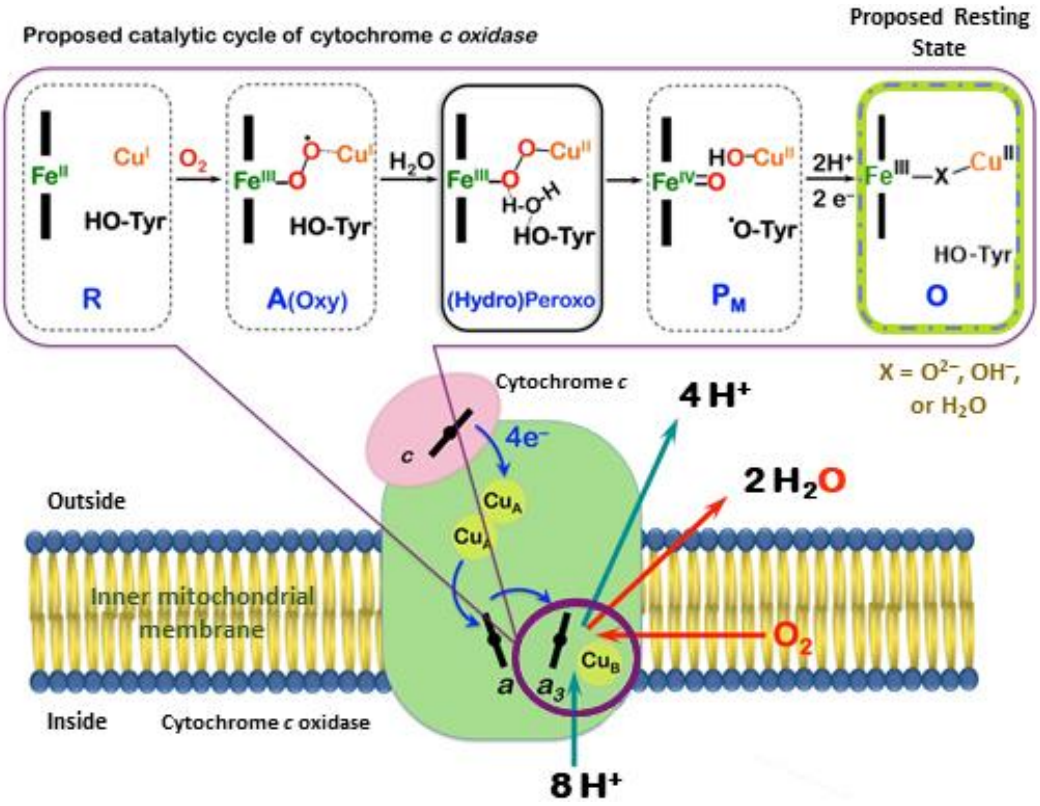

Figure 3.1. Schematic representation of C*c*O in the inner mitochondrial membrane.

Initial attempts at modeling the C*c*O heme a_3/Cu_B dioxygen chemistry led to the discovery of heme/Cu μ–oxo complexes.[54,59] Models of the C*c*O active site include the tethered systems $[(^5L)Fe^{III}–O–Cu^{II}]^+$ and $[(^6L)Fe^{III}–O–Cu^{II}]^+$ as well as the untethered systems $[(F_8TPP)Fe^{III}–O–Cu^{II}(tmpa)]^+$ (**1**) and $[(F_8TPP)Fe^{III}–O–Cu^{II}(MePY2)]^+$ (**2**) were synthesized and the pK_a ranges of their μ–hydroxo conjugate acids were determined; these ranges were reported in acetonitrile (MeCN) and are ~15 < pK_a < ~18, 14 < pK_a < 17, and 16.7 < pK_a < 17.6 for the latter three complexes, respectively.[139,142,143] When comparing complex **1** and **2**, the copper ligand changes from tetradentate to tridentate. This single change causes a shift in pK_a toward the most basic range for a μ–hydroxo complex. Especially intriguing is the geometry about the copper center of complex **2** (τ_4' = 0.449) which bears a strikingly similar coordination geometry to that of the enzyme (τ_4' = 0.477). Another heme/Cu μ–oxo complex with a tridentate copper ligand is $[(F_8TPP)Fe^{III}–O–Cu^{II}(AN)]^+$ (Figure 3.2). The copper site of this complex, with a slightly

more electron rich ligand than the pyridine-based MePY2 ligand, also closely resembles that of the C*c*O resting-state active site (τ_4' = 0.527).

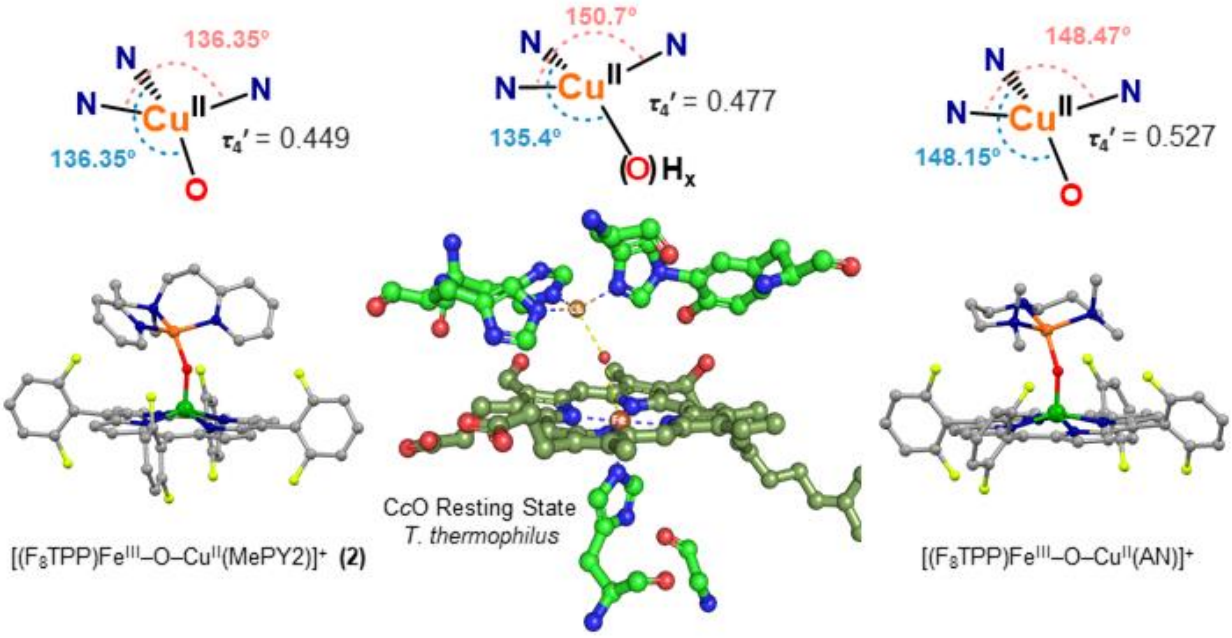

Figure 3.2. Comparison of the copper geometry in C*c*O and synthetic models with tridentate copper ligands.

Exact pK_a values have not been calculated for such complexes given restrictions on both a range of acids with a continuous pK_a scale as well as the use of counteranions with the ability to coordinate to metals that can change the chemical properties of these metal centers. To resolve these issues, we have prepared a range of protonated nitrogen bases (or weak acids) that are paired with non-coordinating counterion *tetrakis*(pentafluorophenyl)borate $[B(C_6F_5)_4]^-$ and that span from 12.3 to 18.46 pK_a (MeCN) units as discussed in Chapter 2 Table 2.3. Here we present pK_a values for systems with variations in both the copper environment and heme site (i.e., the μ–hydroxo complexes of **1**, **2**, and the novel complex $[(TPP)Fe^{III}–O–Cu^{II}(TMPA)]^+$ (**3**), Fig. 3.3).

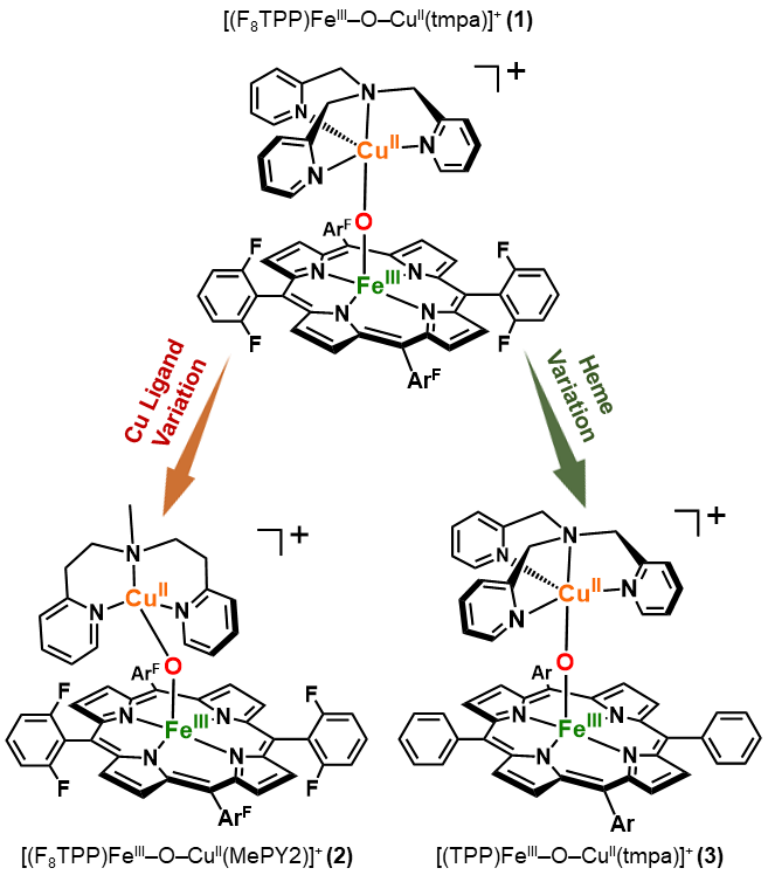

Figure 3.3. Structures of synthetic heme/Cu μ–oxo complexes.

NMR AND UV-VIS TITRATIONS

In order to ensure the products formed through titration experiments with protonated nitrogen bases were the *μ*–hydroxo (*μ*–OH) complexes, the *μ*–oxo complexes were first titrated with the strong acid $[H(OEt_2)_2][B(C_6F_5)_4]$; changes in DCM to both the nuclear magnetic resonance (NMR) and UV-visible (UV-vis) spectra consistent with heme/Cu *μ*–OH complex formation were observed for complexes **1** and **3**. Complex **2** appears to form the *μ*–OH complex at NMR concentrations (Figure 3.9) but a mixture of both the *μ*–OH complex and $[(F_8TPP)Fe^{III}(X)_2]^+$ in UV-vis concentrations (Figure 3.11), where X represents two axial ligands (possibly solvent molecules or counteranions). After addition of the strong acid (up to 2 equivalents), the Cu ligand protons remain visible in the upfield region (-150 to 0 ppm) of the NMR spectra of samples of **1** and **3** (Figures 3.4 and 3.10, respectively).

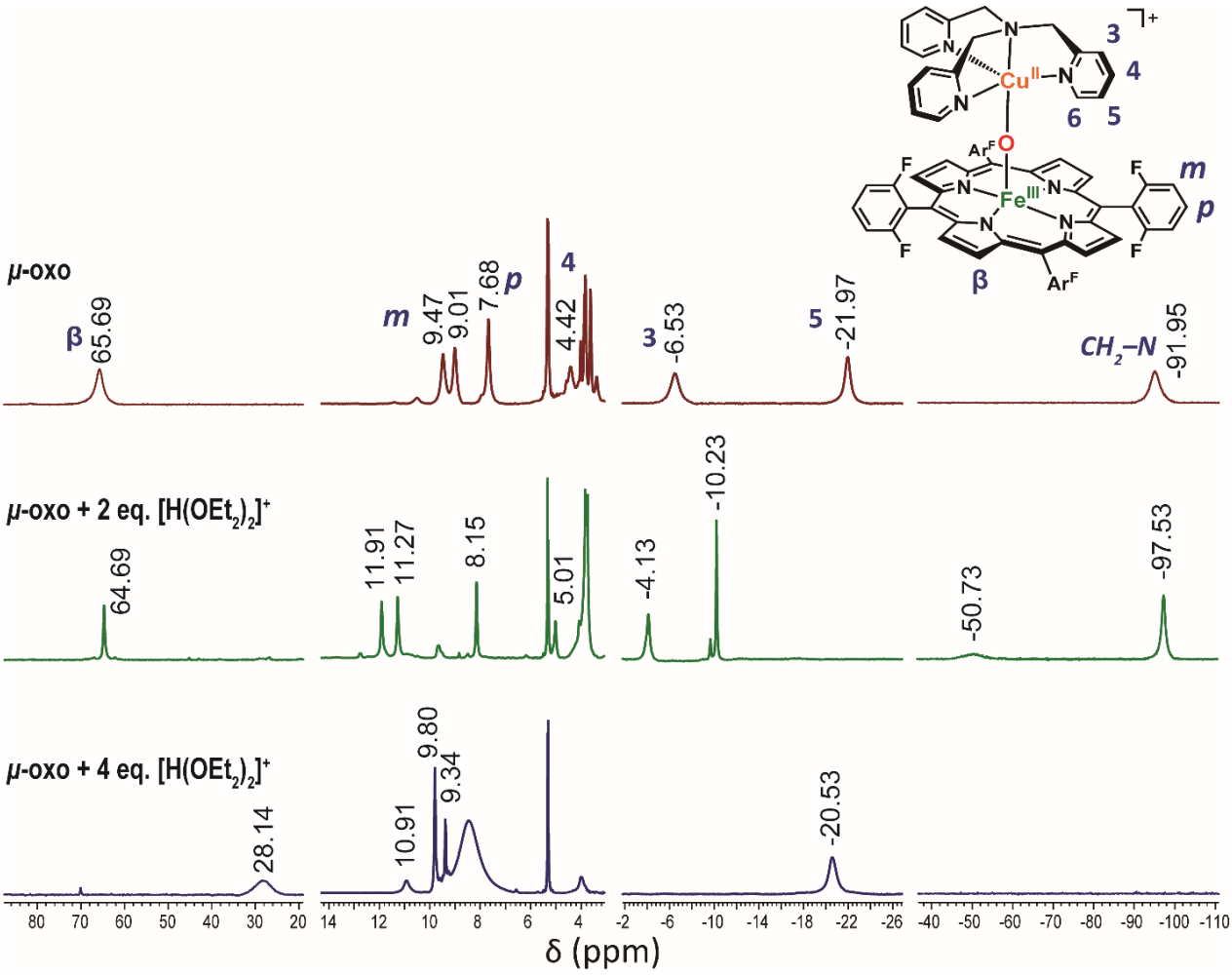

Figure 3.4. ^{1}H-NMR spectrum of the titration of complex **1** with $[H(OEt_2)_2][B(C_6F_5)_4]$ in CD_2Cl_2.

It is believed the copper moiety remains bound, through the protonated bridging ligand (i.e., OH^-), to the heme site due to the Cu ligand protons still experiencing the current induced by the porphyrin ligand. Continuing the titration up to 4 equivalents of $[H(OEt_2)_2]^+$ induces breaking of the Fe–O(H) bond to form the $[(F_8TPP)Fe^{III}(X)_2]^+$ complex. This was further confirmed by authentic NMR samples containing either the Cu^{II} complex, $[(tmpa)Cu^{II}(MeCN)]^{2+}$, or ferric heme, $[(F_8TPP)Fe^{III}(THF)_2]^+$. The former complex has proton shifts at ~30 and 10.4 ppm for the 3 and 5, and 4 protons respectively, and for the latter the pyrrolic protons resonate at 25 ppm and the *para*- and *meta*-phenyl proton signals appear at 10.2 and 9.4 ppm, respectively. (Figures 3.6 and 3.8).

Similarly, in the UV-vis spectra of the titrations of complexes **1** and **3** with $[H(OEt_2)_2]^+$ (Figures 3.14-3.15 and 3.19-3.20), a shift can be seen from the *μ*–oxo features, such as the Soret band, to those of the *μ*–OH complex. For example, the Soret band characteristic for complex **3** in dichloromethane (DCM) is present at 441 nm. Addition of up to 1 equivalent of $[H(OEt_2)_2]^+$ causes a gradual shift to a new absorbance maximum at 409 nm for the *μ*–OH complex as seen in Figure 3.5a. The same Soret and Q-bands are attained when titrating complex **3** with protonated nitrogen bases 2-methylpyridinium $[2\text{-MePyH}]^+$, 2,6-dimethylpyridinium $[2,6\text{-Me}_2\text{PyH}]^+$ (Figure 3.5b), and 2,4,6-trimethylpyridinium $[2,4,6\text{-Me}_3\text{PyH}]^+$.

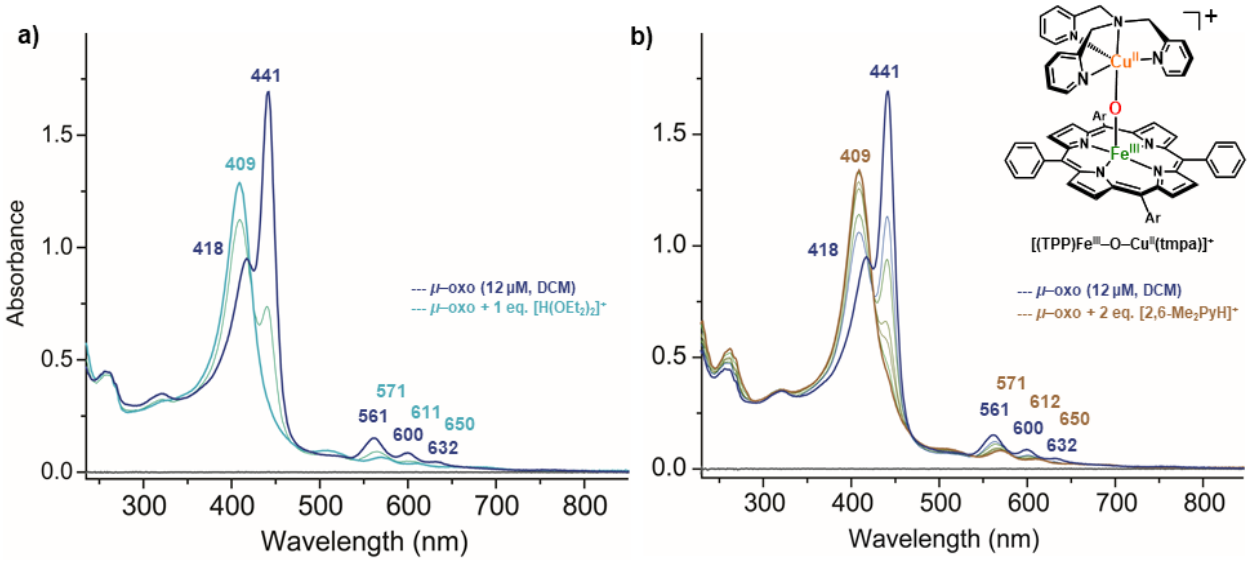

Figure 3.5. UV-vis titration experiments of complex **3** with a) $[H(OEt_2)_2][B(C_6F_5)_4]$ and b) 2,6-dimethylpyridinium in DCM.

Calculation of the pK_a values of our select heme/Cu *μ*–oxo complexes was based on titrations with the weak acids (SI, equations 1-6, Table 3.1). These values are reported in acetonitrile (MeCN) as it is the solvent with the most comprehensive pK_a scale. Also, titrations conducted in MeCN provided similar results as those in DCM regarding weak acid equivalents added to form the heme/Cu *μ*–hydroxo complexes.

Table 3.1. Characteristic pK_a and Soret bands for μ–hydroxo/μ–oxo complex conjugate pairs.

μ-Hydroxo	**pK_a (MeCN)**	**Soret (μ-oxo, nm)**	**Soret (μ-hydroxo, nm)**	**$[H(OEt_2)_2]^+$ Equiv. to break Fe–O(H) bond**
$[(F_8TPP)Fe^{III}–(OH)–Cu^{II}(MePY2)]^{2+}$	15.3*	407/446	406	3
$[(F_8TPP)Fe^{III}–(OH)–Cu^{II}(tmpa)]^{2+}$	13.3	437	405	3
$[(TPP)Fe^{III}–(OH)–Cu^{II}(tmpa)]^{2+}$	14.6	441	409	2

*Measured with only one acid.

Discussion

We have shown that calculating the pK_a values of heme/Cu μ–hydroxo complexes is possible with a series of protonated nitrogen bases, or weak acids, that range between 12.3 and 18.76 pK_a units in MeCN. Most importantly, our acids contain a non-coordinating anion $[B(C_6F_5)_4]^-$ for the anion to be as neutral, or non-reactive, as possible. Our results indicate that changing the porphyrin ligand from the electron withdrawing F_8TPP to the more electron rich TPP ligand causes an increase of about 1.3 pK_a (MeCN) units. As reported by Pecoraro et al, the pK_a in MeCN is about 7.5 ± 1 units greater than in water.[149] Thus, the pK_a values of these synthetic models (5.8 ± 1 for the μ–OH of **1** and 7.1 ± 1 for the μ–OH of **2**) can now be compared to that of biological complexes such as C*c*O. Including the pK_a of synthetic heme/Cu complexes as an added metric for their characterization will allow both a better understanding of how differing ligands change the reactivity of these μ–oxo and μ–hydroxo complexes and also how to better model the structure of the C*c*O active site.

Supporting Information

NMR Spectra

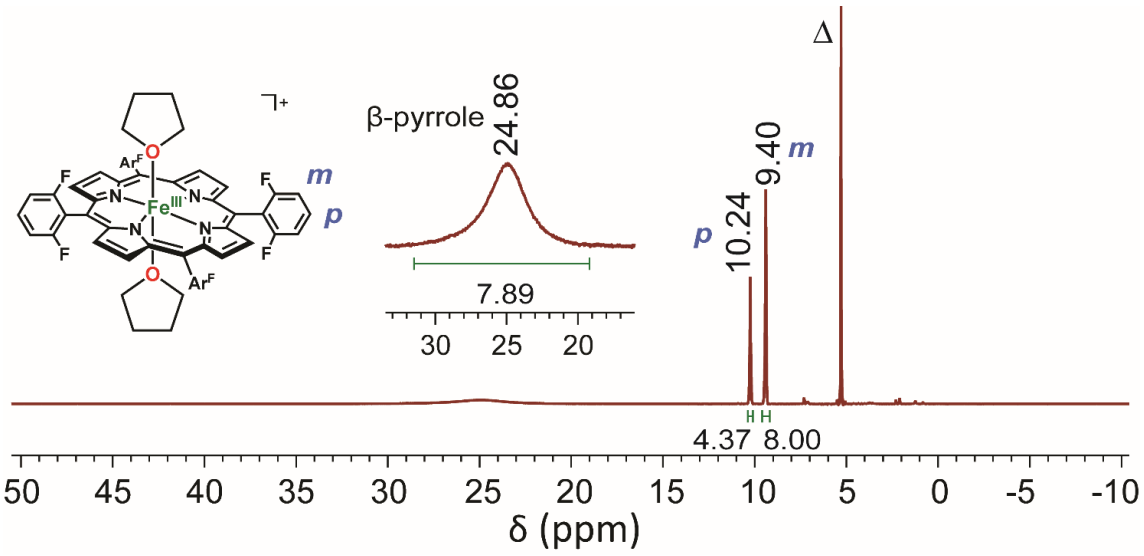

Figure 3.6. 1H-NMR spectrum of [(F8TPP)FeIII(THF)2][SbF6] in CD2Cl2.

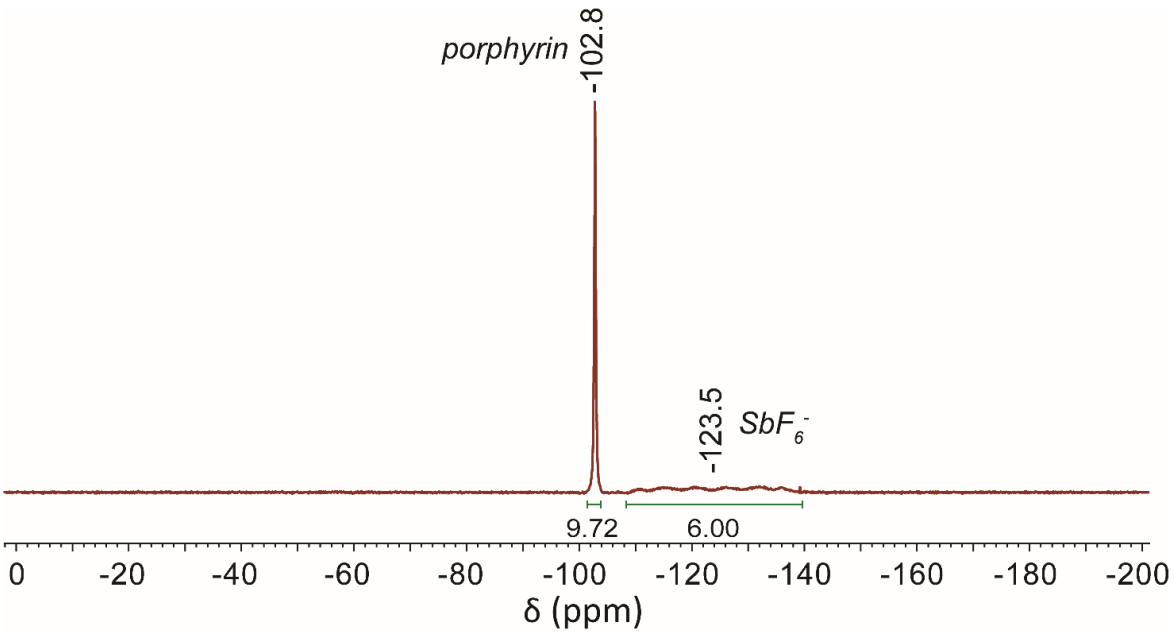

Figure 3.7. ^{19}F-NMR spectrum of [(F_8TPP)Fe^{III}($THF)_2$][SbF_6] in CD_2Cl_2.

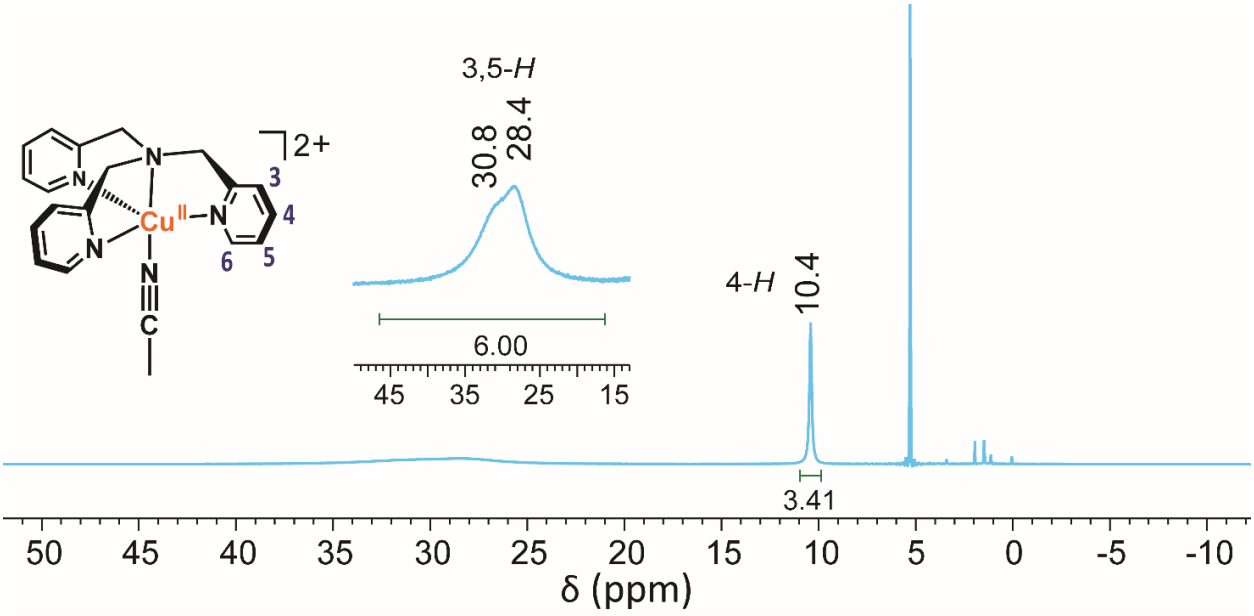

Figure 3.8. ^{1}H-NMR spectrum of [(tmpa)Cu^{II}(MeCN)][ClO$_4$]$_2$ in CD_2Cl_2.

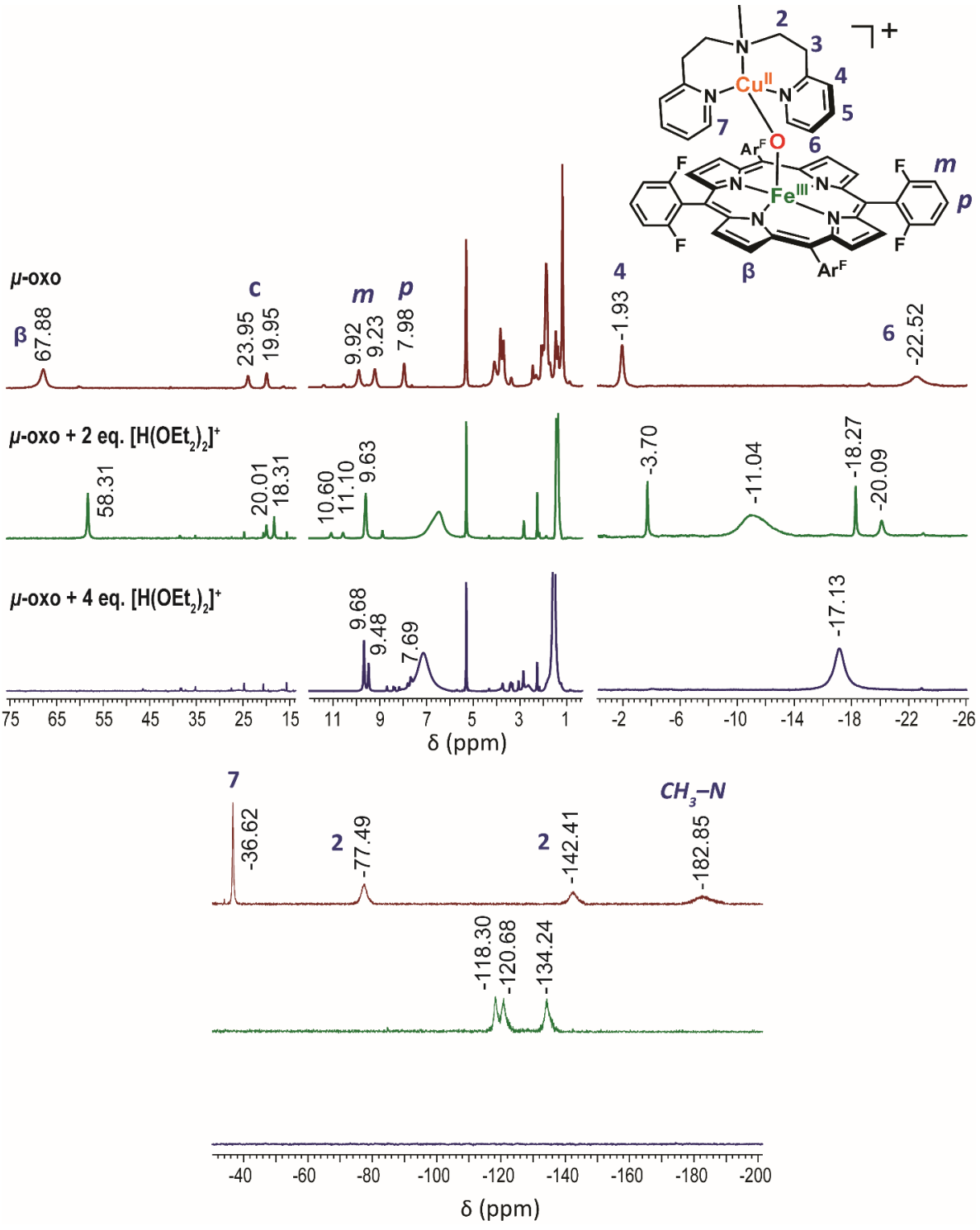

Figure 3.9. ^{1}H-NMR spectrum of the titration of $[(F_8TPP)Fe^{III}–O–Cu^{II}(MePY2)]^+$ with $[H(OEt_2)_2][B(C_6F_5)_4]$ in CD_2Cl_2.

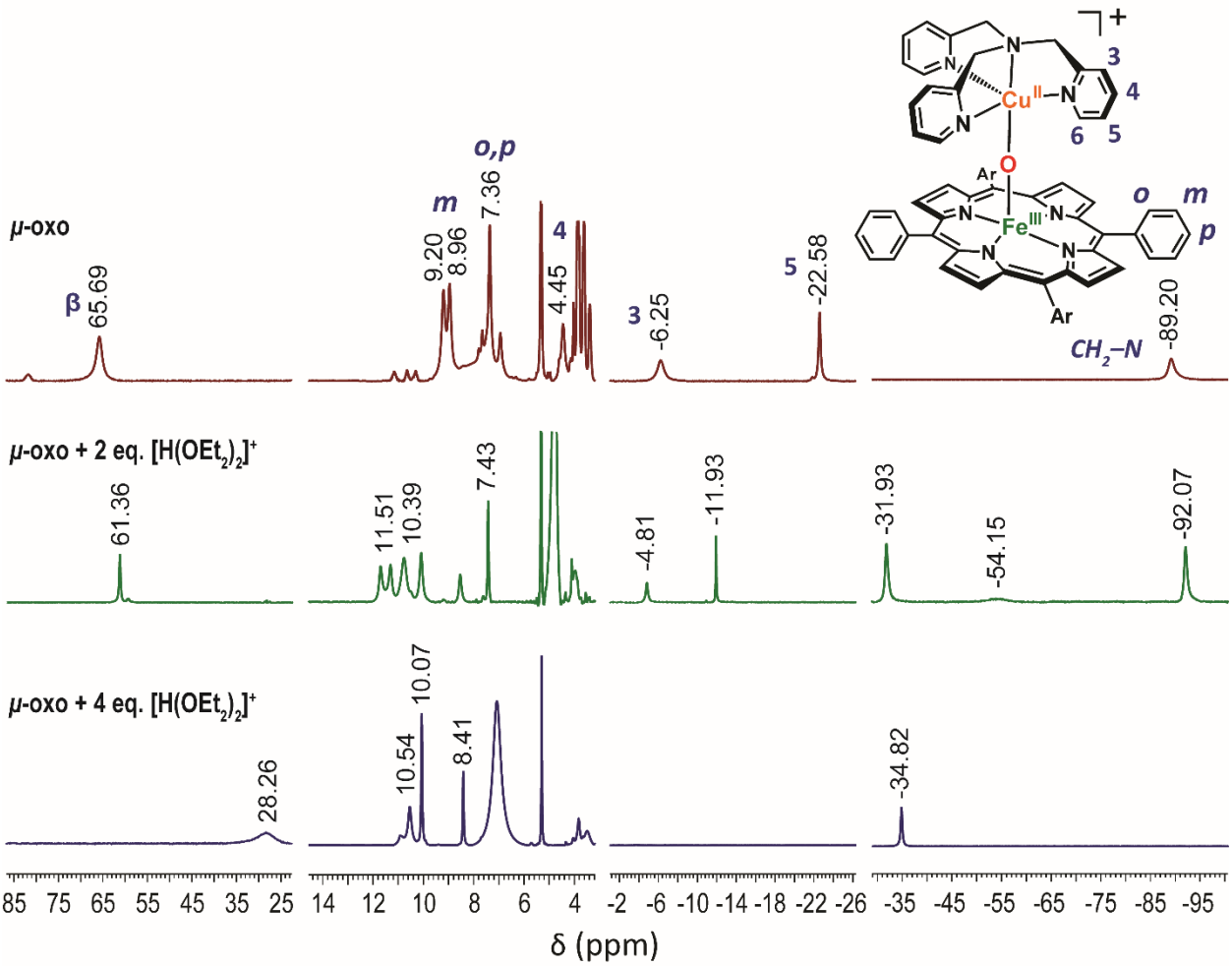

Figure 3.10. ^{1}H-NMR spectrum of the titration of [(TPP)Fe^{III}–O–Cu^{II}(tmpa)]$^{+}$ with $[H(OEt_2)_2][B(C_6F_5)_4]$ in CD_2Cl_2.

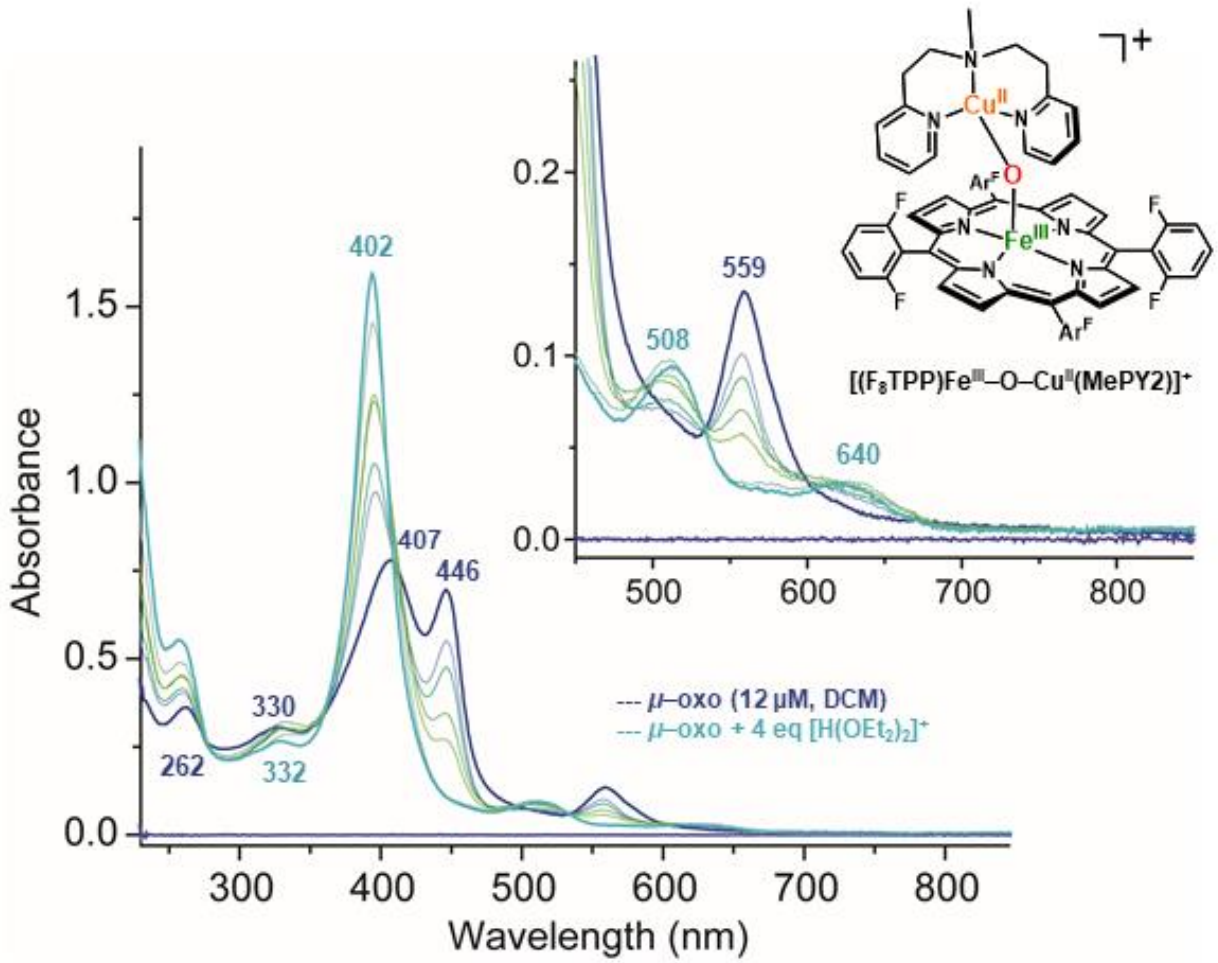

Figure 3.11. UV-vis spectrum of the titration of $[(F_8TPP)Fe^{III}–O–Cu^{II}(MePY2)]^+$ with the strong acid $[H(OEt_2)_2]^+$ recorded in DCM at room temperature.

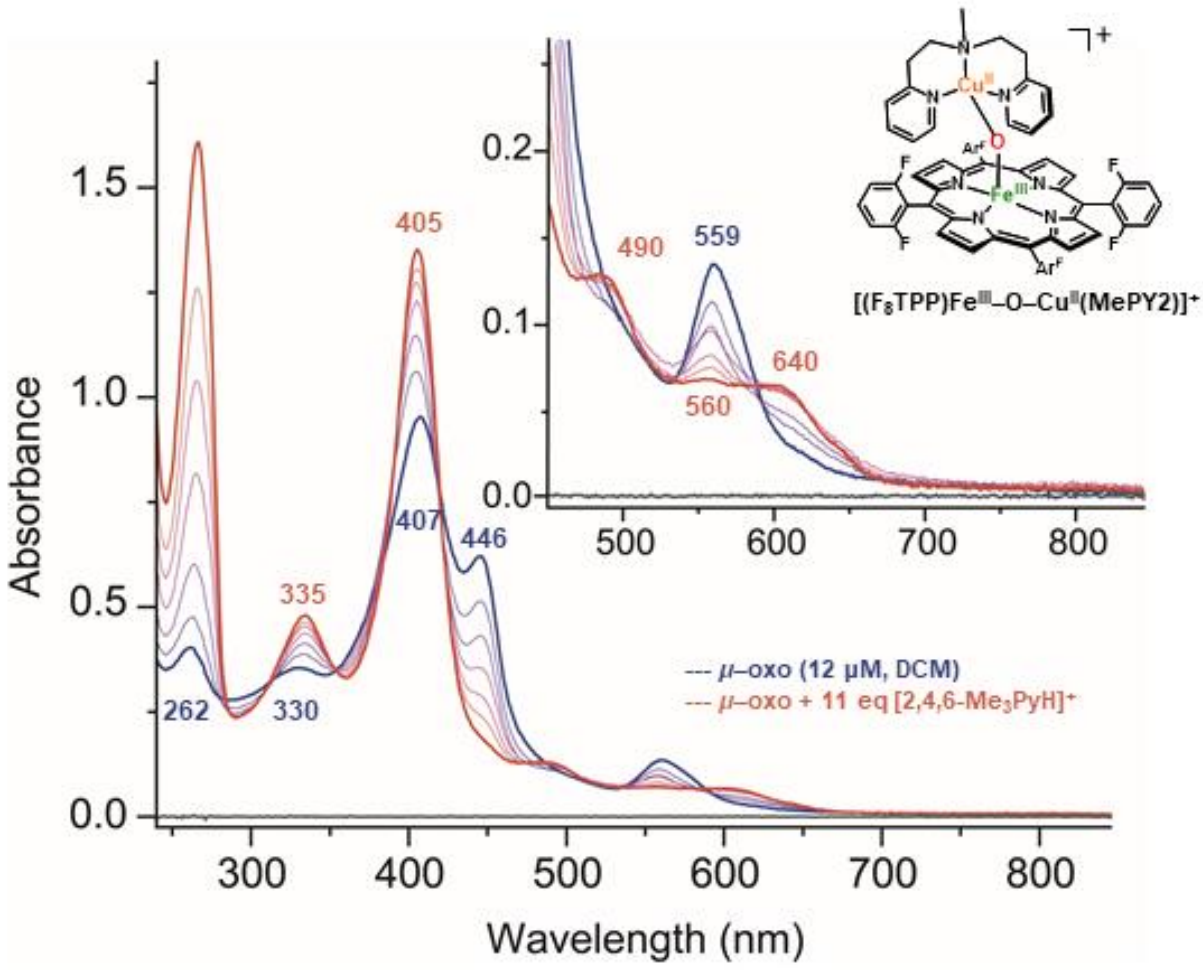

Figure 3.12. UV-vis spectrum of the titration of $[(F_8TPP)Fe^{III}–O–Cu^{II}(MePY2)]^+$ with the protonated nitrogen base $[2,4,6\text{-}Me_3PyH]^+$ recorded in DCM at room temperature.

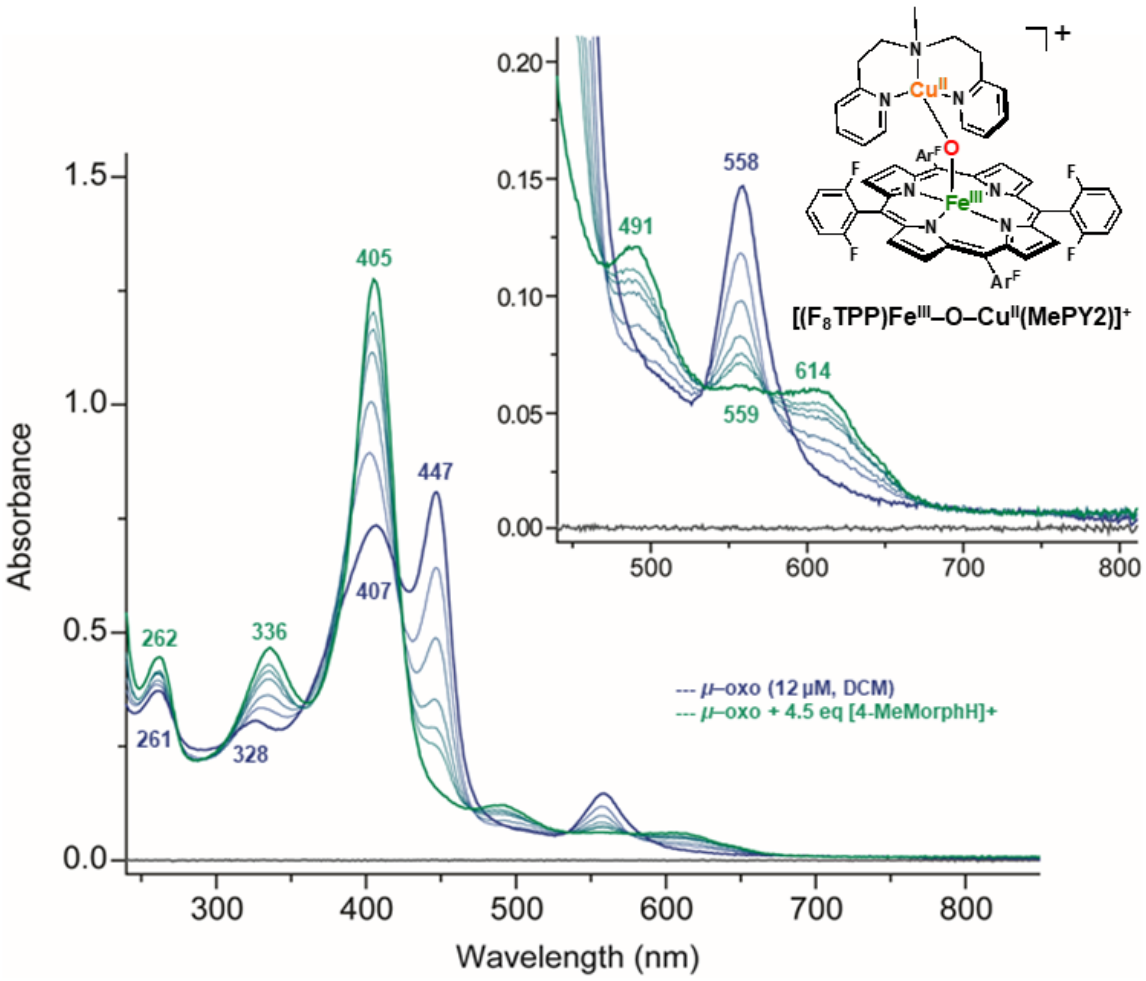

Figure 3.13. UV-vis spectrum of the titration of $[(F_8TPP)Fe^{III}–O–Cu^{II}(MePY2)]^+$ with the protonated nitrogen base $[4\text{-MeMorphH}]^+$ recorded in DCM at room temperature.

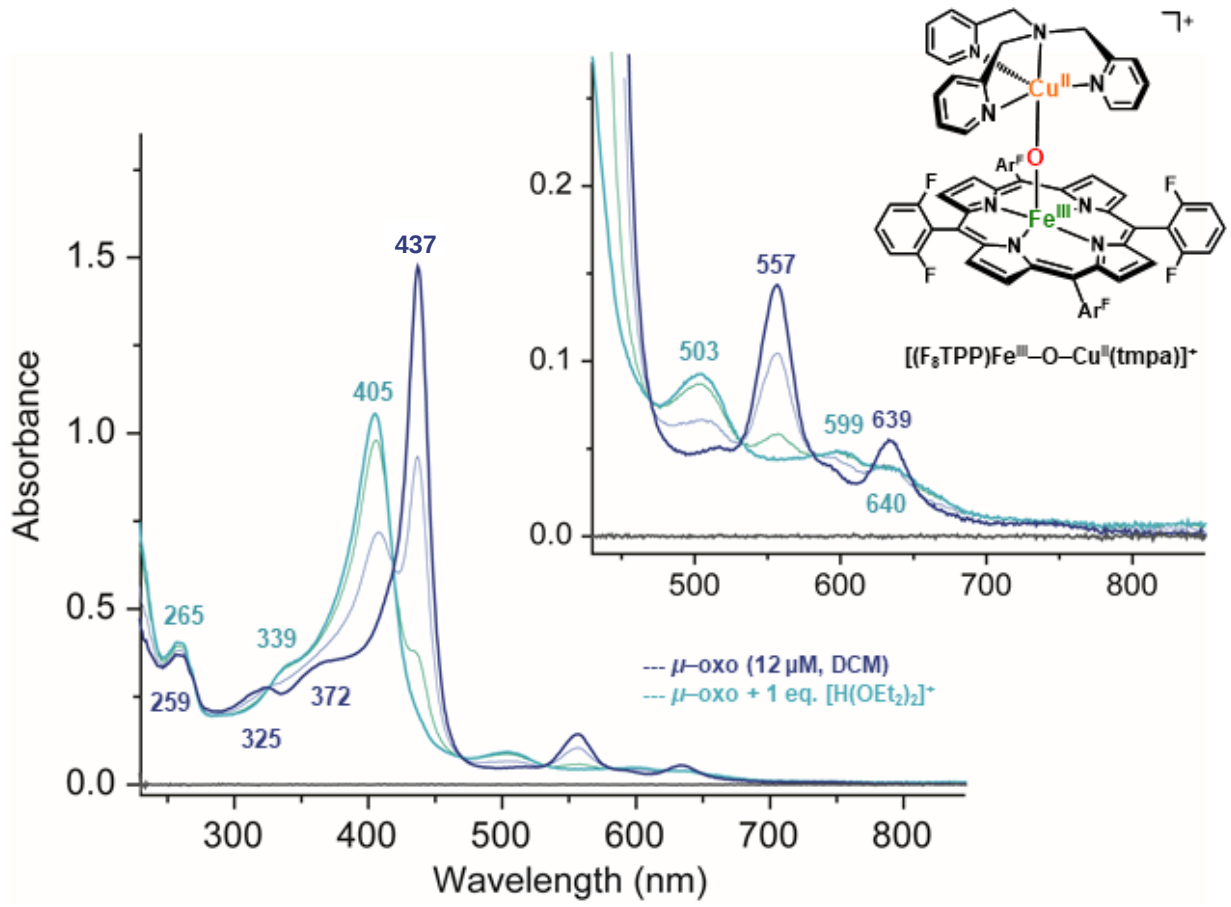

Figure 3.14. UV-vis spectrum of the titration of $[(F_8TPP)Fe^{III}–O–Cu^{II}(tmpa)]^+$ with the strong acid $[H(OEt_2)_2]^+$ recorded in DCM at room temperature to form the *μ*–hydroxo species.

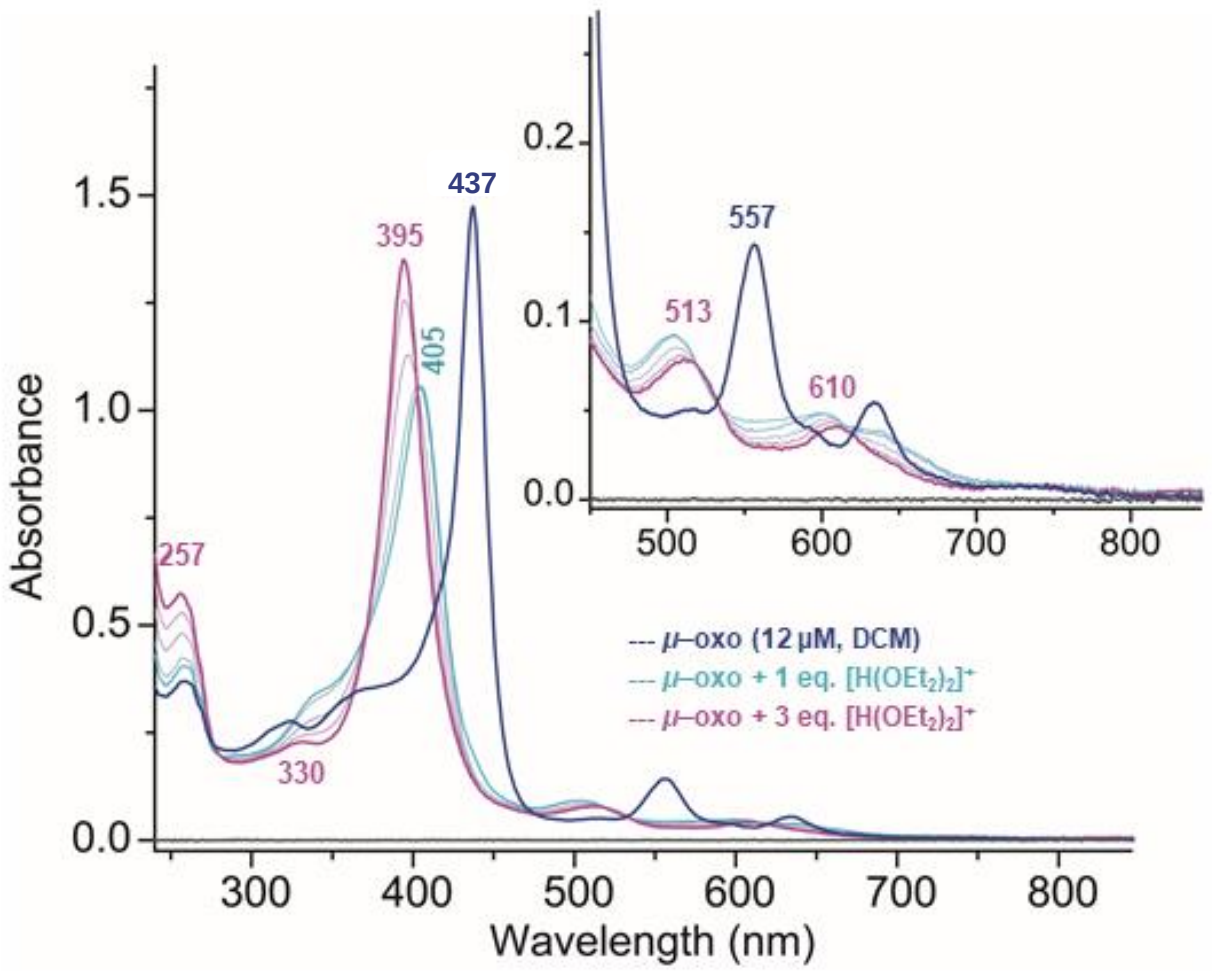

Figure 3.15. UV-vis spectrum of the titration of $[(F_8TPP)Fe^{III}–O–Cu^{II}(tmpa)]^+$ with the strong acid $[H(OEt_2)_2]^+$ recorded in DCM at room temperature. Formation of the compound $[(F_8TPP)Fe^{III}(X)_2]^{2+}$, or free Fe^{III} porphyrin, is observed with addition of excess strong acid.

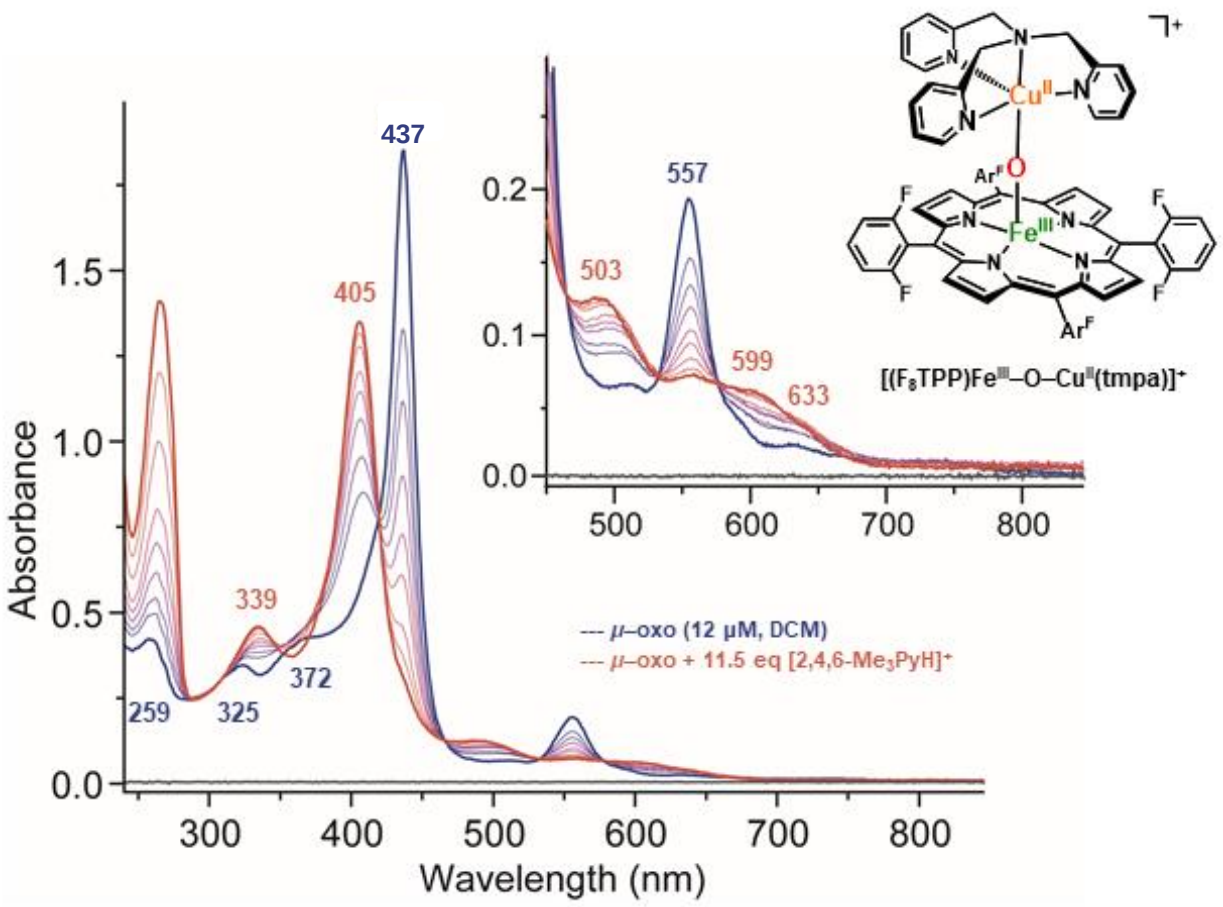

Figure 3.16. UV-vis spectrum of the titration of $[(F_8TPP)Fe^{III}–O–Cu^{II}(tmpa)]^+$ with the protonated nitrogen base $[2,4,6\text{-}Me_3PyH]^+$ recorded in DCM at room temperature.

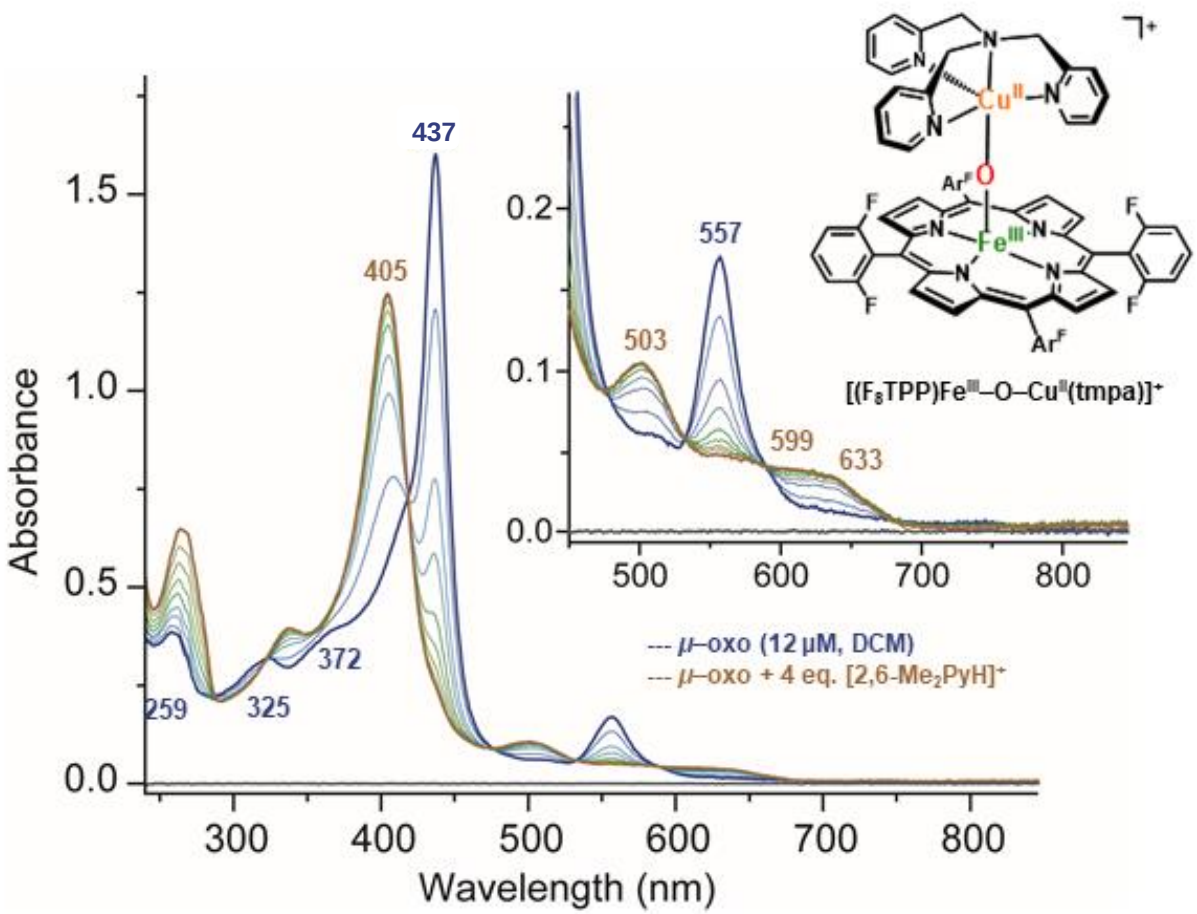

Figure 3.17. UV-vis spectrum of the titration of $[(F_8TPP)Fe^{III}–O–Cu^{II}(tmpa)]^+$ with the protonated nitrogen base $[2,6\text{-}Me_2PyH]^+$ recorded in DCM at room temperature.

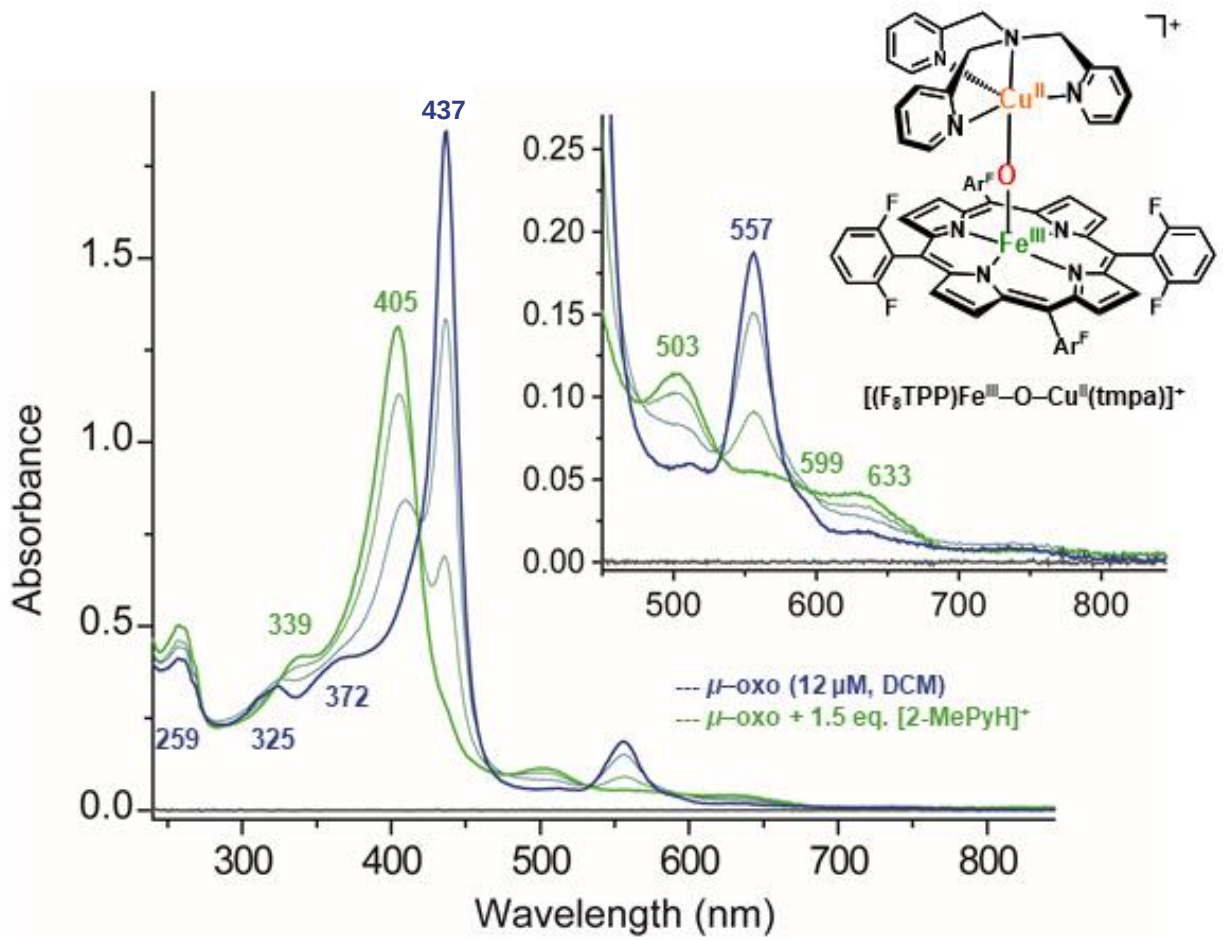

Figure 3.18. UV-vis spectrum of the titration of $[(F_8TPP)Fe^{III}–O–Cu^{II}(tmpa)]^+$ with the protonated nitrogen base $[2\text{-MePyH}]^+$ recorded in DCM at room temperature.

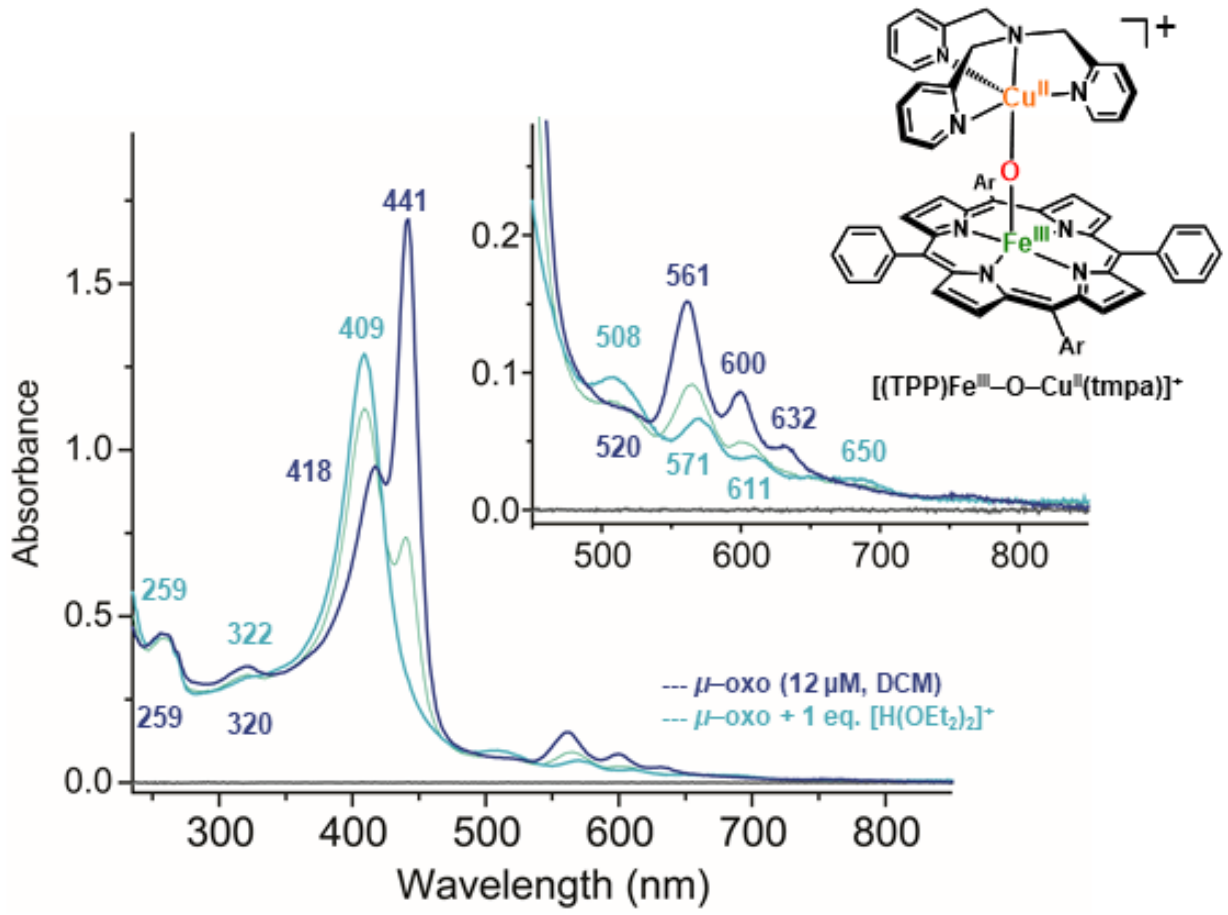

Figure 3.19. UV-vis spectrum of the titration of $[(TPP)Fe^{III}–O–Cu^{II}(tmpa)]^{+}$ with the strong acid $[H(OEt_2)_2]^{+}$ recorded in DCM at room temperature.

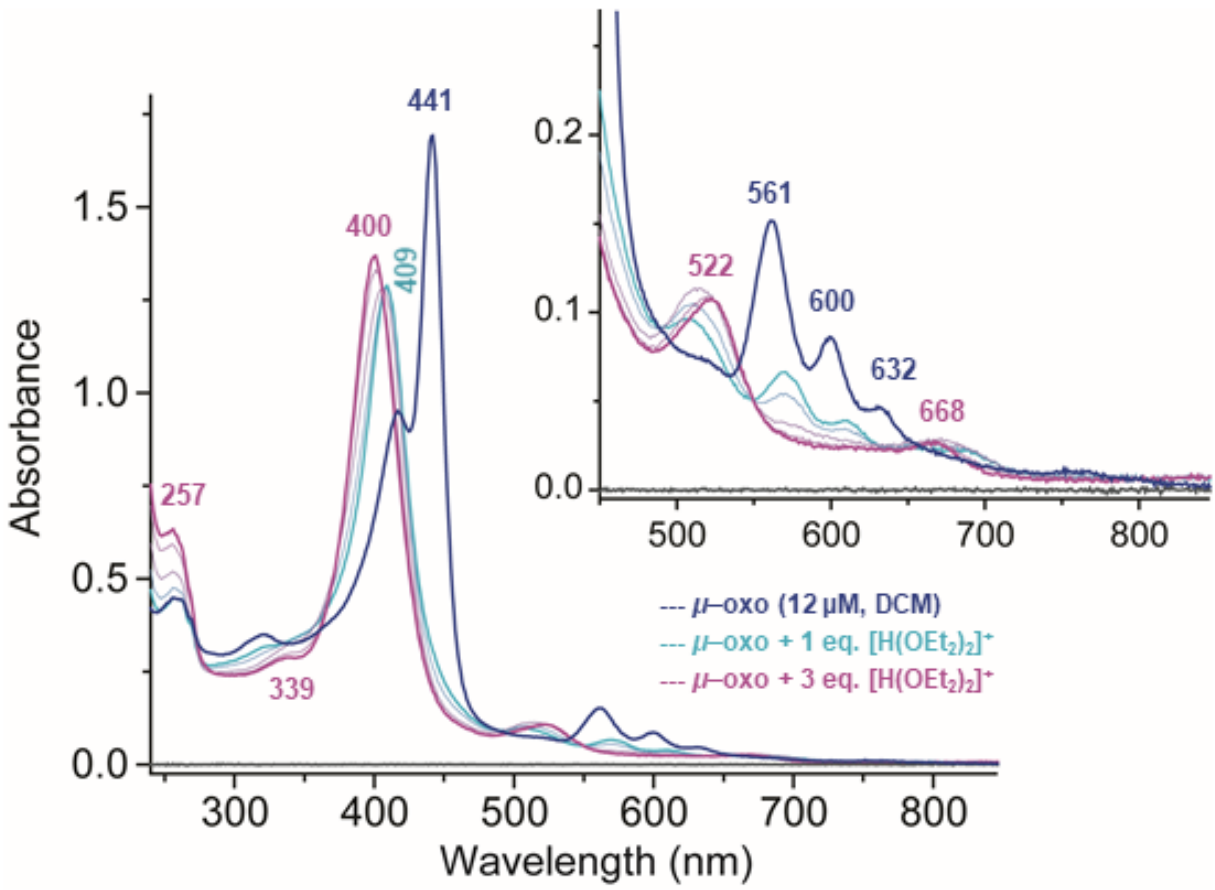

Figure 3.20. UV-vis spectrum of the titration of $[(TPP)Fe^{III}–O–Cu^{II}(tmpa)]^{+}$ with the strong acid $[H(OEt_2)_2]^{+}$ recorded in DCM at room temperature. Formation of the compound $[(TPP)Fe^{III}(X)_2]^{2+}$, or free Fe^{III} porphyrin, is observed with addition of excess strong acid.

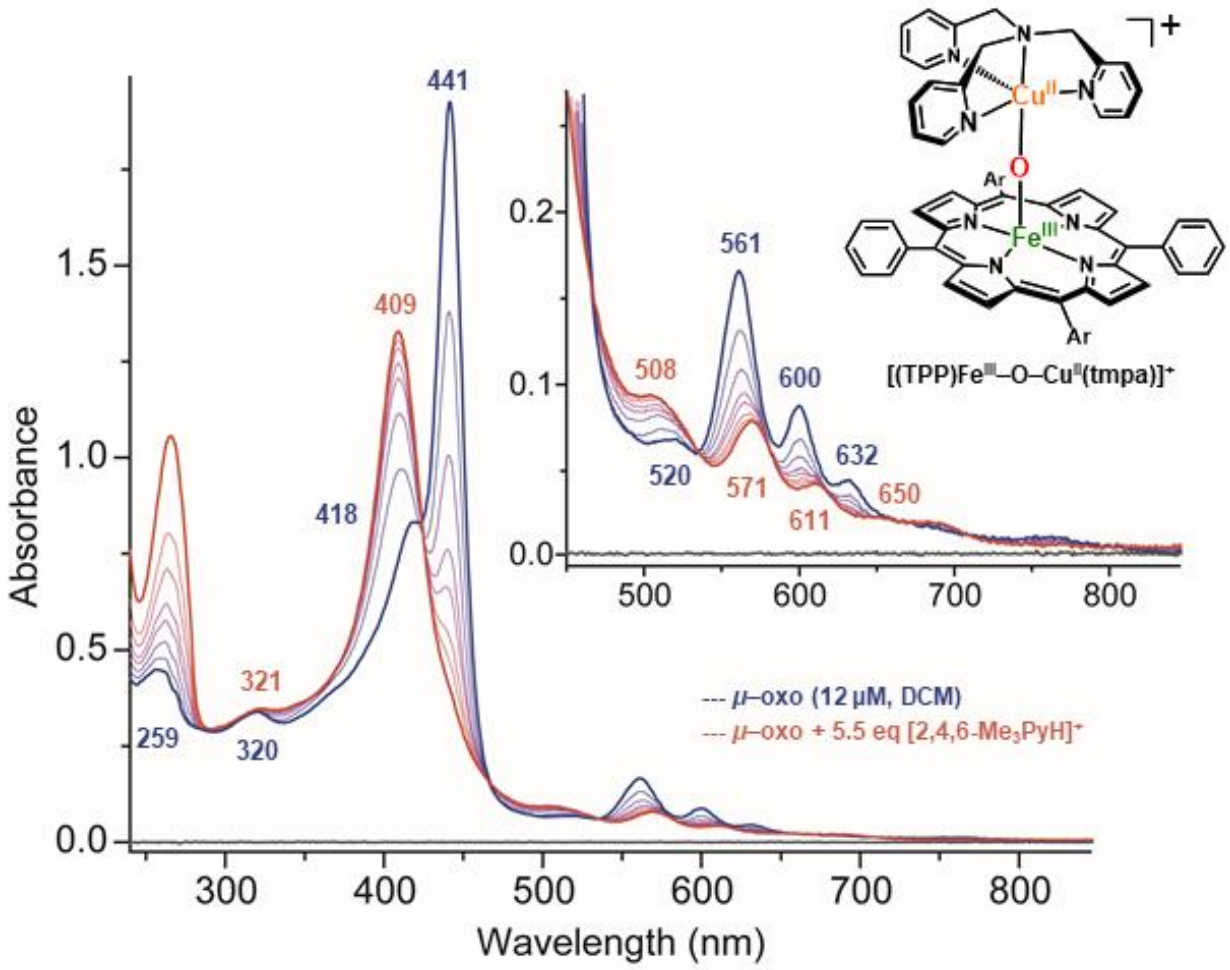

Figure 3.21. UV-vis spectrum of the titration of $[(F_8TPP)Fe^{III}–O–Cu^{II}(tmpa)]^+$ with the protonated nitrogen base $[2,4,6\text{-}Me_3PyH]^+$ recorded in DCM at room temperature.

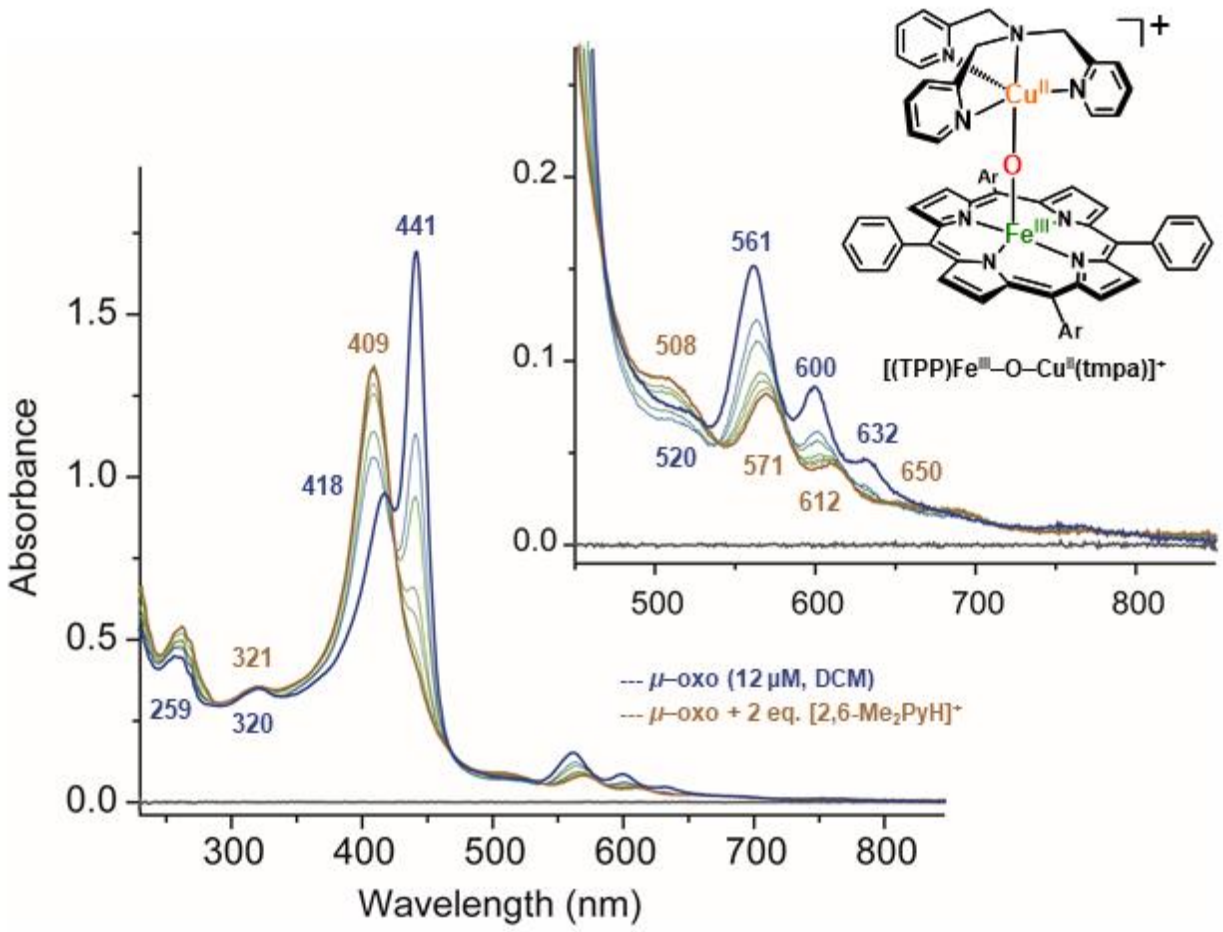

Figure 3.22. UV-vis spectrum of the titration of $[(TPP)Fe^{III}–O–Cu^{II}(tmpa)]^+$ with the protonated nitrogen base $\{2,6\text{-}Me_2PyH]^+$ recorded in DCM at room temperature.

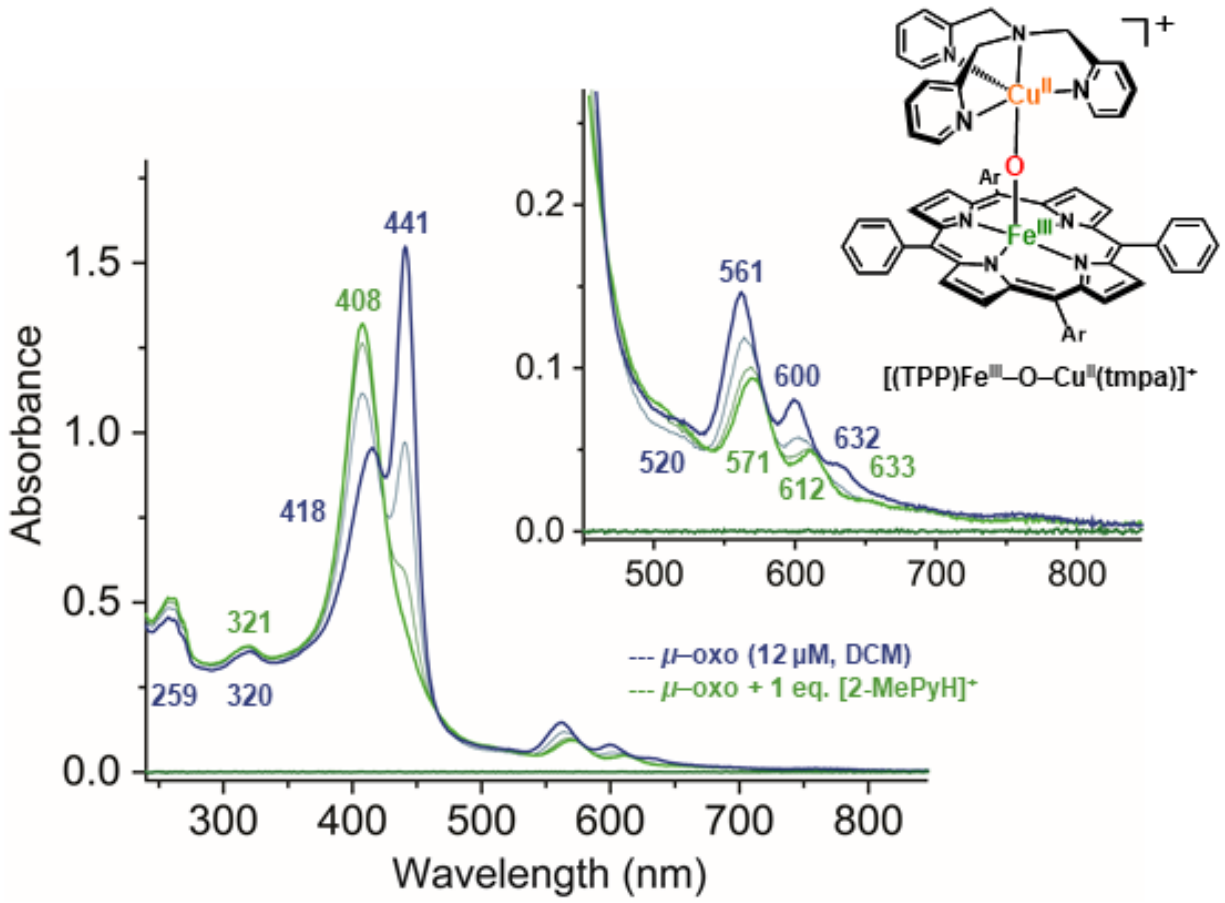

Figure 3.23. UV-vis spectrum of the titration of $[(TPP)Fe^{III}–O–Cu^{II}(tmpa)]^+$ with the protonated nitrogen base $\{2\text{-MePyH}\}^+$ recorded in DCM at room temperature.

Equations for Calculating pK_a:

$$AH \rightleftharpoons A^- + H^+ \ldots K_a\ BH \quad (1)$$

$$\mu\text{–}OH \rightleftharpoons \mu\text{–}oxo + H^+ \ldots K_a\ \mu\text{–}OH \quad (2)$$

$$AH\ +\ \mu\text{–}oxo \rightleftharpoons A^- + \mu\text{–}OH \ldots K_{titration} \quad (3)$$

$$K_a\ BH = \frac{[A^-][H^+]}{[AH]} = 10^{-\mathrm{p}K_a\,(BH)} \quad (4)$$

$$K_a\ \mu\text{–}OH = \frac{[\mu\text{–}oxo][H^+]}{[\mu\text{–}OH]} \quad (5)$$

$$K_{titration} = \frac{[A^-][\mu\text{–}OH]}{[AH][\mu\text{–}oxo]} = \frac{K_a\ BH}{K_a\ \mu\text{–}OH} \quad (6)$$

REFERENCES

1. Poulos TL. *Chem. Rev.* 2014; **114**: 3919-3962.

2. Dawson J. *Science* 1988; **240**: 433-439.

3. Chin D-H, La Mar GN and Balch AL. *J. Am. Chem. Soc.* 1980; **102**: 4344-4350.

4. Fleischer EB and Srivastava TS. *J. Am. Chem. Soc.* 1969; **91**: 2403-2405.

5. Hoffman AB, Collins DM, Day VW, Fleischer EB, Srivastava TS and Hoard JL. *J. Am. Chem. Soc.* 1972; **94**: 3620-3626.

6. *In addition to the initial reports mentioned in this review, other structural data for [(TPP)Fe^{III}–O–Fe^{III}(TPP)] with higher accuracy or in different space groups have been reported by Swepston & Ibers, 1985; Kooijmann et al., 2007 (CSD Private Communication, #667666); and Peters et al., 2019.*

7. Swepston PN and Ibers JA. *Acta Crystallogr.* 1985; **C41**: 671-673.

8. Peters MK, Näther C and Herges R. *Acta Crystallogr.* 2019; **E75**: 930-933.

9. Kiong-Lam L, Buchler JW, Kenny JE and Scheidt WR. *Inorg. Chim. Acta* 1986; **123**: 91-97.

10. Cheng L, Lee J, Powell DR and Richter-Addo GB. *Acta Crystallogr.* 2004; **E60**: m1340-m1342.

11. Carroll JM and Norton JR. *J. Am. Chem. Soc.* 1992; **114**: 8744-8745.

12. Evans DR and Reed CA. *J. Am. Chem. Soc.* 2000; **122**: 4660-4667.

13. Goff H and Morgan LO. *Inorg. Chem.* 1976; **15**: 3180-3181.

14. Miller JR, Taies JA and Silver J. *Inorg. Chim. Acta* 1987; **138**: 205-214.

15. Kurtz DM. *Chem. Rev.* 1990; **90**: 585-606.

16. Scheidt WR, Cheng B, Safo MK, Cukiernik F, Marchon JC and Debrunner PG. *J. Am. Chem. Soc.* 1992; **114**: 4420-4421.

17. Evans DR, Mathur RS, Heerwegh K, Reed CA and Xie Z. *Angew. Chem. Intl. Ed.* 1997; **36**: 1335-1337.

18. Kadish KM, Autret M, Ou Z, Tagliatesta P, Boschi T and Fares V. *Inorg. Chem.* 1997; **36**: 204-207.

19. Li M, Shang M, Duval HF and Scheidt WR. *Acta Crystallogr.* 2000; **C56**: 1206-1207.

20. Li A-R, Wei H-H and Gang L-L. *Inorg. Chim. Acta* 1999; **290**: 51-56.

21. Ivanca MA, Lappin AG and Scheidt WR. *Inorg. Chem.* 1991; **30**: 711-718.

22. Jiao X-D, Huang J-W, Ji L-N, Luo B-S and Chen L-R. *J. Inorg. Biochem.* 1997; **65**: 229-233.

23. Hou Y, Zhu Y, Sun J, Zhang X, Tian Y and Jiang J. *CrystEngComm* 2015; **17**: 4699-4704.

24. Landrum JT, Grimmett D, Haller KJ, Scheidt WR and Reed CA. *J. Am. Chem. Soc.* 1981; **103**: 2640-2650.

25. Gold A, Jayaraj K, Doppelt P, Fischer J and Weiss R. *Inorg. Chim. Acta* 1988; **150**: 177-181.

26. Aguiar A, Ribeiro S, Silva AMN, Cunha-Silva L, de Castro B, Silva AMG and Balula SS. *Applied Catalysis A: General* 2014; **478**: 267-274.

27. Karlin KD, Nanthakumar A, Fox S, Murthy NN, Ravi N, Huynh BH, Orosz RD and Day EP. *J. Am. Chem. Soc.* 1994; **116**: 4753-4763.

28. Melin F, Boudon C, Lo M, Schenk KJ, Bonin M, Ochsenbein P, Gross M and Weiss J. *J. of Porphy. Phthalocyanines* 2007; **11**: 212-221.

29. Johnson MR, Seok WK, Ma W, Slebodnick C, Wilcoxen KM and Ibers JA. *J. Org. Chem.* 1996; **61**: 3298-3303.

30. Suzuki M, Tsuge K, Sasaki Y and Imamura T. *Chem. Lett.* 2003; **32**: 564-565.

31. Amanullah S, Saha P, Saha R and Dey A. *Inorg. Chem.* 2019; **58**: 152-164.

32. Cheng B, Hobbs JD, Debrunner PG, Erlebacher J, Shelnutt JA and Scheidt WR. *Inorg. Chem.* 1995; **34**: 102-110.

33. Patra R, Bhowmik S, Ghosh SK and Rath SP. *Eur. J. Inorg. Chem.* 2009: 654-665.

34. Schaefer WP, Ellis PE, Lyons JE and Shaikh SN. *Acta Crystallogr.* 1995; **C51**: 2252-2255.

35. Fidalgo-Marijuan A, Barandika G, Bazán B, Urtiaga MK, Larrea ES, Iglesias M, Lezama L and Arriortua MI. *Dalton Trans.* 2015; **44**: 213-222.

36. Sil D, Khan FS and Rath SP. *Chem. Eur. J.* 2016; **22**: 14585-14597.

37. Ghosh SK, Patra R and Rath SP. *Inorg. Chem.* 2008; **47**: 10196-10198.

38. Sainna MA, Sil D, Sahoo D, Martin B, Rath SP, Comba P and de Visser SP. *Inorg Chem* 2015; **54**: 1919-1930.

39. Ghosh SK and Rath SP. *J. Am. Chem. Soc.* 2010; **132**: 17983-17985.

40. Bhowmik S, Ghosh SK, Layek S, Verma HC and Rath SP. *Chemistry – A European Journal* 2012; **18**: 13025-13037.

41. Ghosh SK, Patra R and Rath SP. *Inorg. Chim. Acta* 2010; **363**: 2791-2799.

42. Ghosh SK, Bhowmik S, Sil D and Rath SP. *Chem. Eur. J.* 2013; **19**: 17846-17859.

43. Khan FS, Pandey AK and Rath SP. *Chem. Eur. J.* 2016; **22**: 16124-16137.

44. Deng Y, Chang CJ and Nocera DG. *J. Am. Chem. Soc.* 2000; **122**: 410-411.

45. Hodgkiss JM, Chang CJ, Pistorio BJ and Nocera DG. *Inorg. Chem.* 2003; **42**: 8270-8277.

46. Chang CJ, Loh ZH, Shi C, Anson FC and Nocera DG. *J. Am. Chem. Soc.* 2004; **126**: 10013-10020.

47. Wasser IM, Martens CF, Verani CN, Rentschler E, Huang HW, Moenne-Loccoz P, Zakharov LN, Rheingold AL and Karlin KD. *Inorg. Chem.* 2004; **43**: 651-662.

48. Martens CF, Murthy NN, Obias HV and Karlin KD. *Chem. Commun.* 1996: 629-630.

49. Ju TD, Woods AS, Cotter RJ, Moënne-Loccoz P and Karlin KD. *Inorg. Chim. Acta* 2000; **297**: 362-372.

50. Wysłouch A, Latos-Grażyński L, Grzeszczuk M, Drabent K and Bartczak T. *J. Chem. Soc., Chem. Commun.* 1988: 1377-1378.

51. Bartczak TJ, Latos-Grażyński L and WysŁouch A. *Inorg. Chim. Acta* 1990; **171**: 205-212.

52. Chishiro T, Shimazaki Y, Tani F and Naruta Y. *Chem. Commun. (Camb)* 2005: 1079-1081.

53. Hematian S, Siegler MA and Karlin KD. *J. Biol. Inorg. Chem.* 2014; **19**: 515-528.

54. Nanthakumar A, Fox S, Murthy NN, Karlin KD, Ravi N, Huynh BH, Orosz RD, Day EP, Hagen KS and Blackburn NJ. *J. Am. Chem. Soc.* 1993; **115**: 8513-8514.

55. Hematian S, Kenkel I, Shubina TE, Durr M, Liu JJ, Siegler MA, Ivanovic-Burmazovic I and Karlin KD. *J. Am. Chem. Soc.* 2015; **137**: 6602-6615.

56. Kim E, Helton ME, Wasser IM, Karlin KD, Lu S, Huang H-w, Moënne-Loccoz P, Incarvito CD, Rheingold AL, Honecker M, Kaderli S and Zuberbühler AD. *Proc. Nat. Acad. Sci.* 2003; **100**: 3623.

57. Halime Z, Kieber-Emmons MT, Qayyum MF, Mondal B, Gandhi T, Puiu SC, Chufán EE, Sarjeant AAN, Hodgson KO, Hedman B, Solomon EI and Karlin KD. *Inorg. Chem.* 2010; **49**: 3629-3645.

58. Ju TD, Ghiladi RA, Lee D-H, van Strijdonck GPF, Woods AS, Cotter RJ, Young VG and Karlin KD. *Inorg. Chem.* 1999; **38**: 2244-2245.

59. Lee SC and Holm RH. *J. Am. Chem. Soc.* 1993; **115**: 11789-11798.

60. Scott MJ, Zhang HH, Lee SC, Hedman B, Hodgson KO and Holm RH. *J. Am. Chem. Soc.* 1995; **117**: 568-569.

61. Oyaizu K, Haryono A, Nishimura Y, Yamamoto K and Tsuchida E. *Bull. Chem. Soc. Jpn.* 1999; **72**: 1781-1784.

62. Liston DJ, Kennedy BJ, Murray KS and West BO. *Inorg. Chem.* 1985; **24**: 1561-1567.

63. Chufán EE, Verani CN, Puiu SC, Rentschler E, Schatzschneider U, Incarvito C, Rheingold AL and Karlin KD. *Inorg. Chem.* 2007; **46**: 3017-3026.

64. Wang Y, Ang PL, Wong C-Y and Yip JHK. *Chem. Eur. J.* 2018; **24**: 18623-18628.

65. Litvinov AL, Konarev DV, Kovalevsky AY, Lapshin AN, Yudanova EI, Drichko NV, Coppens P and Lyubovskaya RN. *Eur. J. Inorg. Chem.* 2003: 3914-3917.

66. Konarev DV, Khasanov SS and Lyubovskaya RN. *J. Porphyr. Phthalocyanines* 2010; **14**: 293-297.

67. Lee HM, Olmstead MM, Gross GG and Balch AL. *Cryst. Growth Des.* 2003; **3**: 691-697.

68. Fleischer EB, Palmer JM, Srivastava TS and Chatterjee A. *J. Am. Chem. Soc.* 1971; **93**: 3162-3167.

69. Kadish KM, Larson G, Lexa D and Momenteau M. *J. Am. Chem. Soc.* 1975; **97**: 282-288.

70. Forshey PA and Kuwana T. *Inorg. Chem.* 1981; **20**: 693-700.

71. Rodgers KR, Reed RA, Su YO and Spiro TG. *Inorg. Chem.* 1992; **31**: 2688-2700.

72. Rywkin S, Hosten CM, Lombardi JR and Birke RL. *Langmuir* 2002; **18**: 5869-5880.

73. Bizzarri AR and Cannistraro S. In *Surface-Enhanced Raman Scattering: Physics and Applications*, Kneipp K, Moskovits M, Kneipp H. (Eds.) Springer Berlin Heidelberg: Berlin, Heidelberg, 2006; pp 279-296.

74. Phillippi MA and Goff HM. *J. Am. Chem. Soc.* 1979; **101**: 7641-7643.

75. Chang D, Cocolios P, Wu YT and Kadish KM. *Inorg. Chem.* 1984; **23**: 1629-1633.

76. Gans P, Buisson G, Duee E, Marchon JC, Erler BS, Scholz WF and Reed CA. *J. Am. Chem. Soc.* 1986; **108**: 1223-1234.

77. Collman JP, Wagenknecht PS and Hutchison JE. *Angew. Chem. Int. Ed. Engl.* 1994; **33**: 1537-1554.

78. Rosenthal J and Nocera DG. In *Prog. Inorg. Chem.*, Karlin KD. (Ed.), 2007; pp 483-544.

79. Sorokin AB. *Bioinorg. React. Mech.* 2012; **8**: 59-84.

80. Guchhait T, Sasmal S, Khan FST and Rath SP. *Coord. Chem. Rev.* 2017; **337**: 112-144.

81. Khan FS, Guchhait T, Sasmal S and Rath SP. *Dalton Trans.* 2017; **46**: 1012-1037.

82. Sorokin AB. *Coord. Chem. Rev.* 2019; **389**: 141-160.

83. Pistorio BJ, Chang CJ and Nocera DG. *J. Am. Chem. Soc.* 2002; **124**: 7884-7885.

84. Rosenthal J, Pistorio BJ, Chng LL and Nocera DG. *J. Org. Chem* 2005; **70**: 1885-1888.

85. Ghosh SK, Patra R and Rath SP. *Inorg Chem* 2010; **49**: 3449-3460.

86. Steiner T. *Angew. Chem. Int. Ed.* 2002; **41**: 48-76.

87. Wollmann RG and Hendrickson DN. *Inorg. Chem.* 1978; **17**: 926-930.

88. Ivashin NV, Shulga AM, Terekhov SN and Dzilinski K. *Spectrochim. Acta A: Mol. Biomol. Spectrosc.* 1996; **52**: 1603-1614.

89. Richman RM and Peterson MW. *J. Am. Chem. Soc.* 1982; **104**: 5795-5796.

90. Peterson MW and Richman RM. *Inorg. Chem.* 1985; **24**: 722-725.

91. Brémard C, Kowalewski P, Merlin JC and Moreau S. *Journal of Raman Spectroscopy* 1992; **23**: 325-333.

92. Chin D-H, La Mar GN and Balch AL. *J. Am. Chem. Soc.* 1980; **102**: 5945-5947.

93. Peterson MW, Rivers DS and Richman RM. *J. Am. Chem. Soc.* 1985; **107**: 2907-2915.

94. Bergamini P, Sostero S, Traverso O, Deplano P and Wilson LJ. *J. Chem. Soc., Dalton Trans.* 1986: 2311-2314.

95. Guest CR, Straub KD, Hutchinson JA and Rentzepis PM. *J. Am. Chem. Soc.* 1988; **110**: 5276-5280.

96. Shantha PK and Verma AL. *Inorg. Chem.* 1996; **35**: 2723-2725.

97. Rosenthal J, Luckett TD, Hodgkiss JM and Nocera DG. *J. Am. Chem. Soc.* 2006; **128**: 6546-6547.

98. Guo C-C. *Acta Chim. Sin.* 1994; **52**: 367-371.

99. Guo C-C. *Journal of Catalysis* 1998; **178**: 182-187.

100. Guo C-C, Liu X-Q, Li Z-P and Guo D-C. *Appl. Catal. A: General* 2002; **230**: 53-60.

101. Guo C-C, Peng Q, Liu Q and Jiang G. *J. Mol. Catal. A: Chem.* 2003; **192**: 295-302.

102. Hu H-Y, Jiang Q, Liu Q, Song J-X, Lin W-Y and Guo C-C. *J. Porphy. Phthalocyanines* 2006; **10**: 948-952.

103. Tabor E, Połtowicz J, Pamin K, Basąg S and Kubiak W. *Polyhedron* 2016; **119**: 342-349.

104. Luo W, Liu D, Sun J, Deng W, Sheng W, Liu Q and Guo C-C. *Chin. J. Chem. Eng.* 2014; **22**: 509-515.

105. Luo W, Sun J, Ye J, Deng W, Liu Q and Guo C-C. *J. Ind. Eng. Chem.* 2014; **20**: 3061-3067.

106. Cordes C, Morganti M, Klawitter I, Schremmer C, Dechert S and Meyer F. *Angew. Chem. Intl. Ed.* 2019; **58**: 10855-10858.

107. Gallagher KJ, Espinal-Viguri M, Mahon MF and Webster RL. *Adv. Synth. Catal.* 2016; **358**: 2460-2468.

108. Settin MF and Fanning JC. *Inorg. Chem.* 1988; **27**: 1431-1435.

109. Ellison MK, Schulz CE and Scheidt WR. *Inorg. Chem.* 1999; **38**: 100-108.

110. Xu N, Campbell ALO, Powell DR, Khandogin J and Richter-Addo GB. *J. Am. Chem. Soc.* 2009; **131**: 2460-2461.

111. Williams LJ, Dowgiallo A-M and Knappenberger KL. *Phys. Chem. Chem. Phys.* 2013; **15**: 11840-11845.

112. Abdullin D, Fleck N, Klein C, Brehm P, Spicher S, Lützen A, Grimme S and Schiemann O. *Chem. Eur. J.* 2019; **25**: 2586-2596.

113. Takeuchi M, Imada T and Shinkai S. *J. Am. Chem. Soc.* 1996; **118**: 10658-10659.

114. Takeuchi M, Imada T and Shinkai S. *Bull. Chem. Soc. Jpn.* 1998; **71**: 1117-1123.

115. Gao D, Li J-Z, Yu R-Q and Zheng G-D. *Anal. Chem.* 1994; **66**: 2245-2249.

116. Schappacher M and Deffieux A. *J. Am. Chem. Soc.* 2011; **133**: 1630-1633.

117. Schappacher M and Deffieux A. *Macromolecules* 2011; **44**: 4503-4510.

118. Schappacher M, Deffieux A and Le Meins J-F. *Polym. Chem*. 2013; **4**: 458-461.

119. Tian X, Lin C, Zhong Z, Li X, Xu X, Liu J, Kang L, Chai G and Yao J. *Cryst.Growth Des.* 2019; **19**: 3279-3287.

120. Wang DH, Pan JN, Li HH, Liu JJ, Wang YB, Kang LT and Yao JN. *Journal of Materials Chemistry A* 2016; **4**: 290-296.

121. Smalley JW, Birss AJ, Szmigielski B and Potempa J. *Microbiology* 2006; **152**: 1839-1845.

122. Smalley JW, Birss AJ, Szmigielski B and Potempa J. *Arch Biochem Biophys* 2007; **465**: 44-49.

123. Gorka AP, de Dios A and Roepe PD. *J. Med. Chem.* 2013; **56**: 5231-5246.

124. Leed A, DuBay K, Ursos LMB, Sears D, de Dios AC and Roepe PD. *Biochemistry* 2002; **41**: 10245-10255.

125. de Dios AC, Casabianca LB, Kosar A and Roepe PD. *Inorg. Chem.* 2004; **43**: 8078-8084.

126. Kuter D, Benjamin SJ and Egan TJ. *J Inorg Biochem* 2014; **133**: 40-49.

127. Hino T, Matsumoto Y, Nagano S, Sugimoto H, Fukumori Y, Murata T, Iwata S and Shiro Y. *Science* 2010; **330**: 1666.

128. Wasser IM, de Vries S, Moënne-Loccoz P, Schröder I and Karlin KD. *Chem. Rev.* 2002; **102**: 1201-1234.

129. Girsch P and de Vries S. *Biochim. Biophys. Acta* 1997; **1318**: 202-216.

130. Moënne-Loccoz P and de Vries S. *J. Am. Chem. Soc.* 1998; **120**: 5147-5152.

131. Moënne-Loccoz P, Richter O-MH, Huang H-w, Wasser IM, Ghiladi RA, Karlin KD and de Vries S. *J. Am. Chem. Soc.* 2000; **122**: 9344-9345.

132. Wei N, Lee D-H, Murthy NN, Tyeklar Z, Karlin KD, Kaderli S, Jung B and Zuberbuehler AD. *Inorg. Chem.* 1994; **33**: 4625-4626.

133. Wasser IM, Fry HC, Hoertz PG, Meyer GJ and Karlin KD. *Inorg. Chem.* 2004; **43**: 8272-8281.

134. Mihara N, Yamada Y, Takaya H, Kitagawa Y, Aoyama S, Igawa K, Tomooka K and Tanaka K. *Chem. Eur. J.* 2017; **23**: 7508-7514.

135. Ghiladi RA, Hatwell KR, Karlin KD, Huang H-w, Moënne-Loccoz P, Krebs C, Huynh BH, Marzilli LA, Cotter RJ, Kaderli S and Zuberbühler AD. *J. Am. Chem. Soc.* 2001; **123**: 6183-6184.

136. Kim E, Chufán EE, Kamaraj K and Karlin KD. *Chem. Rev.* 2004; **104**: 1077-1134.

137. Hematian S, Garcia-Bosch I and Karlin KD. *Acc. Chem. Res.* 2015; **48**: 2462-2474.

138. Nanthakumar A, Nasir MS, Karlin KD, Ravi N and Huynh Boi H. *J. Am. Chem. Soc.* 1992; **114**: 6564-6566.

139. Fox S, Nanthakumar A, Wikström M, Karlin KD and Blackburn NJ. *J. Am. Chem. Soc.* 1996; **118**: 24-34.

140. Nanthakumar A, Fox S, Murthy NN and Karlin KD. *J. Am. Chem. Soc.* 1997; **119**: 3898-3906.

141. Kramarz KWN, Jack R. In *Prog. Inorg. Chem.*, Vol. 42, Karlin KD. (Ed.) John Wiley & Sons, Inc., 1994; pp 1-65.

142. Kopf M-A, Neuhold Y-M, Zuberbuhler AD and Karlin KD. *Inorg. Chem.* 1999; **38**: 3093-3102.

143. Obias HV, van Strijdonck GPF, Lee D-H, Ralle M, Blackburn NJ and Karlin KD. *J. Am. Chem. Soc.* 1998; **120**: 9696-9697.

144. Maia LB and Moura JJG. *Chem. Rev.* 2014; **114**: 5273-5357.

145. Castello PR, David PS, McClure T, Crook Z and Poyton RO. *Cell Metabolism* 2006; **3**: 277-287.

146. Hematian S, Siegler MA and Karlin KD. *J. Am. Chem. Soc.* 2012; **134**: 18912-18915.

147. Hamer M, Tomba JP and Rezzano IN. *Sens. Actuators, B* 2014; **193**: 121-127.

148. Tshepelevitsh S, Kütt A, Lõkov M, Kaljurand I, Saame J, Heering A, Plieger PG, Vianello R and Leito I. *Eur. J. Org. Chem.* 2019; **2019**: 6735-6748.

149. Baldwin MJ, Gelasco A and Pecoraro VL. *Photosyn. Res.* 1993; **38**: 303-308.

150. Hall HK. *J. Am. Chem. Soc.* 1957; **79**: 5441-5444.

151. Coetzee JF and Padmanabhan GR. *J. Am. Chem. Soc.* 1965; **87**: 5005-5010.

152. Izutsu K. *Acid-base dissociation constants in dipolar aprotic solvents*; Blackwell Scientific Publications: Oxford; Boston, 1990

153. Kaljurand I, Kütt A, Sooväli L, Rodima T, Mäemets V, Leito I and Koppel IA. *J. Org. Chem.* 2005; **70**: 1019-1028.

154. Garrido G, Koort E, Ràfols C, Bosch E, Rodima T, Leito I and Rosés M. *J. Org. Chem.* 2006; **71**: 9062-9067.

155. Jutzi P, Müller C, Stammler A and Stammler H-G. *Organometallics* 2000; **19**: 1442-1444.

156. McNamara R, Wu CH, Chirlian LE and Opella SJ. *J. Am. Chem. Soc.* 1995; **117**: 7805-7811.

157. Consonni R, Santomo L, Tenni R, Longhi R and Zetta L. *FEBS Letters* 1998; **436**: 243-246.

158. Gassman PG and Heckert DC. *J. Org. Chem.* 1965; **30**: 2859-2861.

159. Anteunis MJO, Borremans FAM, Gelan J, Marchand AP and Allen RW. *J. Am. Chem. Soc.* 1978; **100**: 4050-4055.

160. Boese R, Bläser D, Y. Antipin M, Boese R, Y. Antipin M, Chaplinski V and de Meijere A. *Chem. Commun.* 1998: 781-782.

161. Meetsma A. *(CSD Private Communication, #667666)* 2005.

162. Schwenger A, Frey W and Richert C. *Angew. Chem. Intl. Ed.* 2016; **55**: 13706-13709.

163. Schmidtmann M and Wilson CC. *CrystEngComm* 2008; **10**: 177-183.

164. Jiang X, O'Brien ZJ, Yang S, Lai LH, Buenaflor J, Tan C, Khan S, Houk KN and Garcia-Garibay MA. *J. Am. Chem. Soc.* 2016; **138**: 4650-4656.

165. Oswald IDH, Motherwell S and Parsons S. *Acta Crystallogr. B* 2005; **61**: 46-57.

166. Klien H, Wilhelm S and Edwin W. *Acta Crystallogr. E* 2015; **71**: 1439-1443.

167. Van Gelder BF and Beinert H. *Biochim. Biophys. Acta* 1969; **189**: 1-24.

168. Rivetti C, Mozzarelli A, Rossi GL, Henry ER and Eaton WA. *Biochemistry* 1993; **32**: 2888-2906.

169. Andersson R, Safari C, Dods R, Nango E, Tanaka R, Yamashita A, Nakane T, Tono K, Joti Y, Båth P, Dunevall E, Bosman R, Nureki O, Iwata S, Neutze R and Brändén G. *Sci. Rep.* 2017; **7**: 4518.

170. Han Du W-G, McRee D, Götz AW and Noodleman L. *Inorg. Chem.* 2020; **59**: 8906-8915.